Design and system identification for a plasma transferred arc additive manufacturing technology

by

Jose Guadalupe Mercado Rojas

A thesis submitted in partial fulfillment of the requirements for the degree of

Doctor of Philosophy

Department of Mechanical Engineering
University of Alberta

Abstract

The increase in the pace of development of additive manufacturing technology opens new markets and expands the scope of research and knowledge. Additive manufacturing, previously known as rapid prototyping, can employ advanced state-of-the-art materials, such as metal composites, in metal 3D printing, which brings about new concerns and challenges addressable through the scientific method. Recent additive manufacturing research focuses on the benefits of these materials, including printing components with enhanced mechanical properties. For example, the application of nickel alloys with tungsten carbide particles to print units for the oil and gas industry improves wear resistance and reduces corrosion in harsh environments. Better components lead to reduced failures and fewer unexpected shutdown costs. In this context, this research proposes a research methodology to extend the capabilities for a plasma transferred arc welding system to function as additive manufacturing equipment and improve the 3D printing quality to fulfill the requirements of heavy-duty industries. The following three objectives guide the activities of this research: 1) Develop a systematic design methodology for additive manufacturing systems, with the intent to produce different design layers for the mechanical, the electronic, and the software design to achieve a functional metal additive manufacturing system for metal matrix composites with particular mechanical properties. The framework is applied in the case study of a plasma transferred arc welding system. 2) Validate and characterize the system for metal 3D printing of nickel-metal matrix composites to demonstrate that the printed parts have geometric stability and microstructure characteristics similar to those presented in the overlay industry. The objective also

understands the contribution of process parameters to the improvement of geometrical outcomes. 3) Research and develop in-situ measuring strategies to quantitatively understand the physics of the plasma transferred arc additive manufacturing process by examining the time, spatial, electrical, thermal, and geometrical domains for the deposition performance, and by establishing geometric benchmark test artifacts to assess the performance and limitations of the sensing mechanisms. The assessment indicates how the voltage sensor is employed to predict bead height and deviations perpendicular to deposition in multilayer components. The outcome of this research is expected to make significant contributions to the domain of additive manufacturing research by proposing an integrated function modelling-based design methodology that serves as a framework for the development, characterization, validation, and testing of metal additive manufacturing systems for metal matrix composites with particular mechanical properties.

Preface

Some of the research conducted for this thesis forms part of an international research collaboration at Tec de Monterrey Campus Guadalajara, with professors Ahmed Qureshi, Brian Fleck, and Tonya Wolfe being the lead collaborators at the University of Alberta.

Chapters 1, 2, and 5 of this thesis are the original work of J.G. Mercado Rojas.

Chapter 3 of this thesis has been published as J.G. Mercado Rojas, E. Tamayo, T. Wolfe, B. Fleck, and A. J. Qureshi, "Design modeling for additive manufacturing in the case study of a systematic methodology applied to plasma transferred arc additive manufacturing," *Procedia CIRP*, vol. 84, issue 2019, 283-289. I was responsible for the data collection and analysis, as well as the manuscript composition. E. Tamayo assisted with the identification and application of the integrated function modelling. T. Wolfe, B. Fleck, and A. J. Qureshi were the supervisory authors and were involved with concept formation and manuscript composition.

The first part of Chapter 4 of this thesis has been published as J.G. Mercado Rojas, T. Wolfe, B.A. Fleck, and A. J. Qureshi, "Plasma transferred arc additive manufacturing of Nickel metal matrix composites," *Manufacturing Letters*, vol. 18, issue 2018, 31-34. I was responsible for the data collection and analysis, as well as the manuscript composition. T. Wolfe, B.A. Fleck, and A. J. Qureshi were the supervisory authors and were involved with concept formation and manuscript composition.

The second part of Chapter 4 has been accepted to be published as J. G. Mercado Rojas, M. Ghasri-Khouzani, T. Wolfe, B. Fleck, H. Henein, and A. J. Qureshi, "Preliminary geometrical and microstructural characterization of WC-reinforced NiCrBSi matrix composites fabricated by plasma transferred arc additive manufacturing through Taguchi-based experimentation," *The International Journal of Advanced Manufacturing Technology.* I was responsible for the conceptualization, formal analysis, investigation, methodology, validation, and writing original draft. M. Ghasri-Khouzani provided guidance in the formal analysis. T. Wolfe, B. Fleck, H. Henein, and A. J. Qureshi were the supervisory authors and were involved with concept formation, resources, supervision, and manuscript composition.

In Chapter 5, the technical apparatus referred to as "Thermocouple array" and data analysis were designed by myself, with the assistance of A. J. Qureshi. The printed components shown as single-track multiple-layer cuboid shapes presented in the validation section were printed by S. N. El Moghazi and analyzed by myself.

"The highest activity a human being can attain is learning for understanding, because to understand is to be free."

-Baruch Spinoza

Acknowledgements

I dedicate this thesis to my family. To my wife, Jessica, who committed her time and effort, and for this I appreciate you infinitely. Without her support and patience, I could have not reached this point in my life. To my beloved children, Diego and Leonor, I hope to be an example of motivation for them to achieve their goals just as my parents are to me.

To my parents, Gerardo and Maria de Jesus, to my siblings, Rocio, Eliza, and Gerardo, thank you for cheering me on from 3,700 kilometres away. To my grandparent, Guadalupe Mercado, thank you for showing me to care about those small details in life. To my parents-in-law, Roberto and Gloria, and my siblings-in-law, Roberto, Gabriela, and David, thank you for all your support.

I would like to express my gratitude to Tec de Monterrey and CONACYT for their financial support, and to Joaquin Campos, Adriana Encinas, Antonio Renteria, and Ricardo Swain in particular for their words, suggestions, and help in this endeavour.

To Stefano Chiovelli from Syncrude for sponsoring the research in collaboration with NSERC and to Innotech Alberta - Garry Fisher, Ron Rau, Tegbir Singh, Johanna Meier, Brenda Hall, thank you for sharing your expertise and life stories. A sincere thanks to Mike Danysh and Riya Patel for their support and training in the different instruments and equipment.

Thank you to the University of Alberta, to my professors, Peter Schiavone, Morris Flynn, Kajsa Duke, Martin Barczyk, and John Doucette, to the people in the shop, Roger, Daniel, Andrew, Rick, and Marc, to the administrative personnel, Gail, Richard, Isabelle, and Serena, to my co-op students, Lucas Dos Santos Luchiari, Cole Milburn, Theze Pascal, and Andrew Dalziel, to my editor, Kristin Berg, and to my friends, Hani, Prashant, Thomas, Morteza, Aziz, Jonas, Edgar, Balak, Dylan, Khaled, Baltej, Pablo, Elisa, Sandy, and Nancy. Each one of you contributed to my journey on this path. I am glad to have shared moments and experiences with you.

To my friends in Canada, Tetsu, Roberto, Eufracio, Abril, and Natalia, thank you for the support during my stay. To my friends Joaquin, Esau, David, Hugo, Barocio, Enrique, and Espadas, for the virtual meetings and all the recommendations, thank you.

Finally, a heartfelt thank you to the backbones of this work, Ahmed Qureshi, Brian Fleck, and Tonya Wolfe. We shared a bunch of moments, and I enjoyed all and each one of them. I learned a lot about both academia and life. Thank you for all your mentorship and your friendship. You are a gift to those around you. You are awesome!

Table of Contents

List of Tables

List of Figures

xviii

Chapter 1

Introduction

The process of converting raw material into a finished good is called manufacturing [1]. Manufacturing technology involves sizing, shaping and disclosing the desired combination of properties to perform the intended function of the component [2]. Three pillars support manufacturing: additive manufacturing (AM), subtractive manufacturing, and formative manufacturing. AM, also known as three-dimensional (3D) printing, is a fabrication process based on layer deposition for making three-dimensional physical objects directly from a computer-assisted design (CAD) model [3].

The global AM market is forecast to grow by a compound annual growth rate (CAGR) of 15%, passing from $5.31 billion revenue generation in 2015 to $21.5 billion in 2025 [Fig. 1.1]. The prediction is that aerospace, automotive, and medical industries will account for 51% of the market. The adoption of AM technology will reduce logistics costs, decrease inventory, tooling, and maintenance machine operations, and reduce lead and cycle times [4].

Locally, AM adoption in the Canadian industry is currently very low. Although manufacturing is the second largest industry in Canada [6], only 1.6% of all enterprises have used AM for plastic, 0.8% have used AM for metals, and 0.6% have used AM for other applications according to a 2014 Survey of Advanced Technology con-
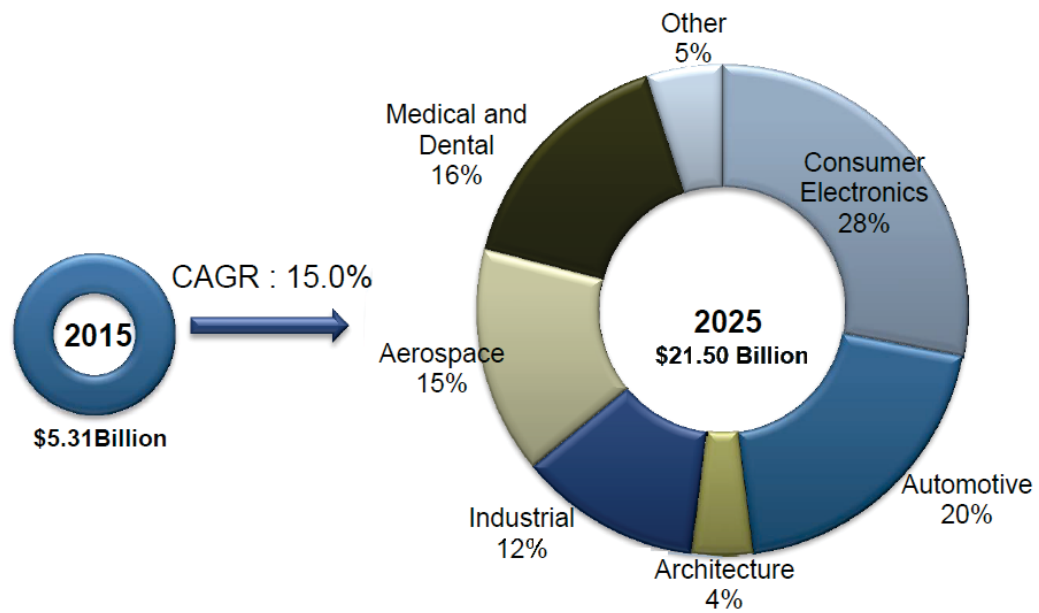
Figure 1.1: Compound annual growth rate in AM from 2015 to 2025 [4].
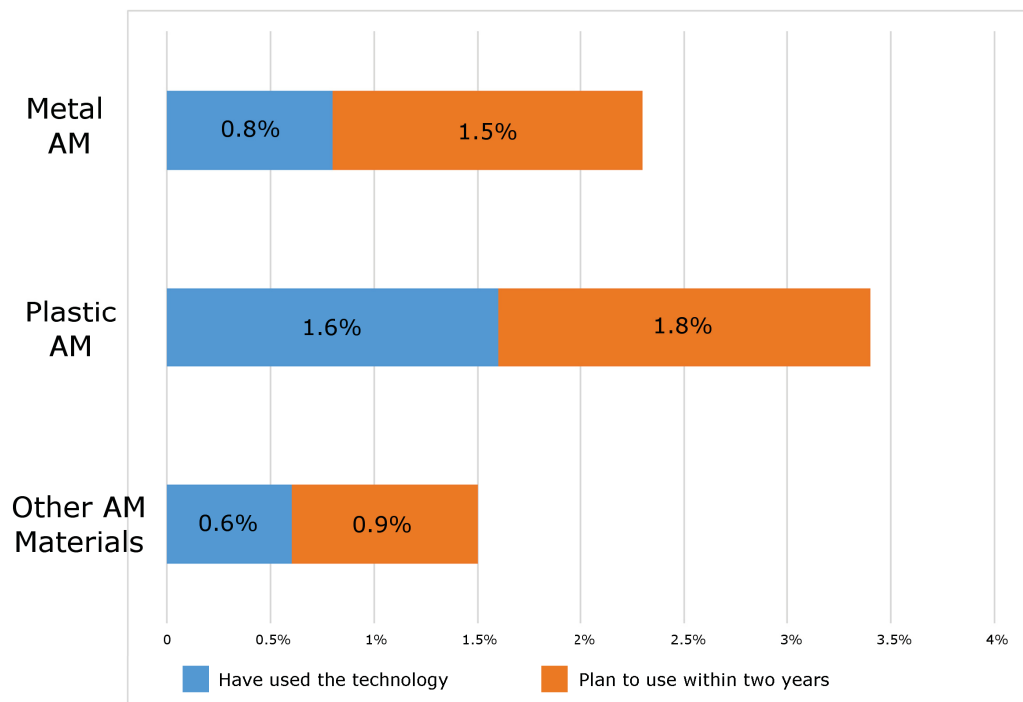
Figure 1.2: Adoption level of AM by Canadian Companies, 2014 [5].

ducted by Statistics Canada [7]. The adoption level of AM in Canada is expected to increase by 3.4% for plastic AM and 2.3% for metal AM [5] [Fig. 1.2].

1.1 Project rationale

Throughout history, manufacturing processes have been in a state of constant evolution. The development of new technology is allowing manufacturing to overcome challenges with improved and customized results. Traditionally, subtractive manufacturing has dominated the industry due to its process stability, automation, productivity, and quality assurance [8]. However, new materials have allowed components to improve in terms of functionality due to advancements in certain mechanical properties. The downside of using advanced materials is the complexity involved in their integration into a streamlined manufacturing process. One possible solution to increase the level of adoption of advanced materials is their integration through AM.

According to Frazier [9], specific technical challenges in metal additive manufacturing include (i) innovative structural design, (ii) qualification and certification, (iii) maintenance and repair, and (iv) direct digital manufacturing science and technology. The top level most significant technical challenges include the following:

- Development of integrated in-process, sensing, monitoring, and controls to understand and control variability.

- Alternatives to conventional qualification methods to validate models, probabilistic methods, and part similarities.

- Development of integrated structural and materials design tools to accelerate AM adoption.

- Underline science of Metal AM to meet the needs in the development of physics-based models relating microstructure, mechanical properties, and performance.

There are numerous companies in the AM market that are using equipment that meets present-day needs for AM. However, it is anticipated there will be an increase in the pace of development of new AM technologies in the following decades, and new applications are already emerging, particularly in the field of highly specialized equipment. The mining and oil & gas industries, in particular, are environments in which spare parts for heavy-duty equipment are often not available in a timely, cost-effective manner when they are needed. A metal AM technology is needed that can create spare parts for the industry in a brief time where tooling costs for casting or injection moulding would be too high or unfeasible to achieve. Moreover, by reducing the lead time, this AM technology promotes the generation of customizable components made of advanced materials to minimize unexpected downtime costs, which can reach \$115M/day [10]. Therefore, the purpose of this work is to present the design, development, and characterization of a novel metal AM system integrating a conventional plasma transferred arc (PTA) system as an energy source. The plasma transferred arc additive manufacturing (PTA-AM) system aims to provide solutions to current challenges in the printing of metal components using advanced materials. This work focuses on the 3D printing of parts made out of a metal matrix composite (MMC) to boost the production of elements with wear-resistant properties and suitable for heavy-duty environments such as the ones in the mining, and oil & gas industries. Direct energy deposition (DED) technology based on PTA-AM provides enough heat input to melt a wide variety of metals in the form of powder feedstock. The energy source and a stream of raw material intersect at a focal point giving rise to melt pool formation [11].

1.2 Research Objectives

The main goal of this research is to design, apply, and validate design methodology, and to measure and test the implementation of a PTA-AM system. To meet this goal, the following objectives are pursued in this research:

1. Apply a systematic design methodology for AM systems, with the intent to produce different design layers for the mechanical, the electronic, and the software design to achieve functionality and supply an initial framework for the design of new AM technology. The framework is applied in the case study of a PTA welding system.

2. Validate and characterize the system for metal 3D printing of nickel metal matrix composites. The goal is to demonstrate that the printed parts have geometric stability and microstructure characteristics similar to those presented in the overlay industry. Additionally, the objective is to identify significant process parameters and their contribution to the deposition of MMC. The hypothesis is that certain combinations of the process parameters contributes to the improvement of geometrical outcomes.

3. Research and develop in-situ measuring strategies to quantitatively understand the physics of the PTA-AM process. One objective is to determine the time, spatial, electrical, thermal, and geometrical domains for the deposition performance. Another objective is establish geometric benchmark test artifacts to assess the performance and limitations of the sensing mechanisms. The last objective is to improve the voltage sensor to predict bead height and deviations that are located perpendicular to the deposition of multilayer components.

1.3 Thesis Organization

Chapter 2 presents the background and motivation behind metal additive manufacturing. The classification and state-of-the art of metal AM is the foundation of the work in AM systems for heavy-duty industries. Chapter 3 proposes the design methodology for additive manufacturing systems through the various design layers. Chapter 4 presents the initial steps toward printing metal components and the microstructural comparison against overlaying of the same material on components for the oil and gas industry. Additionally, this chapter presents the identification of process parameters and their contribution to the geometrical characteristics of multilayer samples. Chapter 5 presents the development of in-situ monitoring sensors and their capabilities, performance, and limitations, which involves the application of a voltage sensor to predict the bead height on the deposition and the deviations in printed walls. Finally, Chapter 6 presents the conclusions, limitations, and recommendations for future work for PTA-AM technology.

Chapter 2

Background

Additive manufacturing is in a position similar to where the Internet was 25 years ago [12]. Back then, few could have anticipated the impact that the Internet was about to have on humankind. Going back to early 1993, the Internet was both old and young. Although it started in the late 1970s, it was not until 1993 that a watershed moment for the Internet occurred, with the release of the Mosaic web browser. This event allowed users to travel through the world of electronic information using a point-and-click interface [13]. This event was the birth of web surfing and the start of the Internet as an unlimited source of information.

The technology used in AM is old and young as well. Although the first attempts at building 3D objects happened 50 years ago, a new era for AM is emerging from its own watershed moments. For the first time in 2007, the Gartner hype cycle for emerging technologies showed 3D printing as a technology that was triggered for mainstream adoption in five to ten years [14] [Fig. 2.1].
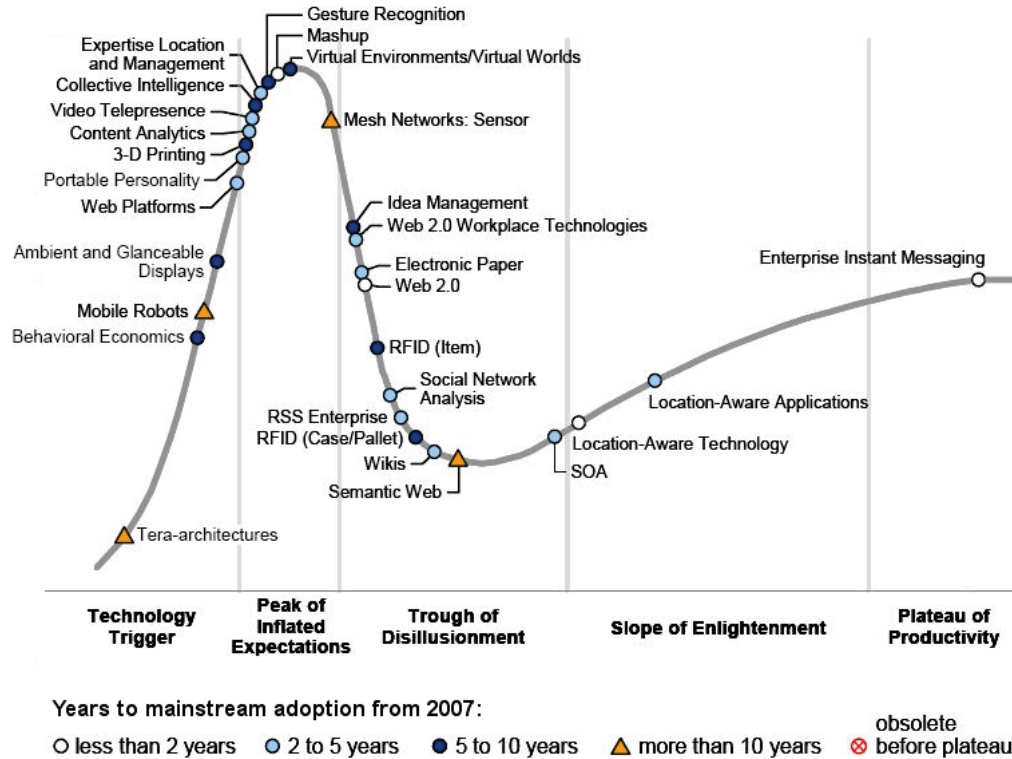
Figure 2.1: Gartner hyper cycle for emerging technologies 2007 [14].

2.1 Watershed moments in AM

The first watershed moment for AM came from Greg Morris and his engineering team [15]. In 2003, GE Aviation engineers were developing an efficient fuel nozzle for a new jet engine. The complexity of the design introduced obstacles in the manufacturing process. The design consisted of 20 different parts welded and brazed together, but every attempt at casting failed. The piece was sent to Morris Technologies, a product development company and contract manufacturer that used AM. All 20 parts were combined into a single unit that weighed 25% less and was more than five times as durable as the original nozzle design [Fig. 2.2]. In a moment, AM eliminated a problem that GE aviation engineers had struggled with for years. This innovation relieved pressure on its financial model by reducing costs by 75% and increasing the product's strength and reliability. Since then, the LEAP jet engine that

has been using this fuel nozzle has carried more than 5 million passengers, with over 14,500 orders valued at $210 Billion. The AM fuel nozzle contributes to a 15% improvement in fuel efficiency.

Figure 2.2: GE Fuel Nozzle for the LEAP jet engine.

The second watershed moment came in 2007. According to Steinar Killi [16], associate professor at the Institute of Design in Oslo, Norway, the expiration of patents, and the maturity of the technology improved the perception of 3D printing among the public and in industry. The ability of AM to function as a product instead of only a mere prototype and the idea that *We are all designers* is supported by the maker culture where anyone with access to a 3D-printer can design and create custom products, which generates endless possibilities to AM users.

AM technology continues to advance ten years after the Gartner hype cycle. According to Frost & Sullivan [4], an increasing trend toward cost-effective manufacturing and rapid production is leading to favourable growth, particularly in the aerospace, automotive, healthcare, and consumer product sectors. This technology is developing an agile manufacturing environment reducing the lead time from conception to production by 70% or more [4].

2.2 Literature review

2.2.1 History of metal 3D printing

The first patent related to metal 3D printing can be traced to 1925, where R. Baker proposed a method to use electric arc welding for making decorative articles using layers [17]. The objective of the invention was to construct walls of receptacles or containers by manipulating a fusible electrode helically to the superposed deposit of metals [Fig. 2.3].
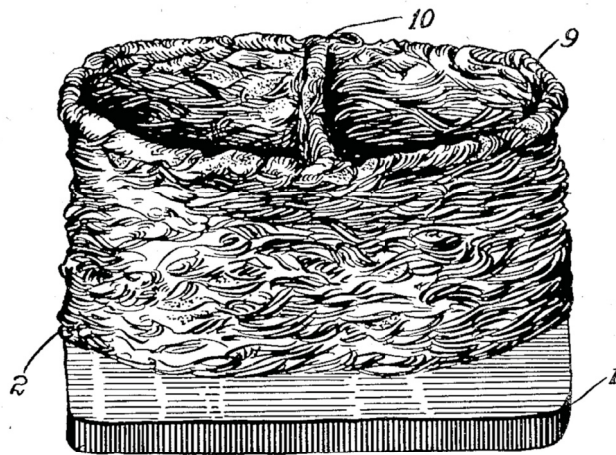
Figure 2.3: Method of making decorative articles patented by R. Baker [17].

The application of a coating from heat-fusible material was patented in 1967 by H. Ingham [18]. Metal or ceramic particles were sprayed against a surface to be coated. This patent is the first to mention that an optical laser could be employed as a heat source for an instantaneous burst of light energy.

In 1971, A. Ujiie patented an apparatus for building circular vessels from welded metal deposition [19, 20]. A thick-walled circular cross-section vessel is fabricated from weld metal. A progressive bead deposition forms a continuous helical strip where the heat of the freshly deposited molten weld is used as heat treatment and then forced to cool abruptly. Afterwards, the part was mechanically trimmed to maintain inner and outer diameters [Fig. 2.4].
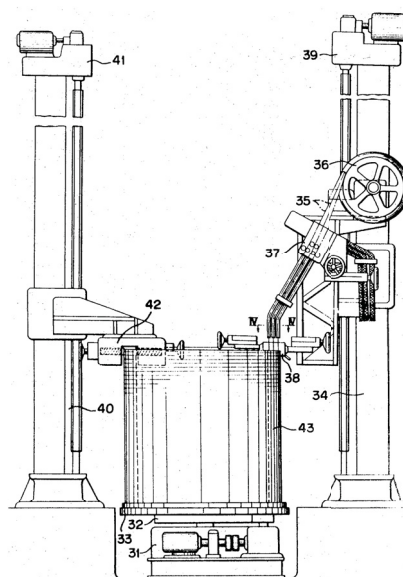
Figure 2.4: Method of and apparatus for constructing substantially circular cross-section vessel by welding patented by A. Ujiie [20].

The first technology using powders was developed by P.A. Ciraud in 1973 [21]. This process features all the modern direct deposition AM techniques. The patent disclosed a manufacturing process of objects from different materials that can be partially melted. Small particles are applied to a matrix, and a laser, electron beam, or

plasma beam heats the particles locally. Figure 2.5 shows how by using these heat inputs coalescence in the particles is achieved to form a continuous layer [22].
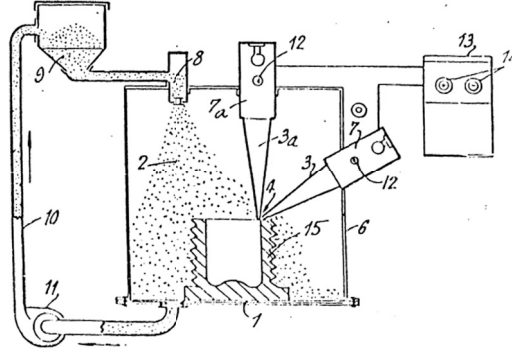
Figure 2.5: A method and apparatus for manufacturing objects made of any arbitrary material meltable patented by P.A. Ciraud [21].

By 1974, the Thyssen company embarked on plans for constructing components made only of weld metal. They were able to build a 72 ton multilayer weldment by a method called shape welding [23, 24]. This method has specific advantages for the manufacturing of thick-walled components of any dimensions with a wide range of high strength, creep- and corrosion-resistant properties. Four tandem welding heads were located above the mandrel with welding speeds of 70 cm/min.

The first use of a plasma jet for a surfacing process for metallic parts was introduced in 1974 by the Institute of technology research for machine building in Romania [Fig. 2.6]. Berinde et al. used granular and powder fillers delivered on open-channel strips to obtain a weld surfacing layer with required geometrical parameters and chemical composition [25].

Skin melting was proposed as a surface treatment for metallic components in 1978. This method involves the fusion of a thin surface layer by a concentrated energy source. Cooling and solidification times were crucial in maximizing the temperature gradients to develop unique microstructures [26].
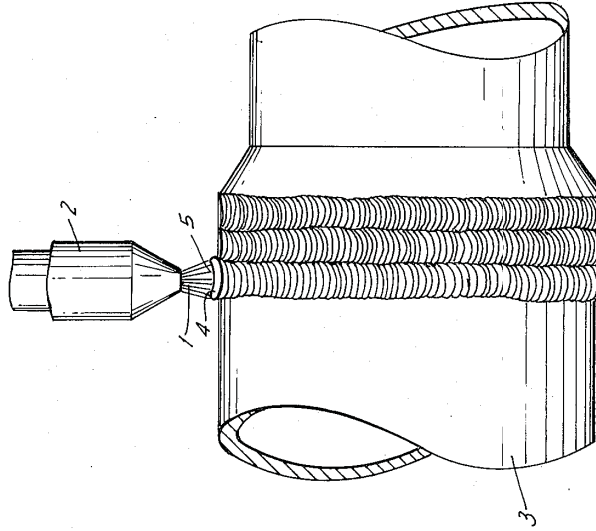
Figure 2.6: Tool joint surfaced with granular tungsten carbide patented by V. Berinde [25].

A sweeping laser beam was proposed by Ditto to deposit material on a valve seat for engine cylinder heads [27]. The purpose was to obtain an alloyed insert with little or no machining. This work was the prelude to the concept Near-Net Shape coined by Brown in 1982 [28], which describes a method for fabricating articles by sequential layer deposition to produce bulky rapidly solidified metallic parts by depositing multiple thin layers of feedstock using an energy beam to fuse the material.

The earliest powder selective laser sintering patent was secured in 1981 by R.F. Housholder, which proposes a moulding process for forming a three-dimensional artifact by layers [29]. A cast material and a moulding material are deposited in unsolidified form sequentially in planar layers. An embodiment and fusible particles are employed to form each layer selectively fused by a laser beam using a controlled heat scanning process. After one layer is selectively combined, another layer will be added to the top to repeat the process. After the object has been formed, the unfused particles will be removed by dusting, blowing, or washing the finished part [Fig. 2.7].
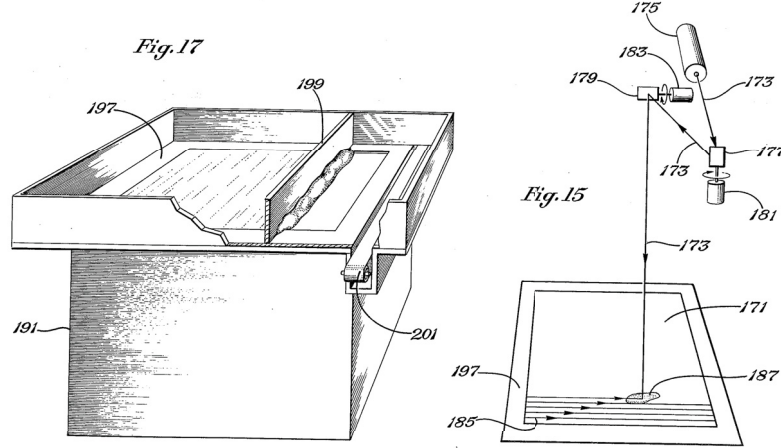
Figure 2.7: Molding process patented by R.F. Housholder [29].

Since 1998, intensive work related to close-loop controllers has been done, particularly in the context of laser cladding. The company DM3D also known as the POM group, has developed several patented grants [30, 31, 32, 33, 34] and applications [35, 36, 37, 38, 39, 40] oriented to real-time strategies. Another system is disclosed for monitoring and controlling the laser cladding process by powder injection that uses automated direct feedback control through optical charge-coupled device (CCD)-based detectors to produce the desired clad quality. This work presented by E. Toyserkany includes patent grants in the US [41] and Canada [42] and applications in the US [43] and worldwide [44].

Further insight into the prehistory of additive manufacturing and the history of stereolithography can be found in Appendices A and B, respectively.

2.2.2 Classification and state-of-the-art of metal AM

Metal AM systems can be classified in terms of the type of process, building volume, or energy source. Table 2.1 lists commercial off-the-shelf AM technology and their manufacturers. The list is divided into three broad categories: powder bed systems, powder feed systems, and wire feed systems [9].

In the literature, research in DED has focused on wire arc additive manufacturing (WAAM). Gas metal arc welding (GMAW) and its particular form of cold metal transfer (CMT) technology has been used to produce thin-walled structures and analyze the thermal history, microstructure, and mechanical properties [45, 46, 47, 48]. Other authors employed micro-lasers, micro-plasma, and thin wires to analyze geometrical properties in thin-walled structures [49, 50]. With respect to PTA-AM, there is no previously published studies. There is one technology which is commercially available for direct metal fabrication. The Materials and Electrochemical Research (MER) Corporation developed a plasma transferred arc-selective free form fabrication (PTA-SFFF) equipment for printing 3D metal parts made of Ti6Al-4V and the refractory alloys Mo-Re and Ta-W [51], but the equipment has not been used for nickel alloys with tungsten carbide particles.

The present research undertakes the development of a PTA-AM system that is suitable for the mining, oil, and gas industries because it is capable of building metal parts made of a nickel alloy with tungsten carbide particles. Chapter 3 presents the design methodology that was followed to build the PTA-AM system. The validation and characterization of AM components are demonstrated in Chapter 4. Chapter 5 presents the development of in-situ measurement strategies implemented in the AM system to provide reliable solutions to current metal printing challenges.

Table 2.1: Representative Metal AM equipment sources and specifications [9].

System	Process	Build volume (mm)	Energy Source
Powder Bed			
ARCAM (A2)	EBM	200 x 200 x 350	7 kW electron beam
EOS (M280)	DMLS	250 x 250 x 325	200-400 W Yb-fiber laser
Concept Laser (M3)	SLM	300 x 350 x 300	200 W fiber laser
Renishaw (AM 250)	SLM	245 x 245 x 360	200 or 400 W laser
Powder Feed			
Optomec (LENS 850-R)	LENS	900 x 1500 x 900	1 or 2 kW IPG fiber laser
POM DMD (66R)	DMD	3,200° x 3,670° x 360°	1-5 kW fiber diode or disk laser
Accufusion laser consolidation	LC	1,000 x 1,000 x 1,000	Nd: YAG laser
Wire feed			
Sciaky (NG1) EBFFF	EBDM	762 x 483 x 508	>40 kW @ 60 kV welder
MER PTA selected FFF	PTAS FFF	610 x 610 x 5182	PTA using two 350A DC power supplies

Further insight regarding AM classification and technology can be found in the Appendix C.

Chapter 3

Design modelling for additive manufacturing systems and the plasma transferred arc case study[1]

This chapter presents, through a systematic implementation of a case study, a design methodology for conceiving and designing additive manufacturing (AM) systems. Integrated function modelling (IFM) is employed to systematically create a metal additive manufacturing system for advanced materials with particular mechanical properties. Based on the design criteria, a use case is developed for a new AM machine. This use case is transformed into a process view, where processes are structured to constraint the scope of the system and its functional specific requirements. IFM is also applied to understand the system from the general to the particular functions as well as to identify the operands and their states. Different design layer implementations of IFM are carried out for mechanical, electronic, and software design, and applied for concept development in the case study. Finally, the actor view is implemented to carry out the high-level system and sub-system decomposition and then is linked to custom fabrication or commercially available off-the-shelf system acquisition for building an experimental setup. These systems are integrated to achieve the functionality as a proof of concept. This chapter demonstrates the application of the methodology through the fabrication of a final working prototype based on an inte-

---

[1]This chapter was published as a journal article in *Procedia CIRP* [52]

grated Kennametal Starweld 400A Plasma Transferred Arc Source and a three-axes motion control system. This chapter also explores the employment of digital mockup and computer-aided design simulation techniques for system design in conjunction with IFM for fabrication. The research objective is to develop a framework for the design modelling of additive manufacturing products that is capable of overcoming the particular challenges in these types of manufacturing processes. A case study for a plasma transferred arc (PTA)-AM system is presented in this chapter in which the IFM approach is applied.

3.1 Structure of the IFM

AM technology is contributing to the development of an agile manufacturing environment with a high impact in the industry by reducing the lead time from conception to production by 70% or more [4]. An increase in AM technology development is forecasted in the following decades. In the system design field, there are different structures, arrangements, and applications for design modelling. Asadollahi-Yazdi et al. [53] proposed an extended version of the design for manufacturing (DFM) in which a skin-skeleton approach is considered to integrate attributes in the product model with particular features in the AM process. Although the case study is applied to an AM part in fused deposition modelling, the model accounts for manufacturing constraints and integration of functional properties for AM components. Another part-driven methodology is proposed by Zaman et al. [54] in which a concurrent process called integrated product process design (IPPD) is developed for allocating the right resources in AM parts. Material, machines, and process selection are the anchor points in the conceptual design decision space, and their methodology is validated by the case study of a crank with defined functional specifications. The authors employed Ashby's material and process indices for a preliminary selection of AM materials, machines and processes. Finally, the authors performed screening and ranking through a

multi-criteria decision making (MCDM) method called the analytical hierarchy process (AHP). The authors then found the resulted combinations are options for the customer to select a technology to print the part.

The design models described on previous paragraph are based on AM parts and their functional features. Concerning multidisciplinary systems, the work presented by Campean and Yildirim [55] is an example of generic function modelling. In their study, a generalized methodology called Enhanced Sequential Diagram (ESD) based on the exchange and flow of functional requirements reasoning is proposed and validated with the case study of an Electric Vehicle Powertrain (EVP). In other work, Eisenbart [56] introduced a modular functional modelling framework across disciplines. Here, a perspective towards integrated systems in the field of mechanical engineering design, electrical engineering design, software development, mechatronic system development, service development, and product and service system design is depicted. Eisenbart [57] presents a case study of the IFM methodology applied to a coffee vending machine for validation purposes. Further adaptations were proposed by Eisenbart [58] for coupling the model with characteristics-properties modelling (CPM) and property-driven development (PDD) to represent diverse information to multi-technology products and services. This IFM structure has shown effective results in the implementation of control panels proposed by Tamayo et al. [59]. The use of axiomatic design (AD) for defining the design structure matrix (DSM) and its integration to the interaction view offers a framework for complex system design. In general, the structure of the IFM is represented by five views: interaction, actor, process flow, state and use case [Fig. 3.1].
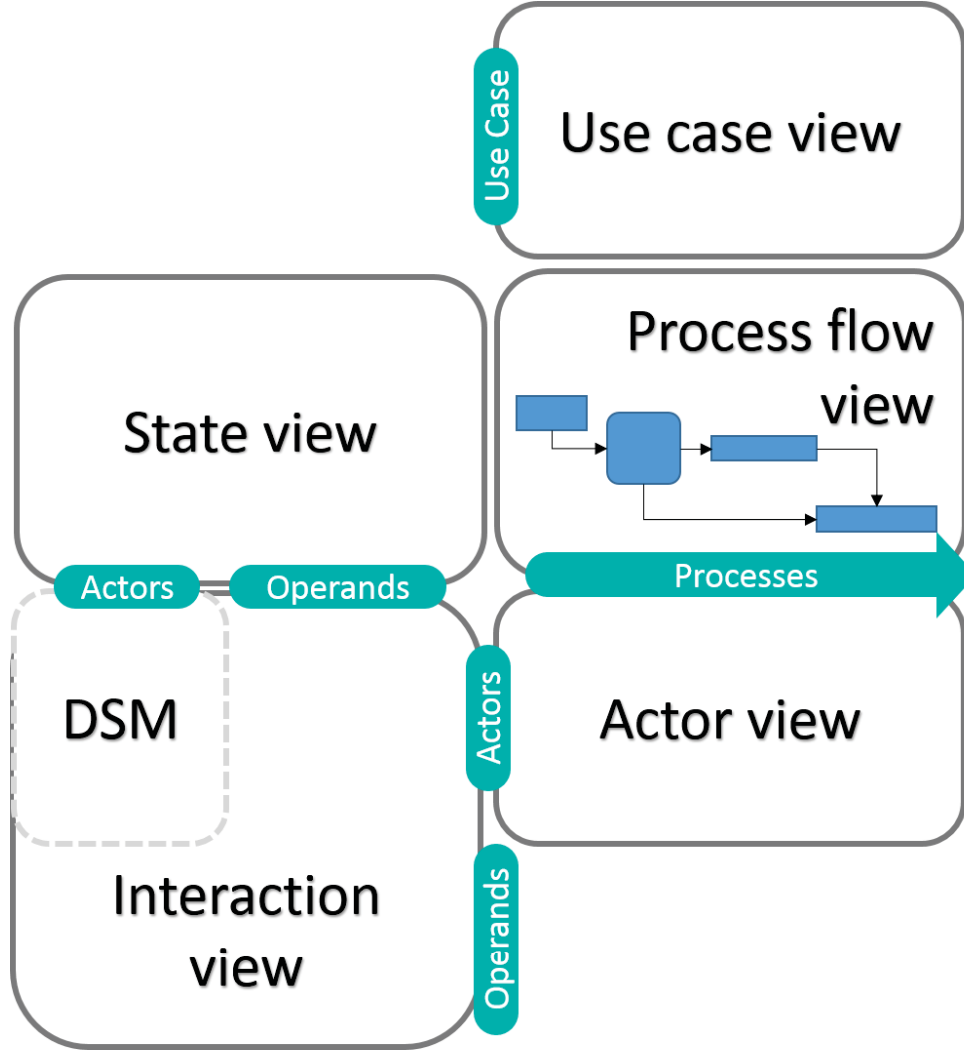
Figure 3.1: IFM adapted from Eisenbart [56] and Tamayo [59].

In the present work, the IFM methodology is applied for AM systems and its integration through design layers. The process begins with the definition of the actors and operands through AD for the interaction view. Then the actor view supports to define the procedures required for the system in the process flow view. The state view allocates the contribution of each actor and operands to the processes. Finally, the use case view represents the functionalities of the system.

3.1.1 Defining actors through Axiomatic Design

The AM design modelling methodology starts with the needs presented by the customer for creating a specialized system. Particular needs can also acquire these specifications according to the industry needs. Both ways are meant only to guarantee attributes that the system must satisfy and belong to the customer domain in the AD [60]. The basis of the customer needs (CNs) domain is given by $\left\{\underline{\mathbf{e_i}}\right\}_{i=1}^{l}$, and its vector can be represented as:

$$\underline{\mathbf{CN}} = CN_i\underline{\mathbf{e_i}} \tag{3.1}$$

Subsequently, functional requirements (FRs) are defined to fulfill the needs and delimit the design. A robust design demands reliable foundations through feasible, valid, unambiguous, verifiable, modifiable, consistent, complete and traceable FRs [61]. The neutrality at this level leads to unbiased proposals and improved creativity. The basis for the FR domain is defined by $\left\{\underline{\mathbf{f_j}}\right\}_{j=1}^{m}$. Equation 3.2 shows the FR vector.

$$\underline{\mathbf{FR}} = FR_j\underline{\mathbf{f_j}} \tag{3.2}$$

A mapping of the domains between CNs and FRs through the CNFR binary tensor $(\overline{\overline{\zeta}})$ is shown by Equation 3.3, where various requirements can be accounted for single needs.

$$\underline{\mathbf{CN}} = \overline{\zeta} * \underline{\mathbf{FR}} = \zeta_{ij}(\underline{\mathbf{e_i}} \otimes \underline{\mathbf{f_j}})FR_j\underline{\mathbf{f_j}}$$

$$= \zeta_{ij}FR_j(\underline{\mathbf{e_i}} \otimes \underline{\mathbf{f_j}})\underline{\mathbf{f_j}}$$

$$= \zeta_{ij}FR_j(\underline{\mathbf{f_j}} \cdot \underline{\mathbf{f_j}})\underline{\mathbf{e_i}}$$

$$= \zeta_{ij}FR_j\delta_{jj}\underline{\mathbf{e_i}} \qquad (3.3)$$

$$= \zeta_{ij}FR_j\underline{\mathbf{e_i}} = CN_i\underline{\mathbf{e_i}}$$

$$\therefore CN_i = \zeta_{ij}FR_j$$

The next domain mapping in the AD is between the functional and physical domains. Design parameters (DPs) are the key variables and actors that characterize the design to support the specified FRs. The DP domain basis is $\left\{\underline{\mathbf{g_k}}\right\}_{k=1}^{n}$ and it can be represented by the vector:

$$\underline{\mathbf{DP}} = DP_k\underline{\mathbf{g_k}} \qquad (3.4)$$

Although labelled as part of the physical domain, some DPs might not be tangible (e.g. DPs in software design). The purpose of the mapping guided by the FRDP tensor $(\overline{\phi})$ is to allocate DPs that can satisfy the FRs typically in a one-to-many process without compromising the independence and information Axioms [62].

$$\underline{\mathbf{FR}} = \overline{\phi} * \underline{\mathbf{DP}} = \phi_{jk}(\underline{\mathbf{f_j}} \otimes \underline{\mathbf{g_k}})DP_k\underline{\mathbf{g_k}}$$

$$= \phi_{jk}DP_k(\underline{\mathbf{f_j}} \otimes \underline{\mathbf{g_k}})\underline{\mathbf{g_k}}$$

$$= \phi_{jk}DP_k(\underline{\mathbf{g_k}} \cdot \underline{\mathbf{g_k}})\underline{\mathbf{f_j}}$$

$$= \phi_{jk}DP_k\delta_{kk}\underline{\mathbf{f_j}}$$ (3.5)

$$= \phi_{jk}DP_k\underline{\mathbf{f_j}} = FR_j\underline{\mathbf{f_j}}$$

$$\therefore FR_j = \phi_{jk}DP_k$$

The information presented in the $(\overline{\phi})$ tensor describes the interaction between FRs and DPs. Three different scenarios can be represented:

- Uncouple: The $(\overline{\phi})$ tensor is diagonal, and there is a one-to-one relation between FRs and DPs.

- Decoupled: If the $(\overline{\phi})$ tensor is triangular, Independence Axiom can be achieved if the DPs are arranged in a proper sequence through forwarding or backing substitutions.

- Coupled: Independence Axiom is violated, and a redesign of DPs is necessary to decouple the solution.

Once the DPs are defined, they lead to the actors necessary to accomplish functionality in the AM process.

3.1.2 Building of the interaction view with Design Structure Matrices

The start of the interaction view is when the DSM modelling tool is applied to represent the elements comprising the system and its interactions. With the information obtained from the AD, actors in the form of DPs are modelled in an n x n square

binary matrix representing the interaction between components considering an Input in Row (IR) convention [63]. Figure 3.2 shows the four possible configurations that characterize the interactions.

- Parallel: There is no interaction between DPs. Independence is ensured, and there is no information exchange between actors.

- Sequential: One actor has a unidirectional influence over another. The output of one actor is necessary for the next one.

- Reverse Sequential: It is similar to the sequential configuration, although the directionality changes. It shows a dependency between DPs.

- Coupled: Interdependent elements show a high interaction in which uncertainty is present. Cyclic dependency is not favourable to robust design.
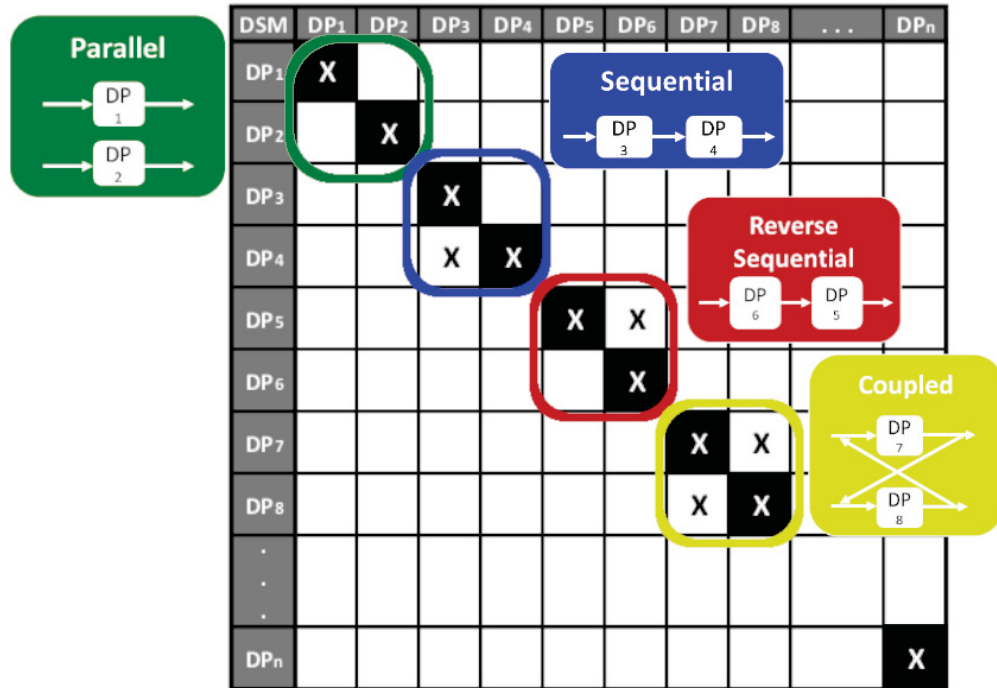
Figure 3.2: DSM Configurations: Parallel, Sequential, Reverse Sequential, and Coupled [64, 65].

Before proceeding to complement the information of the IFM interaction view, it is necessary to keep the interactions of the actors concurrent or dependent and avoid any interdependent interaction. This view is completed when outside resources or operands interacting with the system are annexed to the DSM.

3.1.3 Eventual Integrated Function Modelling

The interaction view enables the visualization of the processes for the machine. By building the actors' view, DPs that directly support operations and those that are being affected are shown.

AM systems must have a set of instructions to manufacture parts and these are displayed by the process flow view. These processes are executed sequentially to print products with the characteristics specified. Three main stages have been identified in the process flow of AM equipment: settings, printing, and shutdown. The first stage covers the machine setup and part preparation for the component being printed. The second stage is the main functionality of the system in which the components are 3D printed. The last step is intended as the finishing routine of the system.

The relations between processes and states in the actors and operands are obtained in the state view. Each DP and operand starts with an initial state which transits through four possible states during the process development: active, idle, support, inactive. This view gives more details regarding the contribution of each process into a shift of state in the actors and operands.

Finally, in the case view, the functionalities of the system are added. There might be some processes that are only functional to some instances and others common between cases. This view allows multi-functionality by letting the IFM expand without compromising the initially defined processes.

3.2 Case study

The methodology described above is implemented for the case study of a metal additive manufacturing system. The design modelling begins with the customer needs for new AM equipment. The system is intended to print a variety of advanced metal powders with suitable dimensions for the oil & gas industry, hence, components subject to wear and corrosion. It is important to print these components fast enough to be replaced and functional; therefore, lower resolution and higher deposition rates than in fused deposition modelling (FDM) are expected. Geometrical dimensions need to be guaranteed to keep the component's functionality, and particular mechanical properties need to be achieved.

Given the customer's needs, more specific and focused CNs were proposed considering the mechanical and physical properties described by the customer. These new CNs were linked to five functional requirements: frame of the system (F1), movement of building platform (F2), material transportation (F3), melting energy (F4), and material (F5). Table 3.1 shows the mapping transformation between CN and FR domains.

Initially, nine design parameters were selected with specific target values for each one of these actors:

1. Building space of 365 mm x 170 mm x 300 mm (DP_1).

2. Building platform movements above 500 mm/min (DP_2).

3. Hopper volume of at least 5 litres (DP_3).

Table 3.1: Mapping between CN and FR Domains.

CNs	FR_1	FR_2	FR_3	FR_4	FR_5
Strength					X
Hardness					X
Porosity			X	X	
Size	X				
Resolution		X	X	X	
Speed		X	X		
Bead width		X	X	X	
Bead height		X	X	X	

4. Powder feeding rate above 20 grams per minute (DP_4).

5. Powder gas flow above 1.5 standard litres per minute (SLPM) (DP_5).

6. Energy capable of reaching temperatures above 1000° C (DP_6).

7. Feedstock melting point above 1000° C (DP_7).

8. Hardness above 30 HRC (DP_8).

9. Porosity less than 1% (DP_9).

Design parameter number six was limiting the options for technology capabilities; therefore, it was decided to integrate a PTA system as an energy input source. This decision split DP_6 into three actors: arc current above 40 A ($DP_{6.1}$), center gas flow above one standard litre per minute ($DP_{6.2}$), and shield gas flow above 10 SLPM ($DP_{6.3}$). Figure 3.3 shows the interaction view built by using DSM modelling and re-organizing the actors by its configuration interactions.

Considering the three stages of AM equipment and the interaction view, twelve processes were proposed in the actors' view [Fig 3.4]. The X marks indicate that the
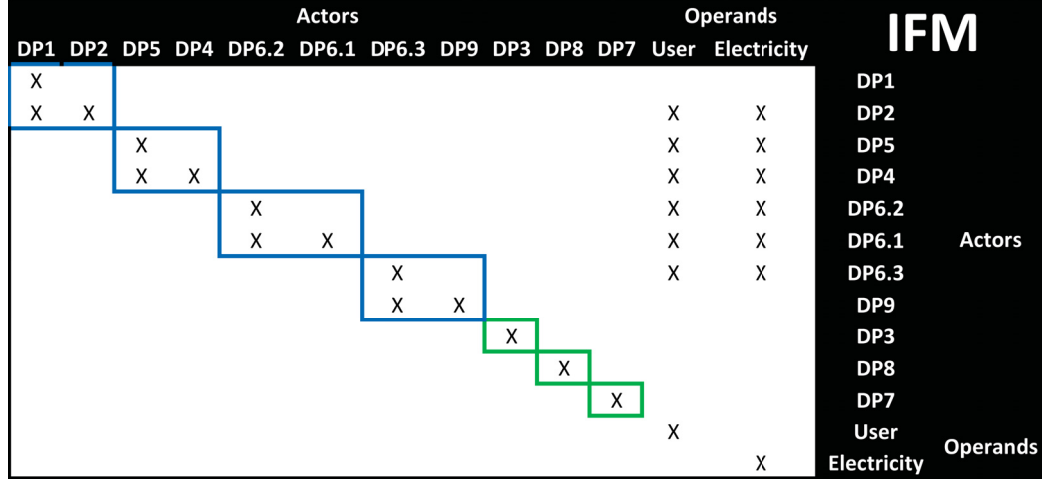
Figure 3.3: Interaction view in the IFM of the PTA-AM Case Study.

actor is directly supporting the process while the 0 marks imply that the actor is affected by it.

1. System on: initialization of the system and energy distribution (P_1).

2. Part geometry: load process of the computer-aided design (CAD) part to be printed (P_2).

3. Home routine: homing the building platform to have the initial reference in the coordinate axis (P_3).

4. G-code instructions: setting the commands for moving the building platform (P_4).

5. Load of material: the metal powder is added to the hopper (P_5).

6. Melting energy on: plasma arc welding is on (P_6).

7. Start material transportation: the material is feed from the hopper to the nozzle (P_7).

8. Melting: the melting process of the material underneath the PTA torch (P_8).

IFM	Settings				Printing				Shutdown			
	P1	P2	P3	P4	P5	P6	P7	P8	P9	P10	P11	P12
DP1		X	O	X					O			
DP2	X	X	X	X					X	X		X
DP5	O				O	X		O	O		X	O
DP4	O				O	X		O	X	X	X	O
DP6.2	O						X	O	O			O
DP6.1 Actors	X						X	X	X	X		X
DP6.3	O								X	X		O
DP9									X			
DP3				X								
DP8				X					X			
DP7				X				X	X			

Figure 3.4: Actors view of the PTA-AM case study.

9. Deposition: the deposition of the material in the substrate or over previously deposited layers (P_9).

10. End deposition: finishing 3D-printing a metal part (P_{10}).

11. Stop material transportation: stop the flow of the material (P_{11}).

12. System shutdown: turning off the system (P_{12}).

These processes are executed sequentially according to the information presented in the process flow view [Fig.3.5].

The state view presented in Figure 3.6 shows the transition of actors from its initial state to its corresponding state, depending on the processes and returning to its final state. It is shown that most of the DPs are supporting or active during the primary process, which is deposition (P_9). This process is where the 3D printing part is being manufactured.
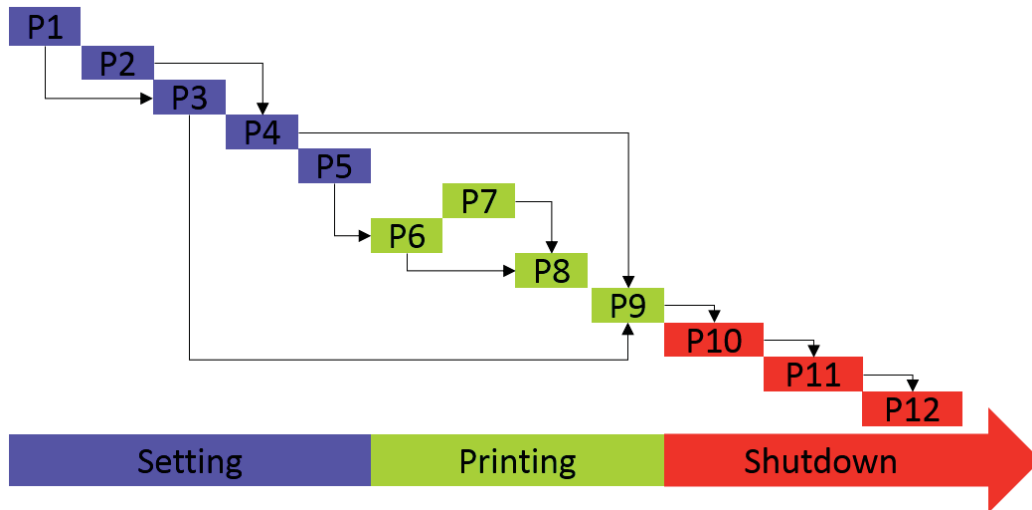
Figure 3.5: Process flow view in the IFM of the PTA-AM case study.

Figure 3.6: State view of the PTA-AM case study.

DP1	DP2	DP5	DP4	DP6.2	DP6.1	DP6.3	DP9	DP3	DP8	DP7	User	Electricity	
Active	Inactive	Inactive	Inactive	Inactive	Inactive	Inactive	Inactive	Idle	Inactive	Idle	Active	Idle	
	Idle	Idle	Idle	Idle	Idle	Idle						Active	P1
											Support		P2
Support	Active											Support	P3
											Support		P4
								Active		Active			P5
				Active	Active							Support	P7
		Active	Active					Support				Support	P6
		Support	Support	Support	Support	Active	Idle	Support	Idle	Support		Support	P8
Support	Support	Support	Support	Support	Support	Support	Active	Support	Active	Support		Support	P9
	Idle			Idle	Idle	Idle	Inactive		Inactive		Support		P10
		Idle	Idle				Idle			Idle	Support		P11
	Inactive	Inactive	Inactive	Inactive	Inactive	Inactive						Idle	P12
Active	Inactive	Inactive	Inactive	Inactive	Inactive	Inactive	Inactive	Idle	Inactive	Idle	Active	Idle	

Actors: DP1, DP2, DP5, DP4, DP6.2, DP6.1, DP6.3, DP9, DP3, DP8, DP7

Operands: User, Electricity

IFM

Although the use case view represents the different functionalities of the system, for this particular case study, a commercially-off-the-shelf (COTS) PTA system integrated with an in-house three axes motion control system was implemented. The case study contemplates a use case of the system printing metal matrix composites (MMC) suitable for the oil & gas industry. The complete IFM structure of the PTA-AM case study is depicted in Figure 3.7.
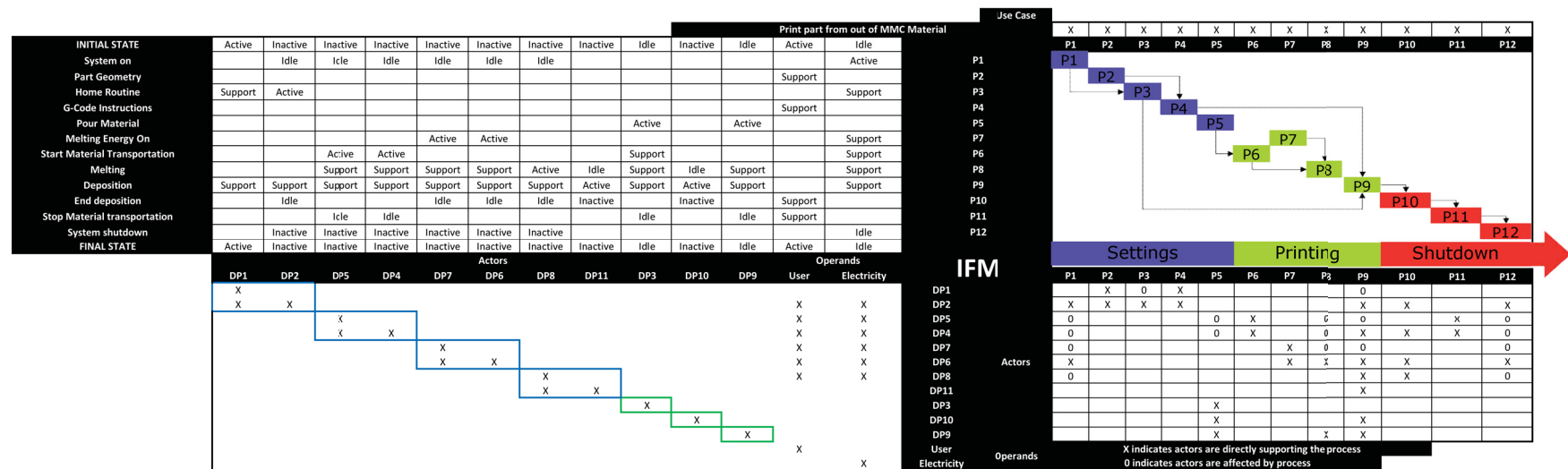
Figure 3.7: Complete IFM for the PTA-AM case study.

3.2.1   Use case view: Printing of metal matrix composites

Two separate systems supported the fabrication of the prototype for the IFM methodology. The first system is a Kennametal Starweld 400A PTA System. This system is adopted to overlay parts with advanced materials to improve wear resistance to components in the oil & gas industry. The second system is a three-axis motion control system that allows the building platform to move through a defined building space. Both systems were integrated through specialized software programmed to synchronize them to work as AM equipment. The functionality of the actors was obtained with the IFM systematic methodology. It can be noted that DP_1 and DP_2 correspond to the motion system, DP_2 to DP_6 are related to the PTA system, and DP_7 to the melting point of the feedstock material. The last two actors (DP_8 and DP_9) are characteristics of the printed parts, which are consequences of the AM process.

Figure 3.8 shows the design layers carried out to build the experimental setup. The integration of all the components demonstrated promising results as a new manufacturing system for metal AM. The next chapter provides further information about the characteristics of the printed parts.
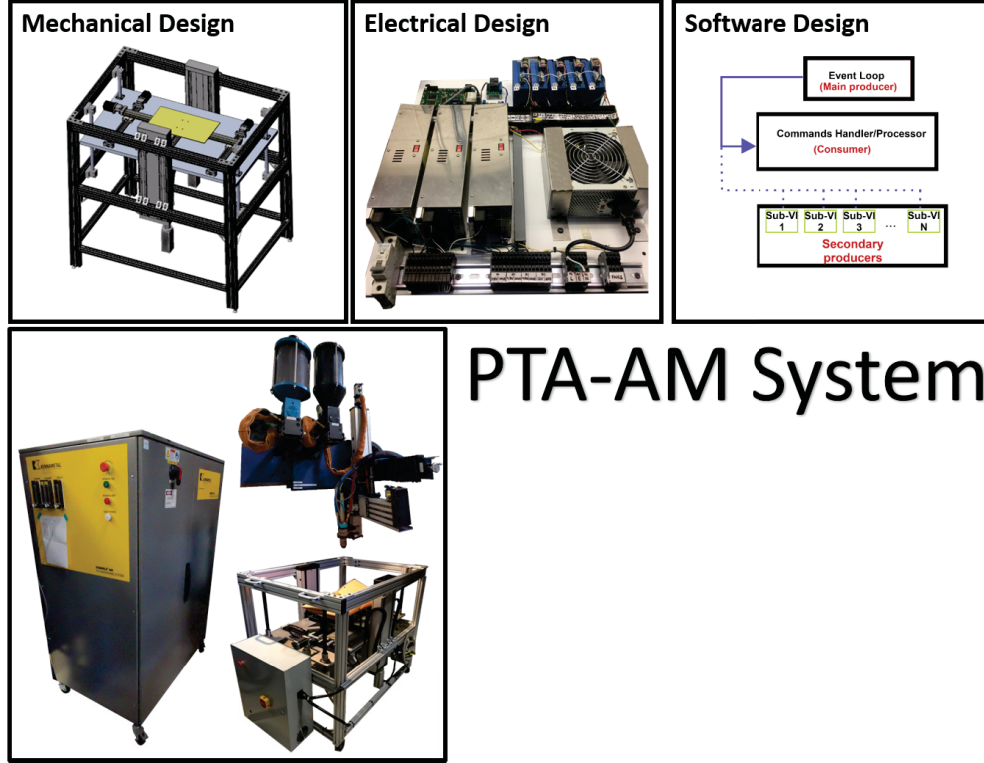
Figure 3.8: Integration of the different design layers in the PTA-AM system.

3.3   Conclusion

The development of methodologies for designing AM systems is necessary to facilitate the transition from concept to product. AM technology is advancing, and its uses are diversifying to meet the new challenges of industry. IFM has proven to be a practical framework by incorporating axiomatic design as basis. The evolution of the different views provides excellent insight for the components, and its constant iteration allows improvements during the progress of the modelling. More work needs to be done for consolidating more detailed design structures such as mechanical, electrical, and software design into the framework.

Future work in the PTA-AM case study endeavours toward improving the quality of the 3D printed part. By increasing the number of actors and processes, this method-

ology could contribute to generating the necessary support applicable for closed-loop feedback controllers for enhanced part geometry control. Additional DPs could address new characteristics expanding the IFM for new types of sensors (more on this in Chapter 5) and adaptations to propel the efficiency and productivity of the current system. Other use cases might include work using other types of materials or functionally graded components with a combination of different alloys during the deposition process.

3.4   Acknowledgements

Chapter 4

Plasma Transferred Arc Additive Manufacturing[1]

This chapter analyzes the geometric stability and microstructure characteristics of metal additive manufacturing parts using plasma transferred arc with metal matrix composites. The analysis is important because not all of the technology is suitable for the deposition of advanced materials. The technology used to enhance the capabilities of a plasma system to create an additive manufacturing system is described, and the initial experiments involve the 3D printing of two parts: one pyramid, and one cylinder. In order to determine how wear resistant the parts are, the geometric stability, microstructure porosity, and cross-sectional hardness of the additive manufacturing parts are analyzed and discussed for the initial deposition experiments. The work presented in this chapter aims to show that the capabilities of the PTA-AM system allow the building of 3D printed parts made of nickel-based metal matrix with tungsten carbide (WC) particles to increase the wear resistance.

This chapter also describes the effects of process parameters commonly used in plasma transferred, such as current, linear speed, powder flow rate, nozzle angle, and powder, shield and center gases at the macro-scale and micro-scale of single-track multiple-layer depositions. This work confirms the use of plasma transferred arc as

---

[1]Part of this chapter was published as a journal article in *Manufacturing letters* [66] and other part was accepted in *The Journal of Advanced Manufacturing Technology* [67]

an additive manufacturing system yielding enough energy for a fast solidification rate of the matrix without compromising the carbide in the composite. Mechanical performance in the printed part depends on the carbide characteristics. The results show that the bead height is mainly affected by the powder flow rate, the powder gas, and the travel speed at the macro-scale, and that the bead width has a close relationship with powder flow rate, powder gas, and current, the latter contributing to the formation of a slumping phenomenon due to heat accumulation. The results show the volumetric deposition is affected by similar parameters to those that affect the bead height. At the micro-scale, the deposition experiments did not result in significant carbide changes but rather validated its homogeneous distribution. The electron microscope observation exhibited the composite's high quality due to the fast solidification of the process. Results indicate that the porosity is mainly affected by the powder flow rate. By understanding the preliminary contribution of process parameters, this manufacturing process can be developed to print near net-shaped parts minimizing the post-processing of metal additive manufacturing components. Therefore, this work contributes to the body of knowledge by implementing a preliminary experimental methodology to understand the deposition process of WC-reinforced composites in plasma transferred arc additive manufacturing.

4.1 Introduction to plasma transferred arc technology

Plasma is a state of matter that is generated when a high concentration of energy ionizes a gas, and the gas is forced to conduct electric current [68]. Plasma arc welding (PAW) is an arc welding process that joins metals by heating them with a constricted arc [69]. This technology is generally divided into two working modes: plasma transferred arc (PTA) and plasma non-transferred arc (PNTA) [70]. In the first mode, the arc is electrically transferred to the workpiece. In the PNTA, the arc is constricted between the electrode and the nozzle [71]. The PTA mode is commonly

used to deposit thick overlays of high wear and corrosion-resistant alloys with high deposition speeds [72].

Figure 4.1 shows a cross-section of the plasma torch. Plasma gases are usually non-reactive, such as argon, helium, hydrogen, or a mixture of these [73]. A pilot arc is first initiated between the electrode (cathode) and the nozzle (anode) ionizing the gas that flows through the nozzle's exit orifice. When the transferred arc starts, the ionized gas decreases the electrode and the substrate's electrical resistance and forms a high-temperature, high-velocity plasma jet [74]. The arc is constricted using a water-cooled small diameter copper nozzle that allows a reduced arc diameter but an increase in the power density compared to other arc welding processes.
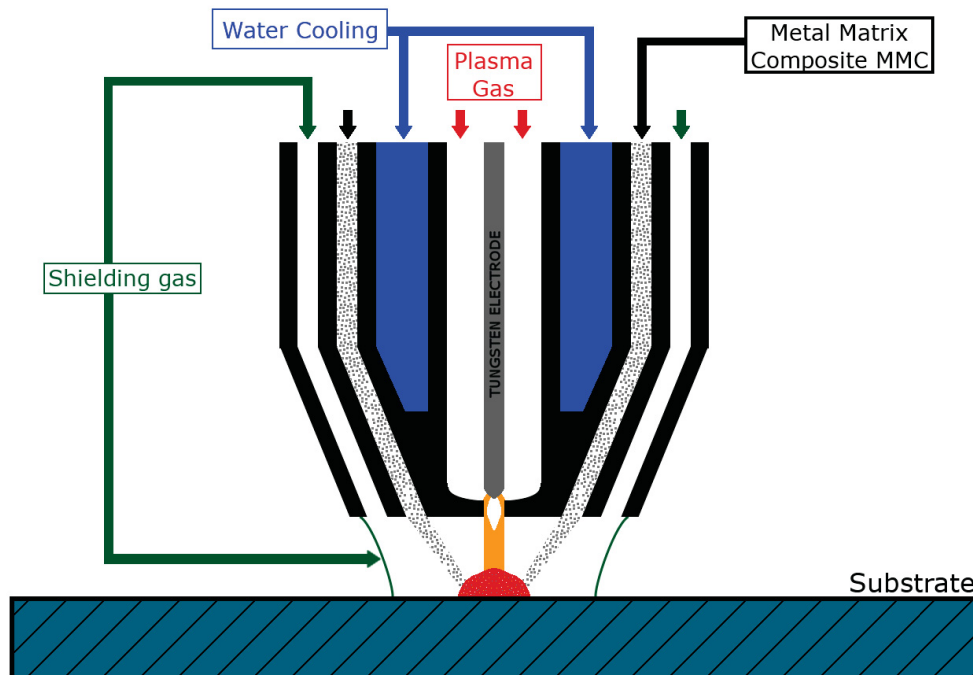
Figure 4.1: Plasma transferred arc deposition with powder delivery through the internals of the nozzle.

Some systems supply the feedstock in a variety of ways and forms, such as off-axis powder injection with ceramic tubes [75, 76, 77] or through a wire feeding system [46].

In this system, the feedstock is delivered through ports in a coaxial nozzle. The use of powders makes the process more flexible in terms of the alloys that can be deposited [11]. Finally, surrounding the deposition, a shielding gas is used to supply a protective environment to the melt pool [78].

4.2 Literature review

DED-AM are non-equilibrium processes with fast cooling rates, a diverse set of processing parameters coupled with complex transportation phenomena bears to a difficulty in understanding the particular effects of process parameters [79]. Generally, the determination of process parameters in new AM systems consists of trial-and-error round-robin tests. Artaza et al. [80] designed and integrated a Wire and Arc Additive Manufacturing (WAAM) system to print Ti-6Al-4V components. The validation of the technique required a combination of 83 single depositions varying feed rate, current, and wire feed speed for a single material. Although these tests can determine the working conditions for the system, further knowledge is required to achieve near net-shaped components [81]. Understanding the role of these variables in metal AM deposition improves the printing quality of components. In PTA-AM, the combination of process parameters such as current, linear speed, powder flow rate, nozzle angle, and powder, shield and center gas flows leads to particular characteristics. The metal deposition rates and quality, different penetration levels into the substrate, losses of powder material, and specific bead height and width are characteristics dependant on process parameters achievable rapidly in a single pass [82].

Although the design of experiments (DOE) techniques are typically used for detailed investigations, Taguchi-based experimentation is a particular technique that allows a quick understanding of parameter's effect in previously unexplored processes [83]. This preliminary analysis provides the foundations of which parameters to focus on for detailed testing. This guideline allows a preliminary investigation of

different parameters, their ranking, and their influence on the process. Comparable type of experiments have been used to investigate the deposition rate in twin-wire submerged arc welding [84] and tungsten inert gas welding [85]. Similarly, DOEs have been used to link process parameters to bead characteristics in laser cladding [86, 87, 88] and plasma cladding [89]. Wilden, Bergmann, and Frank [90], and Parekh, Buddu, and Patel [91] used the experiments for multiphysics simulation in PTA welding and laser cladding, respectively. Other researchers analyzed the effects of process parameters in the bead geometry through transient studies [92, 93].

In terms of metal AM for DED systems, the previous research on PTA used as an additive manufacturing is limited [94, 66]. However, in relevant systems such as laser and wire-and-arc additive manufacturing (WAAM), process parameters have been analyzed through DOEs. Table 4.1 provides insight into the input and output criterion for laser beam experiments. It is important to note that laser beam observations mainly centers on stainless steel. Standard process parameters are laser power, laser velocity, and powder feed rate. In the outcome measures, the bead geometry, such as width and height, are typically investigated.

Table 4.1: Literature review for process parameters in laser beam systems.

Reference	Process parameter	Outcome measures	Material
[95]	-Laser power -Laser velocity -Preheating temperatures -Part geometry	-Melt pool size -Grain size -Residual stress	304 stainless steel
[96]	-Laser power -Laser velocity	-Bead height -Bead width -Dilution	303L Stainless steel

In the laser DED reaserch, Beuth and Klingbeil [95] described the use of a process map approach for the relationship between process parameters and critical deposition parameters such as melt pool size, residual stress, and grain size. In Fathi et al. [96], a theoretical model was linked to the numerical results from the evaluated experiments. A case study for building airfoils with three-, and four-way nozzles was conducted by Qi, Azer, and Singh [97] showed a central composite design to drive the experiments. Additionally, Angelastro et al. [98] described the comparisons between a mathematical model and the results of multi-layer claddings built with MMC composites. A finite element model in single-track single-layer beads was applied by Amine, Newkirk, and Liou [99] to compare the experimental results and to obtain temperature readings, microstructure analysis, and microhardness and grain size measurement. Saqib, Urbanic, and Aggarwal [100] used experimental results to build a prediction model through ANOVA, lumped parameters, and artificial neural networks. Single- and multiple-layers depositions were employed to build contour plots correlating process parameters to thin wall structure height [49].

Table 4.3 presents similar information as Table 4.1, but for WAAM systems. Wire feed speed is a standard parameter along with the studies. In these cases, alloys' availability is limited to commercially wire forms. Prado-Cerqueira, Diéguez, and Camacho [101] implemented a hybrid process to metal 3D printing and milling for surface finishing components. The results from more than 100 experiments related the process parameters to bead height and width. In Liberini et al. [102], the research focused on comparing microstructure and mechanical properties by varying the input parameters. Porosity in single-track multiple layers beads is measured and evaluated considering different manufacturing process parameters and material batches [103]. Furthermore, by building thin walls, Zhang et al. [47] created AM transverse and longitudinal tensile tests linking process parameters with ultimate tensile strength and grain maps.

Table 4.2: Literature review for process parameters in laser beam systems continuation.

Reference	Process parameter	Outcome measures	Material
[97]	-Laser power -Defocus distance -Powder feed rate -Travel speed -Height increment -Shield gas flow	-Wall thickness -Layer height	Inconel 718
[98]	-Laser speed -Hatching space X -Hatching space Z	-Bead width -Bead height -Deposition efficiency	30% Colmonoy 227-F 70% WC/Co/Cr
[99]	-Laser power -Traverse speed -Powder feed rate	-Hardness -Temperature and solidification ratio -Grain size -Temperature -Bead height	316L Stainless steel
[100]	-Laser power -Powder feed rate -Laser speed -Focal lenght -Contact tip distance	-Bead width -Bead height -Penetration -Positive area -Negative area	P420 Stainless Steel
[49]	-Pulse energy -Pulse duration -Transverse speed -Height increment	-Bead width -Bead height -Penetration -Deposited area	301L Stainless Steel

Table 4.3: Literature review for process parameters in WAAM systems.

Reference	Process parameter	Outcome measures	Material
[101]	-Welding speed -Current -Arc correction -Dynamic correction	-Bead height -Bead width	AWS ER70S-6 cooper coating
[102]	-Voltage -Speed rate	-Grain size -Microhardness	AWS ER70S-6
[103]	-Wire batches -Power modes -Wire feed speed -Travel speed	-Porosity size distribution	Aluminum alloy 2319
[47]	-Arc mode -Heat input -Interlayer wait-time -Scanning speed -Current -Voltage -Wire speed	-Maximum width -Effective width -Porosity -Grain maps -Ultimate tensile strength	AL-6Mg alloy

Other types of energy sources were analyzed in Table 4.4. Travel speed, power-related parameters, and material deposition rate were standardized process parameters, while bead height and bead width were outcome measurements.

In Wang et al. [82], voltage information controlled the arc length in μ-plasma, and their system built functionally graded components. Likewise, Jhavar, Jain, and

Table 4.4: Literature review for process parameters in other DED systems.

Type of energy source	Reference	Process parameter	Outcome measures	Material
μ-plasma	[82]	-Current -Speed -Powder feeding rate	-Layer height -Layer width	H13 tool steel powder
	[50]	-Power -Travel speed -Wire feed rate	-Bead width -Bead height -Deposition quality	P20 tool steel wire
	[104]	-Power -Flow Rate of Powder -Travel Speed -Stand off distance -Plasma gas flow rate -Shield gas flow rate	-Bead width -Bead height -Quality of deposition	Ti6Al4V powder
Plasma wire deposition	[105]	-Wire feed speed -Travel speed -Current	-Wall width -Effective wall width -Layer height	Ti6Al4V wire
Electron beam	[106]	-Power -Travel velocity -Wire feed rate	-Beta grain widths -Melt pool area	Ti6Al4V wire

Paul [50] correlated the parameters of multiple layer depositions to quality deposition and characteristics such as surface waviness, deposition efficiency, and microhardness. Moreover, Sawant and Jain [104] investigated the coefficient of friction, wear volume variation, lamellae width, and microhardness. In plasma wire deposition, Martina et al. [105] studied a cubic behaviour with three-factor third-order polynomial function to fit experiments and obtain a working envelope.

This chapter aims to prove PTA-AM technology to be suitable as an AM system. The research presented herein aims to develop a preliminary understanding of process parameters' influence in the bead geometry and the microstructure of WC-reinforced composites through the use of PTA-AM. The next section describes the materials and methods for the experiments. The section details the analyzed process parameters, the Taguchi-based DOE model, and the acquisition of outcome measures.

4.3 Materials and methods

4.3.1 Initial experimental set-up

The initial approach to build a plasma transferred arc additive manufacturing system (PTA-AM) was to employ a Starweld 300 M commercial off-the-shelf (COTS) plasma system from Stellite Coatings and an in-house built positioning device. This PTA system is commonly used globally, and it is an excellent candidate for the adaptation of current technology into 3D printing technology, allowing the equipment to be multi-functional. This technology enhancement is considered a directed energy deposition (DED) system, specifically a free form fabrication system [107]. The PTA equipment was used for metal cladding of components in the oil & gas industry, and it is set up with a Kennametal Excalibur torch. The Kennametal nozzle and all modern PTA hardfacing torches have powder delivery through the internals of the nozzle.

The system comprises of 4 main parts. The PTA enclosure is were the controller, and all the valves and electronics are located [Fig. 4.2A]. The Excalibur torch is at the transition point where the metal powder is carried by the argon and melted by the plasma arc [Fig. 4.2B]. For AM purposes, a three-axis position device was adapted. It should be noted that the torch is fixed, and the build platform moves according to the AM part geometry.

The build platform is the location where the substrate is mounted to print a part [Fig. 4.2C]. The platform can move in the build space of 365 mm x 170 mm x 300 mm through its x, y, and z axes, respectively [Fig. 4.2D]. A real-time DSP-Based system is used with a computer numerical control (CNC) interface to control the table movements by the G-Code standard RS-274NGC. The printing process starts with a 3D model in Standard Tessellation Language (STL). The model is converted then to layers by the slicer software CURA to generate the first set of G-code instructions under the standard RS-274. Before the printing process, a parsing of the code is required to convert the G-code to its extended version RS-274NGC. This language has many capabilities beyond those of RS-274, and that is the type of data that the PTA-AM positioning device uses to coordinate the movements required to print the parts. The design for the positioning device guarantees a steady movement without stalling for components weighing up to 80 kg. The linear actuators installed in the z-axis direction have electrically controlled breaks with a resolution of 12.5 μm per stepper count and uncertainty of ± 0.1 μm [Fig. 4.3].

Initial experiments method

The material for these experiments is a DURIT 6030 40% NiCrNSi Nickel Alloy with 60w% of WOKA 50115 WC particle concentration. Table 4.5 shows the configurations used for the initial trials. In this run, the process parameters were restricted to
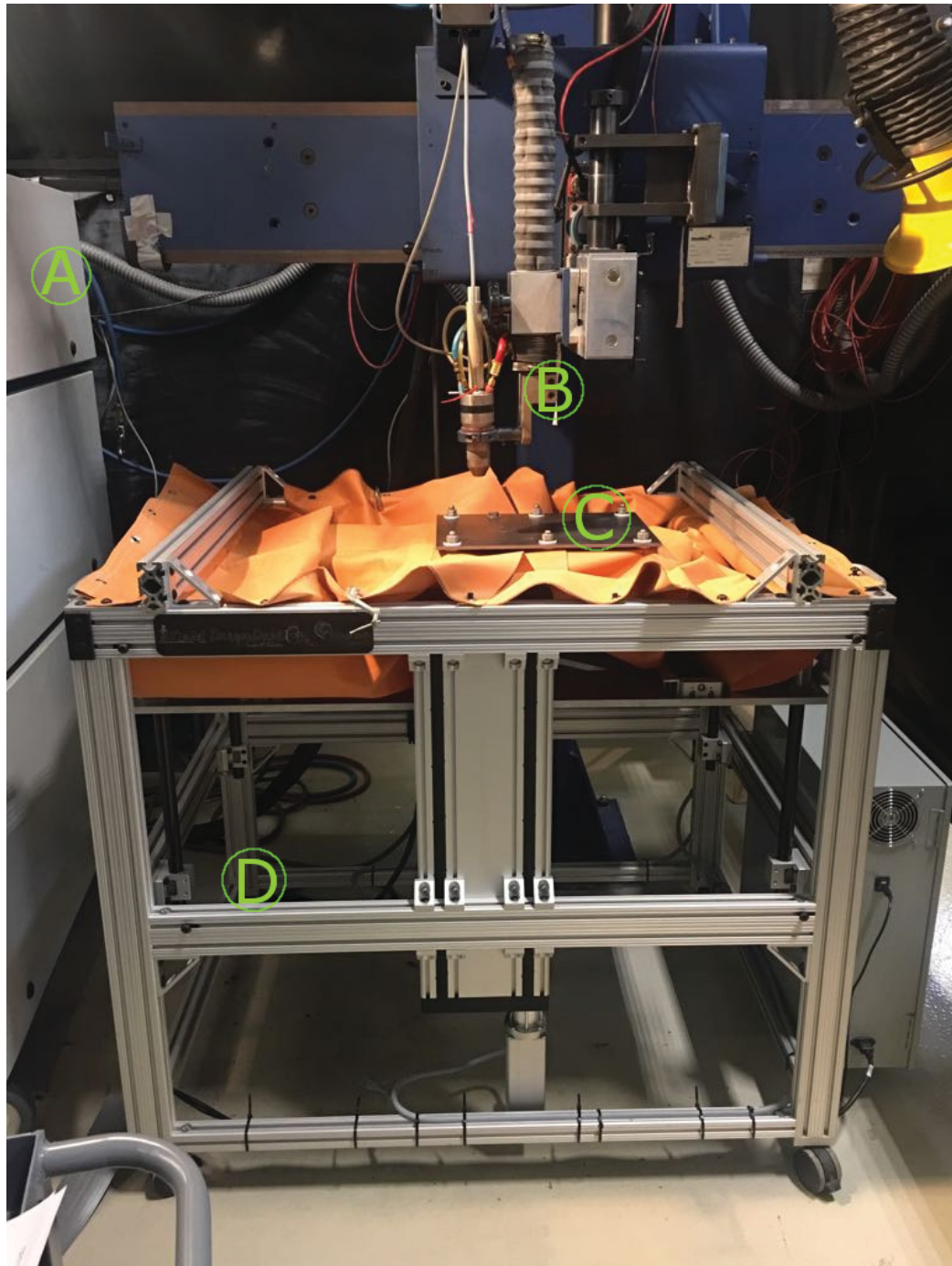
Figure 4.2: PTA-AM system. PTA Enclosure(A), Excalibur torch(B), build platform(C) and build space(D). Explanations are provided in the text of the paper.
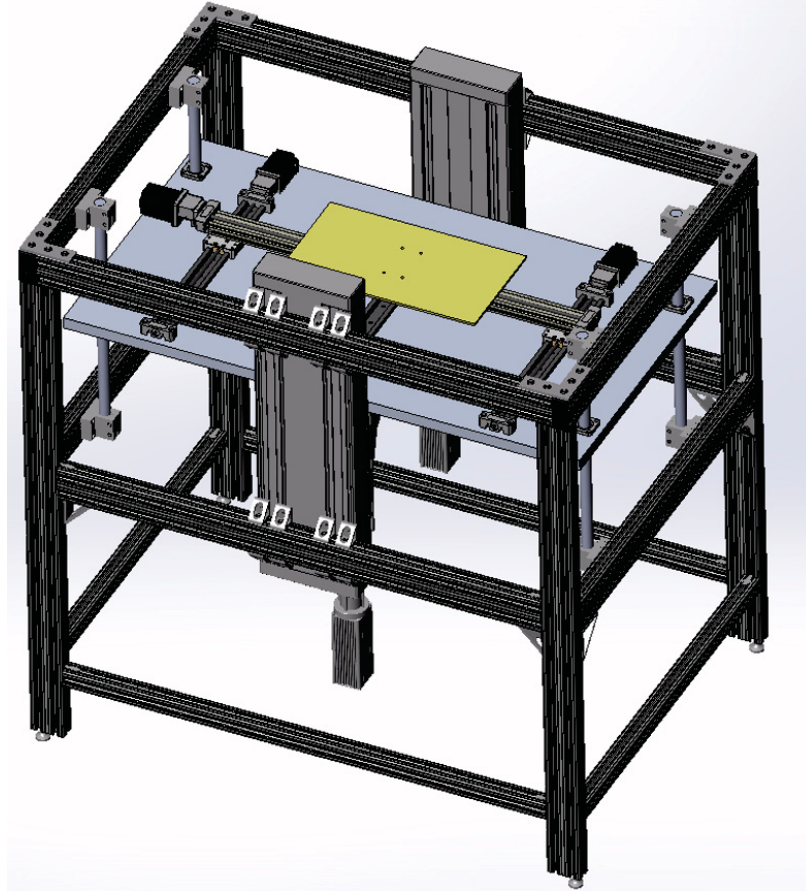
Figure 4.3: Computer-aided drawing of the positioning device.

the lower end of the capabilities to ensure a successful run. Process parameters can be increased for other purposes, e.g.achieve higher speeds. The selected values were based on Wolfe (2010) to ensure the tungsten carbide particles' homogeneity inside the MMC [69].

Table 4.5: Plasma transferred arc AM process parameters for inital experiments.

Center gas	1 GPM
Shield gas	12 GPM
Powder gas	1.5 GPM
Powder Feed Rate	20 GPM
Pilot Current	24 A
Welding Current	48 A
Voltage	23 V
Powder Size	50-180 μm
PTA-AM Table Speed	10 mm/sec

The PTA system is limited regarding the information we can collect during the experiments, therefore, in order to acquire more data during the printing process and assess it, a second version of the PTA-AM system is devised and further experiments are undertaken.

4.3.2 Second version of the PTA system

The second version of the PTA-AM system is depicted in Figure 4.4. It consists of a Kennametal Stellite™ STARWELD 400A PTA system. It is an updated version of the Starweld PTA 300 M designed for general-purpose, multi-faceted, hard face production though the spread of fully fused metal deposits. Similarly to the previous PTA, the metal powder is carried from a powder feeder to the torch in an argon stream. The powder stream transports the material into the plasma, where it is melted and fusion bonded to the workpiece. A direct current power source provides the energy for the transferred arc across a tungsten electrode. The new PTA has an improved control system with the digital capabilities to be integrated and communicated with other systems and sensors. For the hardfacing PTA system to work as an AM system, the same 3-axis coordinated positioning device shown previously is positioned under

the torch while the torch travel remains fixed. The PTA positioning device yields the flexibility to move on a build space envelop of 365 mm x 170 mm x 300 mm through its x, y, and z axes, respectively. Standard g-code instructions developed using standard open-source methods are used to generate the positioning device's path trajectory. The new capabilities allow seamless integration between the deposition process in the PTA, the travel of the positioning device, and the data acquisition for monitoring purposes in the sensors.

Figure 4.4: Second version of the PTA-AM System.

The material, in powder form, is poured in the hopper. The powder flow rate is calibrated prior to deposition to ensure the rate in grams per minute is within the nominal range for the particular type of powder. The calibration is conducted at the start of every deposition run, and confirmed in triplicate. The powder density and morphology are correlated to the powder flowability, as such, the powder flow rate calibration is critical.

The temperature of the plasma can reach more than 24,000 K [74]. Therefore, a cooling mechanism is necessary to prevent damages to the nozzle. A cooler of model Koolant Kooler JHI-1500-M is connected to the torch allowing ∼18% propylene glycol

in water to flow with a pressure of 551.58 kPa (80 psi). A thoriated tungsten electrode is sharpened to the angle of 20° and is set back 4 mm inside the torch nozzle. Two different torches were used in the experiments: the Excalibur PTA torch and the model 600 torch. The Excalibur torch was installed with a 3.18 mm (1/8") nozzle suitable for small to medium applications. The plasma plume is slightly smaller than 4.76 mm (3/16"), which provides better bead control. The 600 torch was installed with a 2.38 mm (3/32") long nose nozzle for low power applications. Table 4.6 provides the technical specification for each torch.

Table 4.6: Operational ranges for the Excalibur and 600 torches.

Nozzle description	Weld current	Powder flow rate	Center gas flow	Electrode	Shield gas flow
	Amperes	grams/min	SLPM	Size (dia.)	SLPM
Excalibur torch standard 3.18 mm (1/8") 2 port	20 - 180	20 - 70	1 - 2	3.18-4.76 mm 1/8" - 3/16"	10 - 15
600 torch long nose 2.38 mm (3/32") 2 port	20 - 80	10 - 40	0.8 - 2	3.18 mm 1/8"	10 - 15

Although different torches and nozzles were used, the location of the powder exit port in the nozzle with respect to the deposition direction must be considered. Figure 4.5 shows the three cases considered for the experiments implemented in the new PTA version: 0, 45, and 90 degrees. The PTA positioning device lies under the fixed torch. An initial position for the building plate is set in the G-code to allow its movement into the single-track multiple-layers deposition.
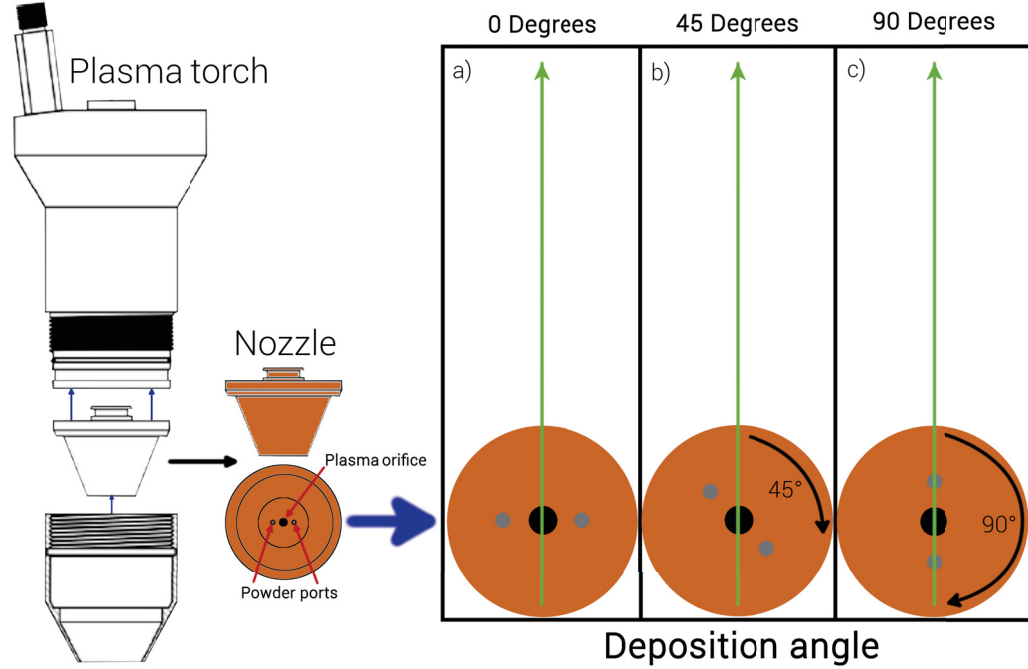
Figure 4.5: Nozzle's angle in relationship with the deposition direction a) 0 degrees, b) 45 degrees, and c) 90 degrees. The arrows indicate the travel direction.

Second version method

Figure 4.6 shows the path planning strategy to minimize the deposition collapse at the ends of the layers [108, 109]. The length in the path planning corresponds to 130 mm, while the height for 27 layers. The transition distance between layers in the z and x directions at the ends of each track is 0.75 mm and 3.5% of the length, respectively.

The powder is a pre-blended mixture of tungsten carbide and a nickel alloy sourced from Œrlikon Metco [110] and the trade name is PlasmaDur 51122. This powder contains monocrystalline Tungsten Carbide with Nickel-Chromium Boron Silicon powder. The morphology of the carbide is angular, while the matrix is spheroidal. Nominal particle size distribution is +63 to -180 μm, with a nominal apparent density of 5-6.5 g/cm^3. Table 4.7 presents the chemical composition ranges of the hard phase and the matrix alloy.
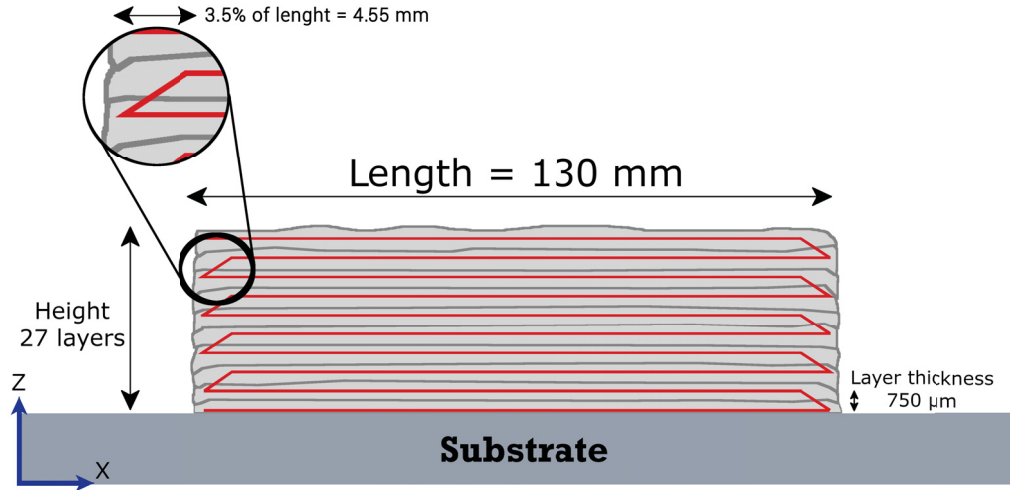
Figure 4.6: Single-track multiple-layers deposition strategy.

Table 4.7: Chemical composition ranges of the metal matrix composite.

Product	Hard Phase Composition (wt. %)			Matrix Alloy Composition (wt. %)						
	Phase %	W	C	Phase %	Ni	Cr	B	Si	C	Fe
PlasmaDur 51122	60	93.8 94.0	6.0 6.2	40	Bal.	9.5 12.5	2.0 2.5	3.3 4.3	0.3 0.6	2.0 3.5

The substrates are 152.40 mm x 152.40 mm x 6.35 mm (6" x 6" x 1/4") hot-rolled flat bars made of ASTM A36 steel [Table 4.8]. The plate is washed with an industrial cleaner to remove residual oils before getting sandblasted. An Empire Pro-Finish® cabinet with a #36 mesh brown aluminum oxide grit at a pressure of 551.58-620.53 KPa (80-90 psi) is used to obtain a near-white metal surface finish in the substrates [111].

Table 4.9 lists the PTA-AM process parameters, the corresponding capability ranges, and the level values evaluated in this preliminary experimentation method.

Table 4.8: Chemical composition of the substrate [112].

wt%	C	Cu	P	Si	S	Fe
ASTM A36 steel	0.26	0.2	0.04	0.4	0.05	Bal.

A fixed value of 7 mm was selected for the stand-off-distance.

Table 4.9: Process parameters, ranges, and DOE levels.

Process parameter	Value range	DOE value
Torch type	*Excalibur or 600 torch*	(P1) **L1:** Excalibur **L2:** 600 torch
Powder gas	*1-4 slpm*	(P2) **L1:**1.5 **L2:** 2 **L3:** 2.5
Shield gas	*10-15 slpm*	(P3) **L1:** 10 **L2:** 12.5 **L3:** 15
Center gas	*1-2 slpm*	(P4) **L1:** 1 **L2:** 1.5 **L3:** 2
Nozzle's angle	*0°-90°*	(P5) **L1:** 0° **L2:** 45° **L3:** 90°
Powder flow rate	*20-40 grams/min*	(P6) **L1:** 20 **L2:** 30 **L3:** 40
Current	*20-80 A*	(P7) **L1:** 40 **L2:** 50 **L3:** 60
Printing Speed	*50-4,000 mm/min*	(P8) **L1:** 500 **L2:** 600 **L3:** 700

A Taguchi-based DOE model method was used to analyze preliminary the effect of the process parameters on the build geometry and internal quality. The assessment includes eight process parameters considering seven factors with three levels, and one factor with two levels. Table 4.10 shows the L18 orthogonal array used for the experiments. The experiment consisted of depositing 18 multi-layer single track samples with orthogonal combinations of the process parameter levels. As stated in the deposition strategy, each sample aims to measure 130 mm in length, and 27 layers in height. To be considered an acceptable experiment, the bead sample must complete all the G-code instructions through a continuous deposition of all the layers; otherwise, it is unacceptable. To characterize the as-built parts, a Struers Discotom-65 diamond saw sliced each sample into four cross-sections. As an outcome measurement, the weight of a one 20 mm section is employed. The remaining three sections were ground and polished up to 0.05 microns to observe any internal porosity and metallurgical defects.

The Taguchi method provides information about the contribution of process parameters to specific outcomes [83]. Consequently, the outcome have a specific goal which is quantifiable through the signal-to-noise ratio (SNR) measurements in decibels-isotropic (dBi) units. The resultant values measure the variability to a nominal or target value under different conditions depending on the goals of the experiment. The outcome measures and the goals expected from the 18 runs are:

- Bead height: The height through the bead is measured for the cross-sections. The goal is to maximize the deposition; hence, the height. Equation (4.1) describes the larger-the-better signal-to-noise ratio [113] goal:

$$\eta = -10Log_{10}\left(\frac{1}{n}\sum_{i=1}^{n}\frac{1}{Y_i^2}\right) \tag{4.1}$$

where n is the number of observations in each experiment, and Y_i is the observed measurement.

Table 4.10: L18 Taguchi orthogonal array combinations.

Runs	Process parameters levels							
	P1	P2	P3	P4	P5	P6	P7	P8
1	1	1	1	1	1	1	1	1
2	1	1	2	2	2	2	2	2
3	1	1	3	3	3	3	3	3
4	1	2	1	1	2	2	3	3
5	1	2	2	2	3	3	1	1
6	1	2	3	3	1	1	2	2
7	1	3	1	2	1	3	2	3
8	1	3	2	3	2	1	3	1
9	1	3	3	1	3	2	1	2
10	2	1	1	3	3	2	2	1
11	2	1	2	1	1	3	3	2
12	2	1	3	2	2	1	1	3
13	2	2	1	2	3	1	3	2
14	2	2	2	3	1	2	1	3
15	2	2	3	1	2	3	2	1
16	2	3	1	3	2	3	1	2
17	2	3	2	1	3	1	2	3
18	2	3	3	2	1	2	3	1

- Bead width: The outcome measurement is multiple measurements of the bead width on each of the runs for the different cross-sections. The goal is to obtain a nominal value, and the variance around this value can be considered the result of the noise factors. This goal searches for standardized width through the deposition, consequently, the importance of numerous measurements. The nominal-the-best signal-to-noise ratio [113] is described as:

$$\eta = 10 Log_{10} \left(\frac{\mu^2}{\sigma^2} \right) \tag{4.2}$$

where η is the signal-to-noise ratio, μ is the mean of the measurements, and σ^2 is the variance.

- Bead Weight: Similarly to bead height, the goal for the weight outcome measurement is to build up a more substantial deposition. Therefore, a larger-the-better signal-to-noise ratio strategy is required. The difference with the bead height outcome is the amount of data collected since only one 20 mm in length cross-section is weighted for each experiment.

- Porosity: In contrast, to ensure that we are maximizing the mechanical properties for the heavy-duty industry (i.e. wear and corrosion resistance), the internal porosity needs to be reduced. Accordingly, the outcome measurement is the porosity percentage of the cross-sections. The internal porosity was calculated using the software ImageJ. Image processing techniques are required to differentiate between pores and WC particles. As a signal-to-noise ratio [113], a strategy of smaller-the-best is depicted in Equation (4.3):

$$\eta = -10 Log_{10} \left(\frac{1}{n} \sum_{i=1}^{k} Y_i^2 \right) \tag{4.3}$$

4.4 Results and discussion

4.4.1 Results and discussion for the initial experiments

Two 3D printed parts made of DURIT 6030 Nickel Alloy with 60wt% of WOKA 50115 macro-crystalline tungsten carbide were obtained from the experiments, one part is a pyramid and one part is a cylinder. By visual inspection of the similarities between

the CAD model and the printed components, it is confirmed that this manufacturing process is feasible for AM purposes. Although the machine is capable of printing components up to 150 mm, two small test artifacts were chosen for validation purposes only. A pyramid with 60-degree angles and a total height of 50 mm was selected to show some degree of over-hang. A cylinder with a 50 mm diameter and 30 mm height was determined to exhibit annular capabilities. Figure 4.7 shows the results of the two printed parts in which geometric stability is achieved. The pyramid's printing time is 13 minutes, and the cylinder has a 2 minutes printing time. Both shapes have a layer thickness of 750 μm.
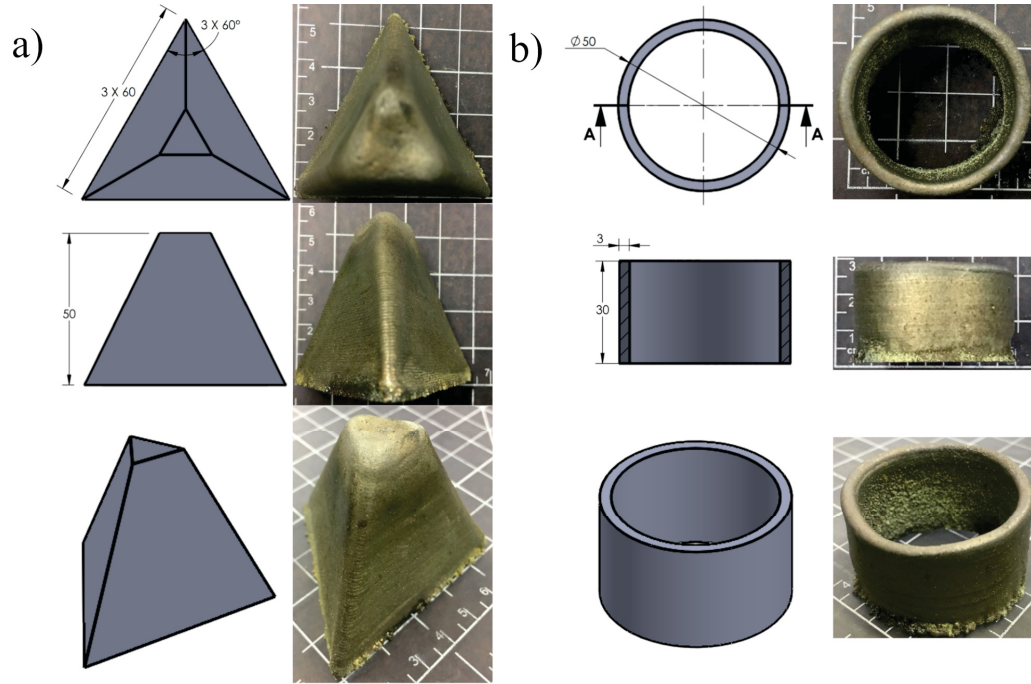
Figure 4.7: Geometric stability for the pyramid (a) and the cylinder (b) in mm (top, front and isometric views).

One particular problem in standard overlays used in the hardfacing industry is the settling of WC particles due to their high density. In this study, a cross-sectional analysis of the 3D printed cylinder part was obtained to have more insight into the effects of the PTA-AM process in the microstructure evolution. The pyramid was preserved

for exhibition purposes. The analysis in the cylinder shows that the homogeneity in the WC particles distribution remains constant due to the rapid solidification in the layer-by-layer AM process [Fig. 4.8]. This rapid solidification occurs because of the meagre building rates noticed in the microstructure that allow the nickel matrix to prevent the settling of the denser WC particles. The even distribution of the particles allows balanced mechanical properties, and the printed parts are less prone to failure or wear.
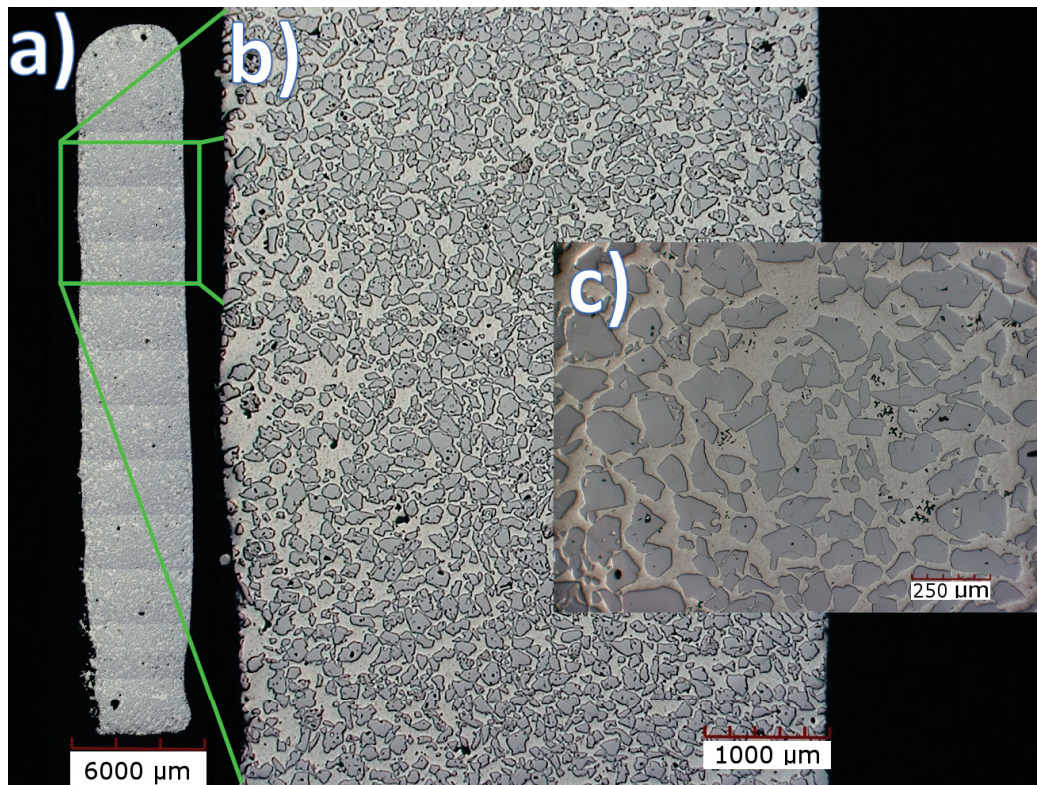
Figure 4.8: 3D printed cross-section a) 6 mm scale, b) 1 mm scale, and c) 250 μm scale.

Comparing the CAD model with the physical model, the nominal value of the total height of the cylindrical part was 30 mm, compared to the real value of 32 mm measured through the microscopic evaluation. The nominal value of the wall thickness of the model was 3 mm. The measured shell thickness average is 4.7 mm, with a standard deviation of 0.339 mm, taken over 63 discrete locations through the build.

The porosity was measured using a false colour technique with image analysis software Clemex 9.0 at seven locations. The average porosity from the seven sections is 0.40%, with a standard deviation of 0.161%. The porosity in the microstructure is due to the lack of metal fusion inside the matrix, as well as internal porosity intrinsic to the tungsten carbide. It was observed that the porosity increases on the last layers of the AM part. This characteristic is highly correlated to heat management in the build, particularly an effect known as heat buildup. It is known that travel speed contributes to higher residual stresses and distortions within the build [87]. Thermal modelling before beginning the building is suggested to reduce porosity. Finally, for the WC hardness, ten random locations inside particles from the cross-section were selected. The measurements where performed through a hardness rockwell C (HRC) methodology. The HRC measurement average is 63.06 HCR, with a standard deviation of 0.73 HCR. This information reveals that the hardness in the microstructure aligns with the conventional hardfacing overlay results. There are no indicators in the microstructure showing the growth of the WC particles. There is little interaction between the carbide and the metal matrix. Table 4.11 shows a summary of the results obtained.

Table 4.11: Summary results for geometric stability, microstructure porosity, and cross-sectional hardness in the cylindrical part.

Parameter	Nominal	Measured	Standard Deviation
Height	30.00 mm	32.00 mm	-
Shell Thickness	3.00 mm	4.70 mm	0.34 mm
Porosity	-	0.40%	0.16%
Hardness	31.00 HRC	63.06 HRC	0.74 HRC

Based on the results shown in Table 4.11, it is observed that the variance in height and shell thickness is higher by 6.67% and 56.67%, respectively. These differences

are due to specific perturbations in the initial layers caused by the copper nozzle's diameter, the initial stand-off distance of the torch, the center, powder, and shielding gas flows, the powder flow rate, the welding current, and the travel speed. The optimization of these process parameters contributes to a better metallic fusion in the printed part. Other possible alternatives to decrease these perturbations, based on the experience in cladding, are pre-heating the substrate before printing, decreasing the nozzle diameter, standardizing the stand-off distance, and characterizing of the powder deposition.

4.4.2 Results and discussion for the experiments in the second PTA system

The DOE was used for all of the configurations shown in Table 4.10. During the 18 runs, the combinations that result in unaccepted experiments were further designated as defects using a classification which is described as follows:

A) **No deposition**: In this category, runs 6 and 17 have a powder quantity of 20 grams per minute. The amount of feedstock material is not enough to generate mass for the formation of a melt pool. In runs 9, 14, and 16, the current input is 40 A. The amount of heat input in these runs is not enough to melt the MMC and create a deposition.

B) **Intermittent deposition**: The category A is characterize by no deposition due to the powder and heat input influences. However, if the travel speed is reduced, more energy is input per volume unit. Run 1 has a low powder quantity and current, but it has as well low travel speed. The low speed allows the generation of a melt pool, but it is not enough to generate coalescence for a continuous deposition, and the deposition is intermittent. This phenomenon is better known as the balling effect. For runs 12 and 13, the powder quantity

is low (20 grams per minute), but the nozzle generates a more concentrated plasma than the Excalibur torch due to the center bore reduction. The increase in heat input allows the melt pool generation but not enough for a continuous deposition.

C) **Collapse due to heat accumulation**: In runs 3, 4, and 18, the heat input is the highest (60 A). This amount of energy input generates a heat accumulation in the deposition. As the printing continues, the thermal build-up keeps increasing to the point that the melt pool spreads, producing a bead's slumping, hindering the increment in layer thickness and increasing the bead width.

D) **Over-deposition**: The layer thickness for all the experiments is 750 μm to keep a constant increase in the z-axis. If the deposition of metal powder increases, on each layer, the stand-off-distance will decrease. For run 5, the nozzle angle at 90 degrees and the low travel speed (500 mm/min) produces an increment in the deposition. For run 8, the low speed produces a raise in the deposition.

The lack of deposition, such as in defects A to C, increases the stand-off-distance, increasing the process voltage. The distance increment induces a rise in the voltage, which generates unstable plasma operation for the PTA. Over-deposition, on the other hand, can create a short-circuit due to the low stand-of-distance between the torch and the deposit. Table 4.12 shows a summary of the experimental results.

Figure 4.9 shows the cross-section results for the successful experiments (runs) number 2, 7, 10, 11 and 15. These images provide the information to measure the bead height, width, and porosity. Each image was calibrated with the corresponding scale bar and taken from the left, middle, and right sections.

Table 4.12: L18 Taguchi orthogonal array combinations results.

Run	Result	Comment
1	Defect type B	Intermittent deposition due to balling effect
2		Collapsing at ends of track
3	Defect type C	Collapse due to heat accumulation
4	Defect type C	Collapse due to heat accumulation
5	Defect type D	Over-deposition
6	Defect type A	No deposition
7		One side collapse and uneven height
8	Defect type D	Over-deposition
9	Defect type A	No deposition
10		Uneven height and width
11		Shorter and fewer deposition
12	Defect type B	Intermittent deposition due to balling effect
13	Defect type B	Intermittent deposition due to balling effect
14	Defect type A	No deposition
15		Unstable deposition and uneven width
16	Defect type A	No deposition
17	Defect type A	No deposition
18	Defect type C	Collapse due to heat accumulation
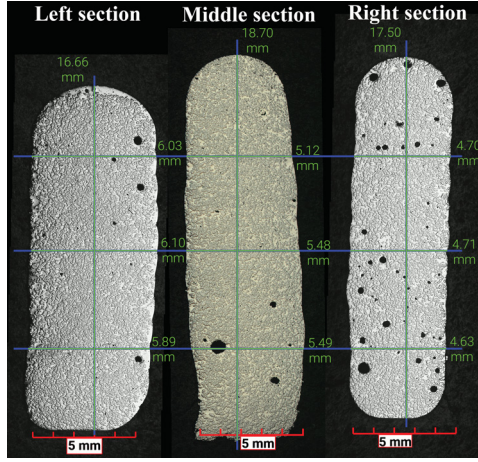
(a) Run 2
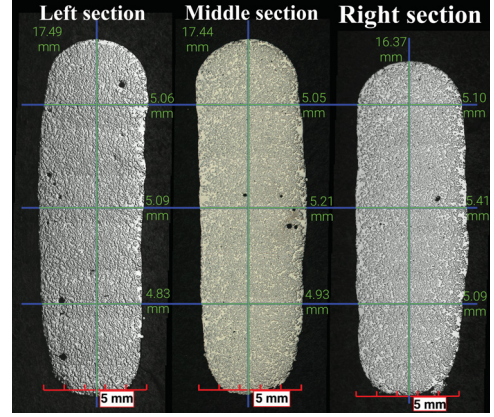
(b) Run 7
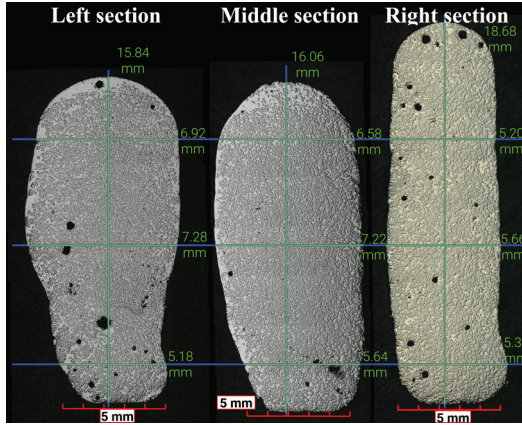
(c) Run 10
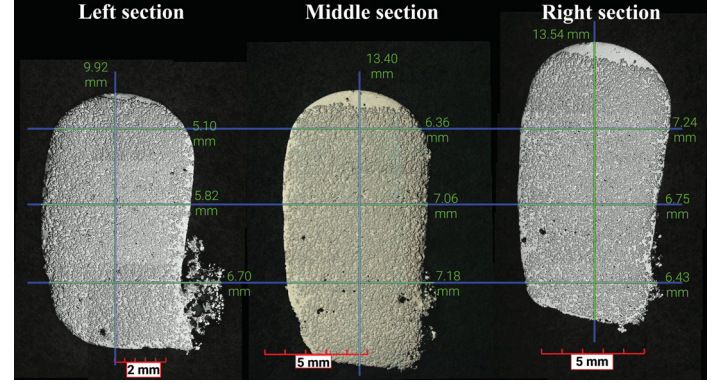
(d) Run 11
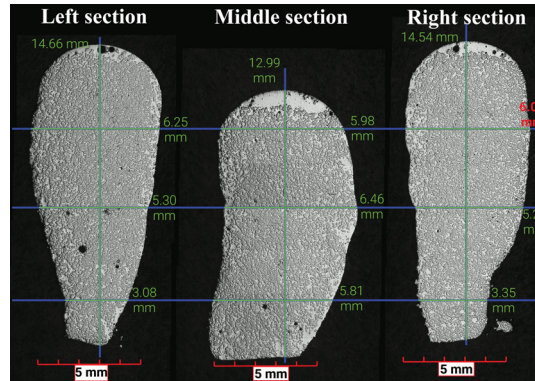
(e) Run 15

Figure 4.9: Single-track multiple-layers cross-sections results.

In the case of run 2 [Fig. 4.9a], although the width of the bead is steady, the middle section has higher deposition than the ends of the bead. This observation is consistent with the macro-scale information of the collapsing at the end of the track as shown previously in Table 4.12. This effect is common in single-track multiple-layers beads due to the deposition collapse at the ends. The deposition at the ends of the beads is continuous; therefore, thermal strain increases at the ends, causing this type of distortion as reported in Mukherjee et al. [114]. Additionally, porosity is higher in the right section, and some WC particles are settling on top of the left section. These are indicators of higher settling rates of the carbide which has a significantly higher density than the metal matrix. This carbide free region at the top can be minimized with higher solidification rates and/or lower overall heat input.

For run 7 [Fig. 4.9b], the bead is homogeneous among the sections, and less porosity is observed compared to run 2. Although the results are good at this scale, on the macro-scale, one side is collapsed in right section, and a notable increment in height through the bead is detected. The one-sided phenomenon can be linked to the perturbations of the start of the plasma arc. Higher powder flow gas can generate turbulent flows hindering the deposition in the transition to a steady-state.

In the case of run 10 [Fig. 4.9c], the bead's width shows significant differences in the cross-sections. Higher porosity is present at the ends, while WC settling is in the left and middle sections. It is essential to highlight that from all the samples, this bead was not attached to the substrate, indicating poor bonding between the bead and the substrate. As the heat flow from the bead out to the substrate, deposition was hindered due to lack of bonding, and the left section shows a slumping effect due to heat accumulation. At taller builds, stable heat distribution plays an important role in maintaining geometric consistency [115, 116].

Figure 4.9d illustrates the results of run 11. Through the sections, carbide settling is observed. This phenomenon is an indicator of the slow solidification of the Nickel matrix due to heat accumulation. Another consequence of thermal build-up is the geometry deformation. The sample exhibits a broader and shorter shape compared to other samples. A low dilution with the substrate is the rationale for this anomaly.

Run 15 is depicted in Figure 4.9e. Considerable carbide settling is identified at the top of the middle section. Left and right sections display slumping events with moderate WC settle.

Figure 4.10 shows the descriptive statistics for the bead width in the successful experiments. Run 2 exhibits better width stability based on its standard deviation, while run 15 is the more unstable. Run 15 has higher powder and shield gas than run 2, which can influence the stability of the deposition. Moreover, the speed in run 15 is slower, yielding to higher heat concentration notable on the green oxide attached to the bead.

For the Taguchi DOE preliminary analysis, the software Statistica™ was used. Table 4.13 shows the SNR results considering their respective goals providing a vision of each run's performance towards the outcomes; higher SNR means better performance. Information from defect samples in the height and weight analysis were manually measured and considered towards the study. Due to the defects, the data could not be calculated for width and porosity outcomes. Their signal-to-noise ratios were replaced with zeros as a standard for unacceptable samples. This standard works as a boundary baseline condition to prevent any undesired contributions from the defective specimens.
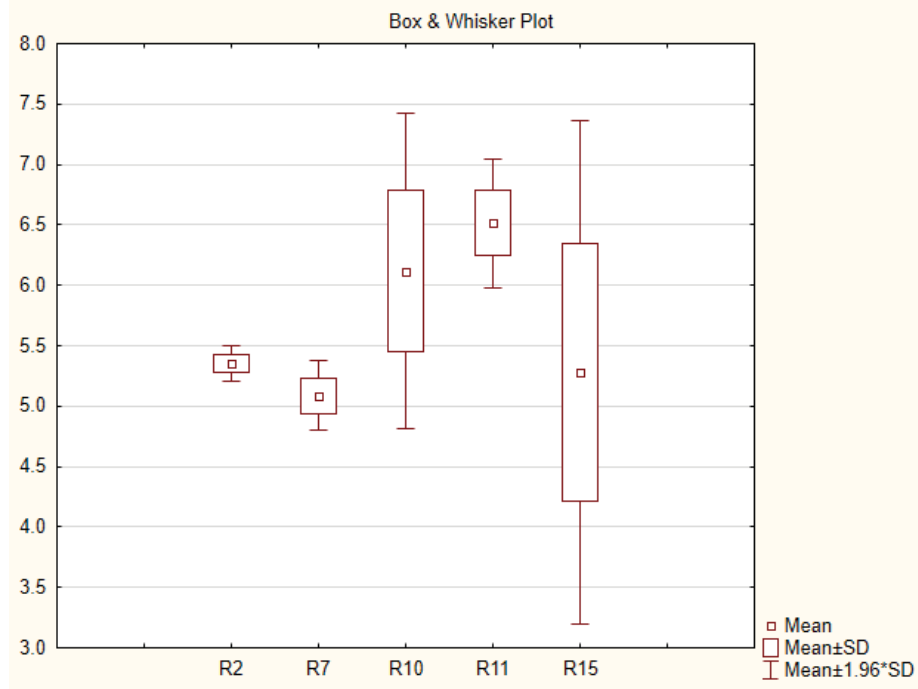
Figure 4.10: Descriptive statistics for the bead width.

Figure 4.11 shows the mean plot results for the outcome variables. These graphs represent how susceptible are the responses to the process parameters. Figure 4.11a demonstrates that the powder flow rate (by 34%), powder gas (by 21%), and travel speed (by 17%) have a more significant impact on the bead height. The results prompt that in order to increase the bead height, more material is needed. Additionally, higher deposition rates can be obtained by decreasing the travel speed. Width standardization is principally affected by current (by 36%), powder flow rate (by 19%), and powder gas (by 17%) (Fig. 4.11b). An even heat distribution during the deposition process is essential to standardized width. A high current produces heat accumulation and deformations; low current generates low dilution and unstable deposition. In the results of the weight, it is interesting to identify that similar process parameters to bead height are influencing the outcome: powder flow rate (by 29%), powder gas (by 25%), and travel speed (by 12%). Moreover, other parameters such as center gas (by 11%) and current (by 10%) became more meaningful (Fig. 4.11c). Similarly, increment in weight is closely related to higher deposition shown by the

Table 4.13: Signal-to-noise ratio results in dBi.

Run	Height	Width	Weight	Porosity
1	19.20	0.00	14.30	0.00
2*	24.89	37.15	22.79	-2.57
3	21.93	0.00	16.36	0.00
4	15.94	0.00	5.98	0.00
5	23.73	0.00	15.80	0.00
6	15.08	0.00	10.03	0.00
7*	24.65	30.96	22.75	6.48
8	16.31	0.00	9.03	0.00
9	10.98	0.00	-4.07	0.00
10*	24.47	19.22	22.72	-1.26
11*	21.51	27.61	22.46	5.84
12	14.73	0.00	11.39	0.00
13	13.20	0.00	10.69	0.00
14	10.17	0.00	-0.70	0.00
15*	22.92	13.92	19.81	5.58
16	16.19	0.00	15.46	0.00
17	4.24	0.00	-5.55	0.00
18	17.97	0.00	11.84	0.00

The star (*) elements indicate the accepted experiments.

comparison between the height and weight mean plots. Regarding the porosity, the powder flow rate is the parameter with the most substantial effect by 52%, followed by the nozzle angle (by 19%) and the center gas (by 16%) (Fig. 4.11d). Results indicate that higher deposition rates lead to lesser voids in the bead. Interestingly, a zero degree angle generates a symmetrical deposition reducing the probability of process-induced porosity [117]. By reducing the center gas, less gas can become entrapped within the melt pool, and the porosity is decreased [118].
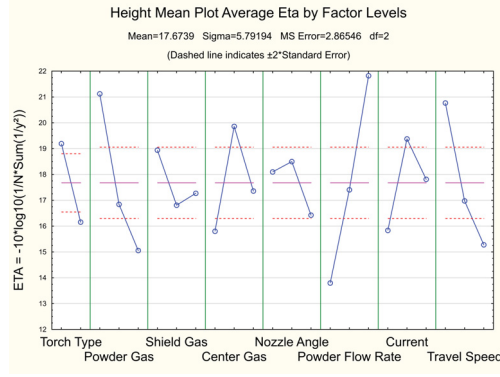
(a) Height
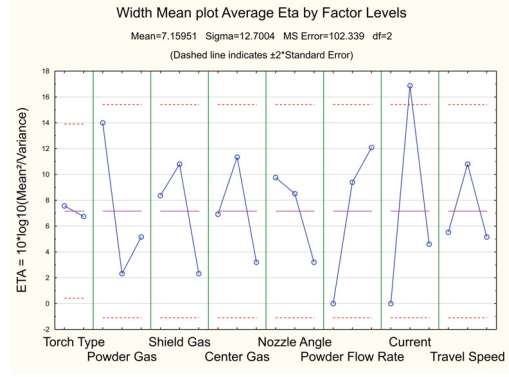
(b) Width
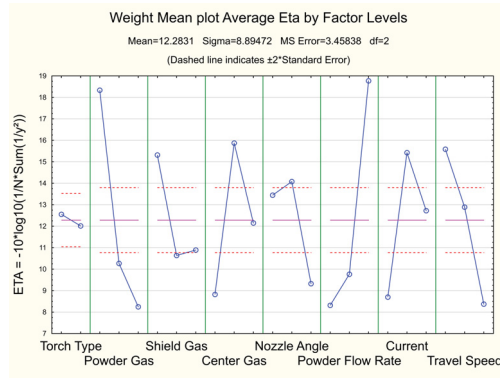
(c) Weight
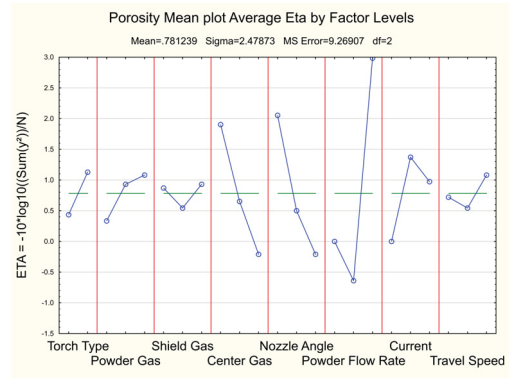
(d) Porosity

Figure 4.11: Mean plot results for the Taguchi design of experiments.

The information obtained from the mean plots provides a combination of recommended process parameters for a better performance of the desired output. Table 4.14 shows the proposal of the process parameter's combinations and the analytically calculated signal-to-noise ratio. The recommended process parameters obtained in this preliminary work are a stand-off-distance of 7 mm using the Excalibur torch, a powder gas flow of 1.5 SLPM, a shielding gas flow of 10 SLPM, a center gas flow of 1.5 SLPM, a nozzle's angle of 45 degrees, a powder flow rate of 40 grams/min, a current of 50 A, and a travel speed of 500 mm/min to achieve an overall increment in the SNR.

Additional analysis of the samples in the micro-structural domain were completed. Figure 4.12 shows the micrograph results for run 15 at two different magnifications.

Table 4.14: Process parameters combinations to improve the height and weight, width, and porosity.

Outcome measure	P1	P2	P3	P4	P5	P6	P7	P8	Expected SNR dBi
Height Weight	1	1	1	2	2	3	2	1	35.86 39.96
Width	1	1	2	2	1	3	2	2	43.11
Porosity	2	3	3	1	1	3	2	3	7.06

A uniform distribution of tungsten carbide particles in the nickel matrix was observed without a significant degradation of the tungsten carbide particles. The results exhibit that changes in the process parameters do not affect significantly carbides in the envelope of ranges that the experiments were executed.
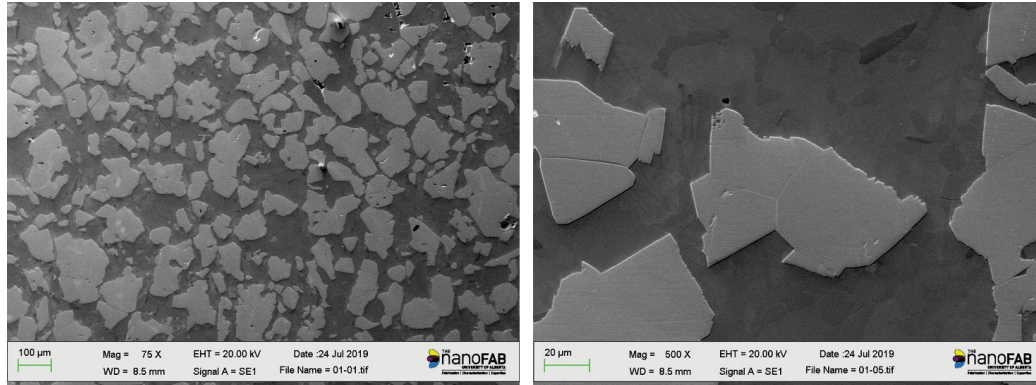
Figure 4.12: Micrograph analysis of run 15. The tungsten carbide distribution is even without carbide degradation.

The energy dispersive spectroscopy (EDS) elemental maps of the as-built composite are illustrated in (Fig. 4.13a). In addition to W-enriched particles (tungsten carbides), some small Cr-enriched particles can be observed. It is important to remark that the EDS spectrum of silicon (Si) overlaps with the tungsten carbide (WC) spectrum, showing Si inside the carbide which is not the case. This artifact is intrinsic to the EDS and other analyses are required. To determine the phase of these par-

ticles, X-Ray diffraction (XRD) analysis was conducted. From XRD pattern of the composite (Fig. 4.13b), the Cr-enriched particles were found to be $Cr_{23}C_6$. Moreover, Ni_3Si and Ni_3B phases were detected by XRD, whose formation was attributed to the presence of Si and B in the nickel alloy matrix. Regarding the spectrum overlap, the XRD demonstrates the absence of WC-Si composition validating the spectrum overlapping in the EDS. The micrographs, the EDS and XRD results are expected for this type of material.

(a) Chemical analysis

(b) X-Ray diffraction analysis
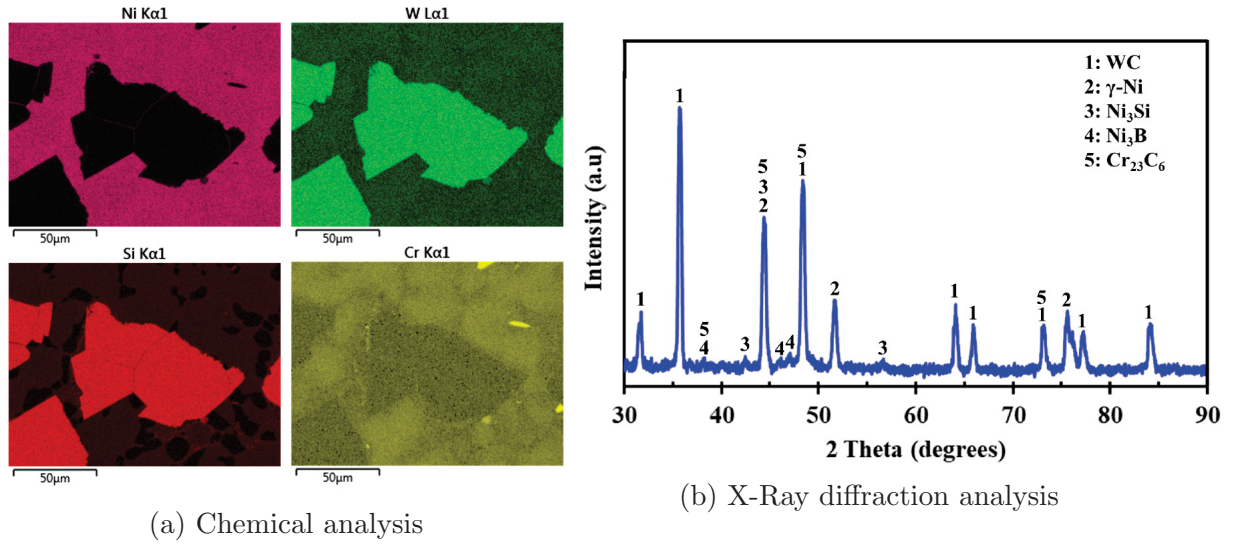
Figure 4.13: Micro-scale analyses, (a) shows the chemical composition at the micro-scale of a MMC representing the elements by color intensity, (b) shows the XRD analysis of the same component where the peaks correspond to the detected metal compositions.

4.5 Validation

Three samples were printed with the obtained process parameters combinations of Table 4.14. Figure 4.14 shows the front, sides, and top views of the selection for height and weight recommended parameters (Fig. 4.14a), for width's recommended parameters (Fig. 4.14b), and for porosity recommended parameters (Fig. 4.14c). Qualitative observations disclose improvement results for the height and width outcomes. The

sample made with the recommended parameters for height and weight shows a higher bead with some perturbation on top due to the nozzle angle's deposition effect. The side views show some instability during the building of the layers. The sample for the width's recommended parameters shows a steady bead width through the layers. In the case of the porosity results, the travel speed increment caused a lack of continuous coalescence in the bead producing columnar depositions. This phenomenon was not presented in any of the 18 runs. Runs 1, 12, and 13 made a balling effect, although the travel speed was 500, 700, and 600 mm/min, respectively. The powder flow rate used in these runs was too low to allow the columnar deposition (20 grams/min). The columnar deposition was not expected, and for that reason, the measurement and comparison of the porosity sample could not be obtained.

With the aid of a Sick™ laser profilometer, twelve points were selected to measure bead height and width quantitatively. For the height and weight bead combination, the average height was 24.20 mm with a standard deviation of 0.34 mm, and the average width was 6.23 with a standard deviation of 0.33 mm. Regarding the width bead combination, the height averaged 22.87 mm with a standard deviation of 0.21 mm and the width 5.40 mm with 0.13 mm of standard deviation. In the case of the porosity bead combination, average height was 19.18 mm with a standard deviation of 8.86 mm, and width averaged 5.39 mm with 1.13 mm of standard deviation. A 20 mm section was sliced for each bead and weighed. The values obtained were 18.67 g, 17.71 g, and 8.62 g for height and weight combination, width combination, and porosity combination, respectively. Figure 4.15 exhibits the descriptive statistics for height and width through the samples showing that the height and weight combination provides a better bead height (Fig. 4.15a) and the width combination a less deviation in the bead width (Fig. 4.15b).

(a) Results from recommended combination to improve height and weight.
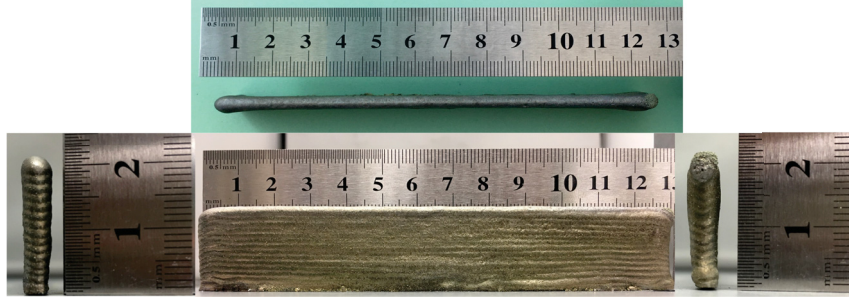
(b) Results from recommended combinations to improve width.
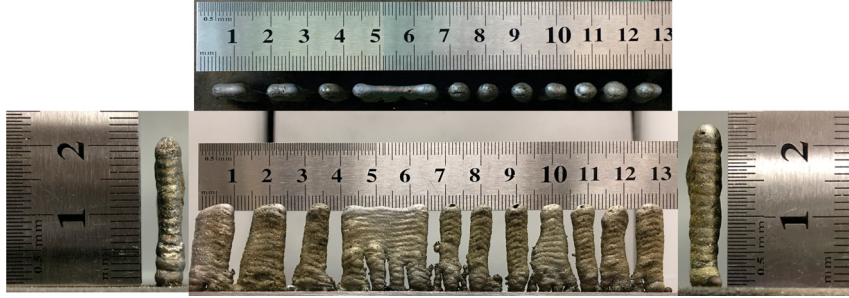
(c) Results from recommended combinations to improve porosity.

Figure 4.14: Results from recommended combinations to improve outcomes.

Quantitative information confirms that the height and weight combination improves the respective outcomes. The height difference between the height and weight combination and the width combination is of 5.82%, which can be because of the additional perturbations that the height and weight combination exhibits due to the nozzle orientation. Similarly, the weight difference is of 5.42%, and it is due to the additional deposition in the sample. On the other hand, the height and width combination has 26.17% more height and 1.16 times more weight compared to the porosity combination. Comparing it to the best result in the experiments, the height and width combination result improves by 29.41% the height and by 35.39% the weight.
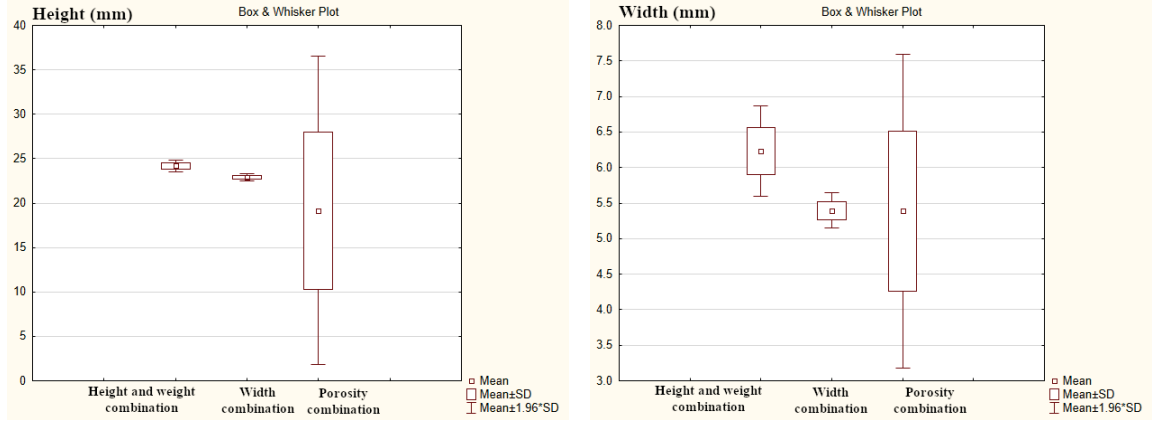
(a) Height results in recommended combina- (b) Width results in recommended combina-
tions.   tions.

Figure 4.15: Descriptive statistics results for the height and width in the recommended combinations.

Regarding bead width, the standard deviation in width recommended combination is 60.61% less than the standard deviation of the height and width combination. Additionally, the bead width combination's standard deviation is 88.63% less than the porosity combination's standard deviation. That confirms that the width recommended parameters has less variance and standardized width through the deposition.

From the data collected in the recommended results, the SNR for the height, width, and weight can be calculated as 27.67 dBi, 40.09 dBi, and 25.42 dBi, respectively. It is demonstrated that the method worked for improving the height SNR by 11.19%, the width SNR by 7.9%, and the weight SNR by 11.55%.

4.6   Conclusion

The PTA-AM technology is a DED method that uses plasma energy to melt MMC with valuable mechanical characteristics for heavy industry applications. The expectation of this technology is to 3D print critical components, such as bucket teeth,

crushers, shovel or cyclofeeders from a CAD model instead of overlaying them with the MMC. A combination of steel and hard-facing powders will improve the strength, toughness, hardness, abrasion and corrosion properties of the components. The process can melt a variety of alloys together with tungsten carbide particles because of its high energy. The features that make this AM system beneficial include the possibility of high printing speeds, the mechanical properties that can be achieved with the variety of material combinations, and the capacity to print customizable parts.

Higher printing speeds will allow the system to build large-scale additive manufacturing (LSAM). Building sizable components in the fusion AM processes is a challenge. As shown in the microstructure analysis of the parts, build-up heat and thermal stresses can lead to porosity, distortions and warping of the parts. These effects can be reduced through thermal modelling of the process, process parameters optimization, or improving the PTA-AM technology through closed-loop control strategies. Addressing these difficulties will allow the system to improve its building rate. The work here shows that the PTA-AM parts homogeneity in WC particles is due to the rapid solidification because of the combination of low building rate and travel speed.

This chapter also provided a methodology through the Taguchi-based design of experiments for preliminary understanding the repercussion of process parameters in geometrical and microstructural characteristics. The SNR in the outputs provide an overview of the performance toward the goals. The results showed the importance of an appropriate bonding between the part and the substrate to allow stable thermal dissipation. Heat accumulation induces perturbations in the build-up process producing deformed structures such as those seen in the recommended process parameters for the porosity. This slumping effect hinders the deposition process and increases the solidification time. For metal composites with considerable different densities, a

decrease in the cooling rates results in settling of the denser reinforcement particle, which can lead to poor performance in service.

Bead height and weight are mainly affected by the powder flow rate, the powder gas flow rate, and the travel speed. These outcomes are coupled, the higher the deposition, the more material is in there; hence, an increment in weight. There is no coupling with the width because the outcome goal is to minimize the variance, not maximizing the width. A rise in the deposition takes effect by increasing the material flow input and reducing the travel speed. Parameters such as current and powder flow rate, greatly influence the fluctuation of the bead width. As stated previously, a higher current generates overheating of the bead warping it. A low powder flow rate or low current inhibits the deposition process due to a lack of material or energy respectively. Lowering these parameters generates a balling effect or no deposition. The plasma shape also affects the bead width with different stand-off-distances, but this work kept that parameter fixed. Concerning the porosity, the results depicted a direct correlation between high powder flow rate and low porosity, although given the outcome in the recommended parameters, the results must be taken with prudence. The anomaly might be originated due to process-induced effects such as the turbulent flow under the torch. The phenomenon will later be analyzed by the use of high-speed cameras to add further information to this matter. One process parameter was consistent with being crucial to every outcome, the powder flow rate. The upper limitation of 40 grams per minute on the 600 torch limits the maximum amount of powder flow; hence, further experiments require increased flow rates by using the Excalibur torch, so the 600 torch is not suitable for the AM applications.

The PTA-AM process exhibits generally uniform carbide distribution though the deposition height. The results display a high quality of the composite after the printing process as seen with the low carbide degradation within the analyzed operational

ranges. Therefore, this advanced manufacturing process is suitable for application in the heavy-duty industry where wear is a concern. The methodology validates the impact of process parameters into quantifiable outcomes to understand the deposition process and achieve near net-shaped components.

Chapter 5

In-situ measuring strategies for PTA-AM

5.1   Introduction

The adoption of additive manufacturing (AM) in the last decade has generated a trend towards developing technology and capabilities considering the future of connectivity. The introduction of Industry 4.0 and the Internet of Things (IoT) requires the acquisition of reliable data sources to be analyzed which makes manufacturing analytics more important than in past decades [119]. In this sense, the integration of sensors into the AM processes provides a collection of data to compile information and to improve the quality characteristics of the deposition.

This type of in-process monitoring for in-situ metrology evolves to process real-time data to influence an on-the-fly response in the manufacturing strategy [118]. Additionally, cloud data storage provides a technological advantage to manage the information and to allow collaborators to process the information right away after the experiment regardless of their location. Tables 5.1 to 5.8 provide an overall view of the in-situ measurements in AM and more specifically, in direct energy deposition (DED) technology. The review presented herein includes the authors, the type of DED technology, and a classification of the in-situ sensing parameters during deposition for the temperature, distortion, bead geometry, and other measurements.

Table 5.1: Literature review for in-situ sensing of DED systems

Reference	DED Technology	Temperature	Distortion	Bead height	Bead width	Other
[127]	LENS	-Type C thermocouples FLIR Pris DS camera -12 bits digital camera with telephoto lens and 650 nm broad band filter	-	-	-	-
[121]	SDM	-	-High temperature biaxial strain gage	-	-	-
[128]	PAW-GMAW	-Infrared pyrometry camera (unspecified)	-	-Laser stripe 3D digitizer sensor CCD camera through narrow bandpass filter		-
[129]	LBAM	-Coaxial infrared high frame-rate CCD camera	-	-	-	**Powder delivery** -Optoelectronic sensor (unspecified)
[130]	LENS	-ThermaViz CCD based pyrometer	-	-	-	-

Table 5.2: Literature review for in-situ sensing of DED systems continuation

Reference	DED Technology	Temperature	Distortion	Bead height	Bead width	Other
[131]	LRF	-Two-color infrared thermometer	-	-	-	-
[132]	LMD	Pyrometers -Impac IGAR 12-LO MB 22 -Impac IGA 50-LO MB 13.5 plus	-	-	-CCD Camera (unspecified)	-
[133]	RLMwD	-	-	-Camera (unspecified) -Laser diode (unspecified)	-Camera (unspecified)	-
[134]	LMD	-Mikron infrared pyrometer MI-GA 5-LO	-	-OMRON laser displacement Z4M-W100	-	-
[122]	MD	-Thermocouples (unspecified) -Pyrometer (unspecified)	-Optical measurement ARAMIS by GOM	-	-	-

Table 5.3: Literature review for in-situ sensing of DED systems continuation

Reference	DED Technology	Temperature	Distortion	Bead height	Bead width	Other
[135]	RLMwD	-	-	-Camera (unspecified) -Near UV Laser diode at 409 nm	-Camera (unspecified)	-
[136]	GMAW-P CMT	-FLIR A320 thermal video camera -Thermocouples	-	-	-	-
[137, 138, 139] [140, 141]	GMAW-AM	-	-	-CCD Camera with neural filter and narrow-band filter		-
[142]	LMD/DMD	-FLIR A615 thermal video camera with spectral range of 8-14 µm	-	-Height regulation sensor (unspecified)	-	**Energy** -Energy management sensor (unspecified)
[143, 144]	GMAW-AM	-	-	-Laser projector of 30 mW emmitting at 650 nm and CCD		-

Table 5.4: Literature review for in-situ sensing of DED systems continuation

Reference	DED Technology	Temperature	Distortion	Bead height	Bead width	Other
[145]	LMD	-Canon EOS 7D with calibrated color temperatures	-	-	-	-
[146]	LENS	-	-	-	-	**Laser spot** -Primes GmbH FocusMonitor system **Spectrum** -Spectometer fiber connected to an Ocean Optics HR4000 CG UV-NIR spectrometer
[147]	GMAW-WAAM	-	-	-3D Laser scanning system		-
[123]	LENS	-Omega GG-K-30 type K thermocouples	-Substrate deflection with LDS Keyence LK-031	-	-	-

Table 5.5: Literature review for in-situ sensing of DED systems continuation

Reference	DED Technology	Temperature	Distortion	Bead height	Bead width	Other
[148]	LENS	-Single wavelenght pyrometer Raytek GPSCFLW	-	-	-	**Laser spot** -Primes GmbH FocusMonitor system
[149]	LENS	-Two wavelength imaging pyrometer ThermaViz optical sensor	-	-	-	-
[150]	GTAW-WAAM	-Thermocouples (unspecified)	-	-	-	-
[151, 152]	LENS	-	-	-	-	**Spectrum** -Ocean optics HR2000+ UV-VIS-IR spectrometer **Emissions** -Basler Pilot piA640-210gm CCD camera with 430 nm band-pass filter

Table 5.6: Literature review for in-situ sensing of DED systems continuation

Reference	DED Technology	Temperature	Distortion	Bead height	Bead width	Other
[124, 125]	LENS	-Omega GG-K-30 type K thermocouples	-Substrate distortion Keyence LK-031 LDS	-	-	-
[153]	Precitec YC50	-K type thermocouples	-	-	-	**Heat transfer** -Convective heat transfer Senflex SF9902 single-element hot-film sensors
[154]	LENS	-	-	-3D Spatial laser profilometry (unspecified)		-
[155]	GT-WAAM	-Thermocouples (unspecified) -IR pyrometer (unspecified)	-	-	-	**Arc stability** -High speed camera (unspecified)
[156]	LMD-w	-	-	-Keyence laser scanner	-CMOS Camera with neutral density filters	-

Table 5.7: Literature review for in-situ sensing of DED systems continuation

Reference	DED Technology	Temperature	Distortion	Bead height	Bead width	Other
[46]	RB-WAAM	-	-	-META SLS-050 V1 sensor		-
[157]	LENS	-	-	-	-	**Mass flow rate** -Acoustic emission sensor
[158]	HiEV	-Pyrometer MicroEpsilon CTLM	-	-Laser Profilometer Keyence		**Wire feed speed** -Triton sensor (unspecified) **Current** -Triton sensor (unspecified) **Shield gas flow** -Triton sensor (unspecified) **Oxygen concentration** -PurgEye 500 sensor
[126]	GMAW-WAAM	-	-	-META SLS-050 line structured laser sensor		-
[159]	GMAW-AM	-	-	-Creaform Handy Scan700 3D laser scanner		-

Table 5.8: Literature review for in-situ sensing of DED systems continuation

Reference	DED Technology	Temperature	Distortion	Bead height	Bead width	Other
[160]	LMD GMAW-WAAM	-	-	-	-	**Porosity** -Phased array ultrasonic testing with an Imasonic 10Mhz probe
[161]	GTAW-WAAM	-	-	-Online surface measurement through voltage	-	-

Laser engineered net-shaping (LENS) technology is the predominant DED system. The most relevant process measurements are temperature, bead profile and distortion. Thermocouples are the more reliable sensing source to measure temperature because of their wide temperature range and quick response to temperature changes. Other methods to measure temperature, such as pyrometers, have been demonstrated to be suitable for in-situ monitoring. For temperature measurements through radiation, it is important to note that metals' emissivity is susceptible to the temperature and the presence of surface oxides; therefore, the implementation of two-wavelength pyrometers allows for temperature measurements independent of emissivity [120]. The use of high-temperature biaxial strain gauge is described by Klingbeil et al. [121] to measure the distortion during the deposition process, although other authors such as Lundbäck and Lindgren [122], Heigel, Michaleris, and Reutzel [123], Denlinger et al. [124], and Corbin et al. [125] opted for optical measurements of these distortions in the substrate due to residual stresses developed during the AM process. The literature review showed that after temperature, the bead profile is the second most crucial in-situ measurement. Charged-coupled devices (CCD) aligned with the energy laser projection is a popular technique to detect the bead shape. Laser DED technology has the advantage of allocating cameras coaxial to the laser heat source; hence, a direct measurement of the melt pool is obtained. Recently, laser scanners have been used to measure bead height and width [126].

Other measurements, such as powder delivery through an optoelectronic sensor [129] or acoustic emissions [157] provide information to understand the feedstock's transportation phenomenon. Chabot et al. [160] present a novel way of measuring porosity with an ultrasonic probe. Other measurements include the use of spectrometers [146, 151, 152] to understand the optimal emissions towards a path for real-time flaw detection. The framework presented by Xu et al. [158] establishes foundations to build multi-sensor monitoring systems to improve the quality of AM parts.

The research presented herein develops a multi-domain platform for data acquisition in a plasma transferred arc additive manufacturing (PTA-AM) system. This chapter presents the research and development of the data collection and in-situ measuring strategies for the PTA-AM system described in section 4.3.2 from Chapter 4, which are developed with the objective of establishing geometric benchmarks to assess the performance, capabilities, and limitations of the sensing mechanisms. It also demonstrates the contribution of the data toward the prediction of the torch voltage and the stand-off-distance (SOD). The data contribute to the development of an in-situ embedded sensor for the bead geometry validated through single-track single-layer (STSL) and single-track multiple-layers (STML) experiments. It is important in the context of my research to determine deposition performance due to the mechanical requirements demanded by the heavy-duty industry for 3D printing components.

5.2   Materials and Methods

PTA-AM is a complex process supported by different structures as seen in Chapter 3. Each one of the structures provides insight into different front-ends such as the mechanical, electrical and computational. It is critical to gather reliable data to make decisions in AM systems and any other complex system. Data collection is used at the initial stages to understand the process from different points of view. By collecting as much information as possible, the PTA-AM process may be better interpreted, providing researchers with quantitative knowledge that can be processed to determine deposition performance.

Data processing in the latter stages of system development leads to monitoring techniques that measure performance. Knowledge of the system is essential when

the objective is to generate standardized data patterns that link data measurements with the operation. Moreover, awareness of the current state of the process supports better decisions, such as control strategies, during the manufacture. By comparing the actual measurement against a standard, feedback can be provided to the system to optimize a particular outcome. As DeMarco [162] states, "you can't control what you can't measure."

For instance, the structure concerning the positioning device is mainly involved in the spatial domain of the process. Here, positioning instructions are commanded by the software and executed by the FPGA board. The movement data are monitored and recorded by the integration software, which can provide the spatial information of the deposition process. For the sensor monitoring data collection in the PTA-AM system, five different domains were established: time domain ($\underline{\mathbf{t_i}}$), spatial domain ($\underline{\mathbf{s_j}}$), electrical domain ($\underline{\mathbf{e_k}}$), thermal domain ($\underline{\mathbf{h_l}} \otimes \underline{\mathbf{h_m}}$), and geometrical domain ($\underline{\mathbf{g_n}}$). The following subsections in this chapter provide information regarding the collection, handling, and analysis of the data obtained including its capabilities and limitations.

5.2.1 Time domain

Data collection in the experiments implemented in this chapter is linked to a timestamp. Due to constraints in the conditions of the signal acquisition devices, such as the communication protocols and the multitasking execution in a non-real-time target, the timestamp is variable and task-based dependant. Therefore, the time domain provides enough information regarding the time at which the data are acquired. The domain is described by the basis $\left\{\underline{\mathbf{t_i}}\right\}_{i=1}^{f}$ where f is the number of data points obtained in a particular experiment. The vector is described in Equation (5.1):

$$\underline{\boldsymbol{\tau}} = \tau_i \underline{\mathbf{t_i}} \qquad (5.1)$$

The timestamp is collected in milliseconds (ms), at a resolution of 1 ms with an uncertainty of ± 0.475 ms, which corresponds to a 95% confident interval.

5.2.2 Spatial domain

As previously stated, the positioning device is controlled by an FPGA board named Kflop. The current setup of the equipment is open-loop, although the controller can receive feedback from encoders. The responses in the x and y directions are subject to their respective stepper motor and lead screw. The stepper motor has a resolution of 1.8° per count, with an uncertainty of ± 0.05° per count. The resolution in the lead screw is 25 mm/rev, with an uncertainty of ± 0.0007 mm/rev. Each axis has a resolution of 125 μm per stepper count with an uncertainty of ± 3 μm. Additionally, the z-axis characteristics are accounted for by the information of its respective mechanism. Therefore, the resolution in the z-axis direction is 12.5 μm per stepper count with an uncertainty of ± 0.1 μm.

A Mitutoyo indicator dial is mounted on the PTA torch to calibrate the building plate [Fig. 5.1]. The dial has a resolution of 1 thou (a thousandth of an inch) with an uncertainty of ± 0.5 thou. The dial is located in contact with the building platform, and the indicator is set to zero. Then, through continuous movements of the positioning device, the platform moves, and the dial measures different points on the top. The calibration process is intended to set the building platform in the range of ± 10 thou. If any measurement is found to be out of range, pre-loaded springs at the base of the building platform can be adjusted to correct the alignment.

On the other hand, the calibration in the x-y plane is done by a two-step protocol. The first step is by selecting one axis at a time. An initial position is set and marked by lowering the plasma torch with a fine point pen attached to it [Fig. 5.2]. The torch is raised, and the final position is set and executed. The torch is lowered again to

Figure 5.1: Calibration of the z-axis. A gauge is used to test the level of the building plate.

mark the endpoint, and the calibration process is repeated in a new location to ensure repeatability. The obtained distances are then manually compared to the same set distance with a caliper. The second step is to repeat the protocol, moving two axes simultaneously with a 45° angle covering the same Euclidean distance as in the first protocol.

Although manual measurements agree with the calibration values, the amount of error attributable to human errors and measuring device uncertainty is low. An analysis of the position values given by the data collected in the controller can provide enough insight into the spatial domain. The orthogonal basis describes the spatial domain $\{\underline{s_j}\}_{j=1}^{3}$. Each orthogonal direction corresponds to the value of its x, y, and z axis position. The vector can be represented as:

$$\underline{\xi} = \xi_j \underline{s_j} \tag{5.2}$$

91
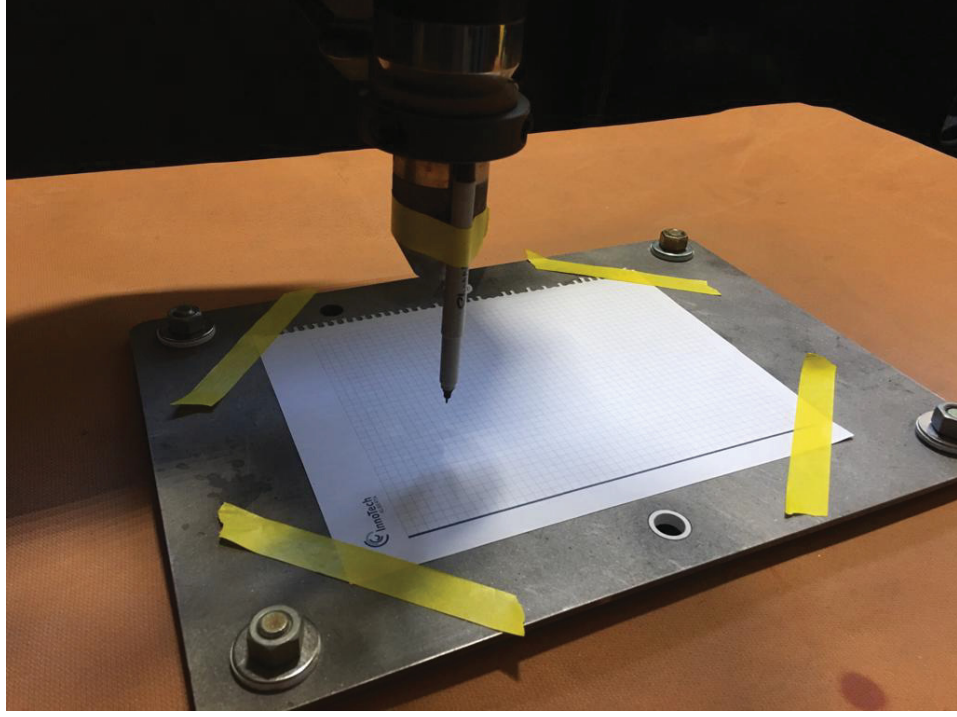
Figure 5.2: Calibration of the x and y axes. A linear movement is executed and the movement collected with the use of a pen and sheet to manually measure it as calibration input.

This vector shows a space location through different axes. The vector has to be expanded to its tensor form when coupled with the time domain to represent a full experiment acquisition. Equation 5.3 shows the coupling tensor.

$$\vec{\boldsymbol{\xi}} = \xi_{ij} \underline{\mathbf{t_i}} \otimes \underline{\mathbf{s_j}} \tag{5.3}$$

Consider $\vec{\boldsymbol{\xi}}^{(1)}$, $\vec{\boldsymbol{\xi}}^{(2)}$, $\vec{\boldsymbol{\xi}}^{(3)}$, $\vec{\boldsymbol{\xi}}^{(4)}$ to be four experiments with the same time domain $\underline{\boldsymbol{\tau}}$. All of these experiments have an initial position of 80 mm, a final position of 160 mm, and a speed of 600 mm/min. Figure 5.3 shows the data collected through the controller.

The spatial tensor needs to be transformed into the same time resolution to allow a comparison of the information. The transformation is a linear interpolation of the data at a particular standardized resolution. Appendix D provides the macro
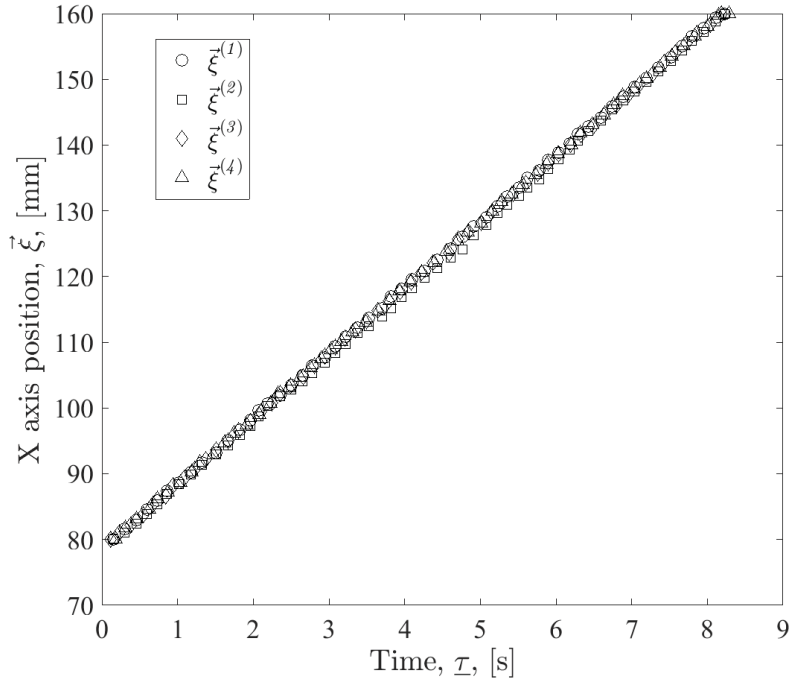
(a) Overall data
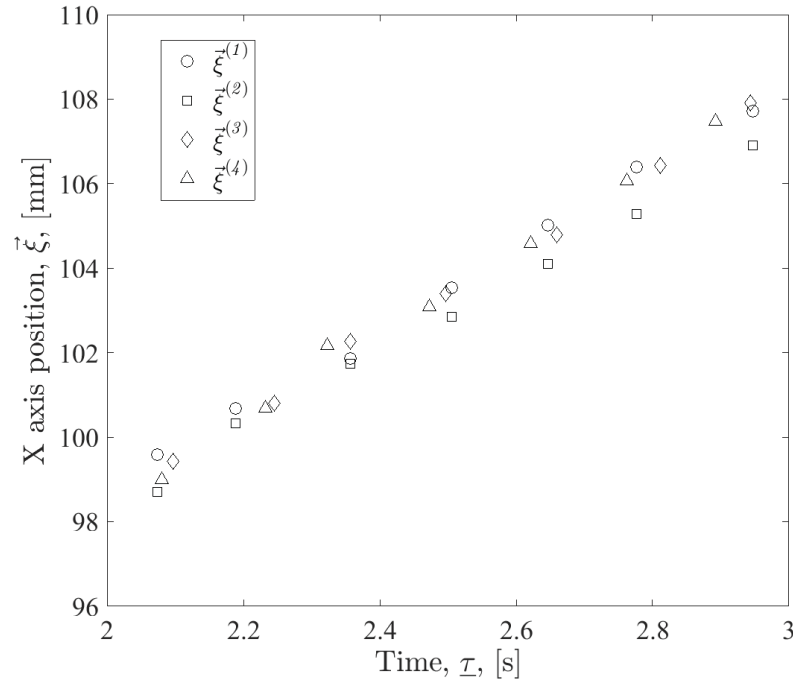
(b) Close-up to time 2 to 3 seconds

Figure 5.3: Positioning data of four experiments in the x-axis. Although ran separately, robustness of the data collection is shown.

for the implementation of the transformation. Later, the transformed tensors can be analyzed statistically to understand the uncertainty of the spatial domain. The transform operator is defined as:

$$\vec{\xi}* = \chi_s(\vec{\xi})^\Xi \tag{5.4}$$

indicating that the tensor will be spatially-scaled to the resolution proposed by the term Ξ. Figure 5.4a shows the spatial transformation of the experiment $\vec{\xi}^{(1)}$. Additionally, the Figure 5.4b shows the same data close-up as shown in Figure 5.3b but of transformed data with a spatial resolution of $\Xi = 0.125\ mm$.

Once the data are transformed, a point-wise statistical comparison between the data from of the experiments indicates that the average standard deviation is 0.374 mm [Fig. 5.5a]. An uncertainty of $\pm187\ \mu$m is calculated by using Equation 5.5 on the assumption that the bias is absent, and the measurements are mutually indepen-dent [163].

$$u = \frac{\sigma}{\sqrt{n}} \tag{5.5}$$

The term σ is the standard deviation and n the number of measurements.

Other spatial characteristics, such as the positioning device speed, are measured with the spatial domain. Consider the experiments $\vec{\xi}^{(5)}$, $\vec{\xi}^{(6)}$, $\vec{\xi}^{(7)}$, $\vec{\xi}^{(8)}$ to have speeds of 600, 1450, 2300, and 3150 mm/min, respectively. The starting point is at 0 mm, and the end location is at 80 mm. Figure 5.6a shows the data collected. The change in the slope corresponds to the increment in speed, reaching the end location faster. Similarly, but in the y-axis, the experiments $\vec{\xi}^{(9)}$, $\vec{\xi}^{(10)}$, $\vec{\xi}^{(11)}$, $\vec{\xi}^{(12)}$ are conducted with a starting point of 120 mm, a final location of 40 mm, and the speeds of 600, 1450, 2300, and 3150 mm/min, respectively [Fig. 5.6b].
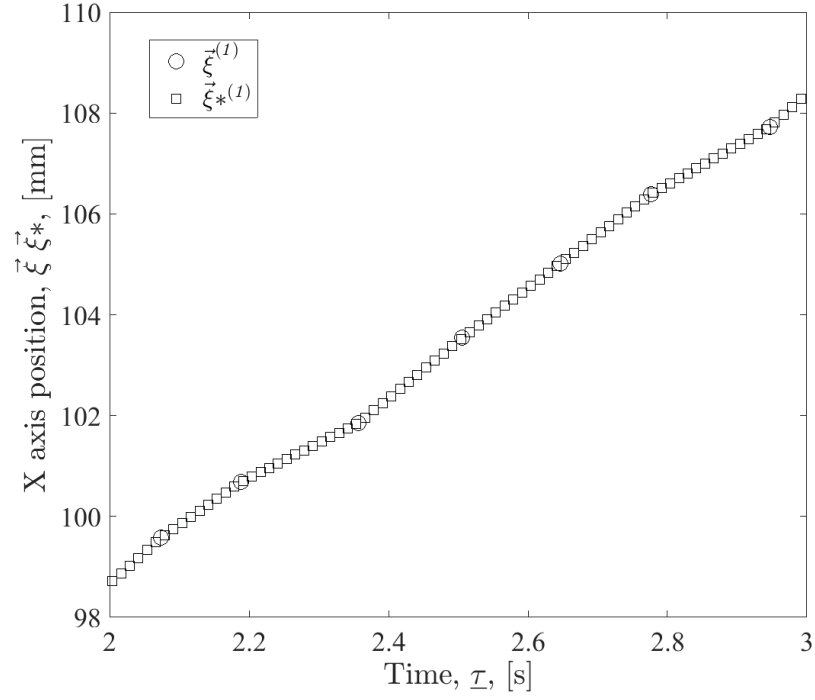
(a) Spatial transform of experiment $\vec{\boldsymbol{\xi}}^{(1)}$
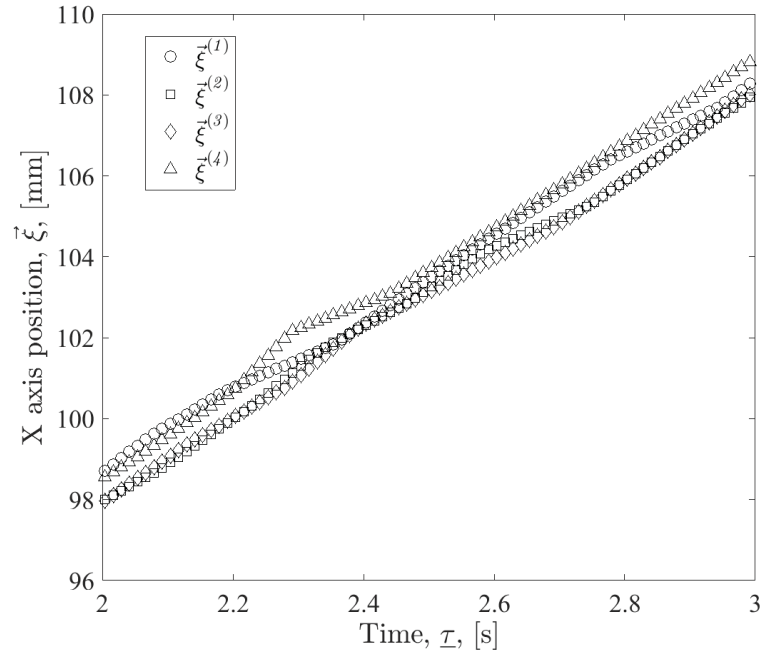
(b) Close-up of transformed data

Figure 5.4: Spatial transform operator. Data points are interpolated providing more resolution through the use of the operator.
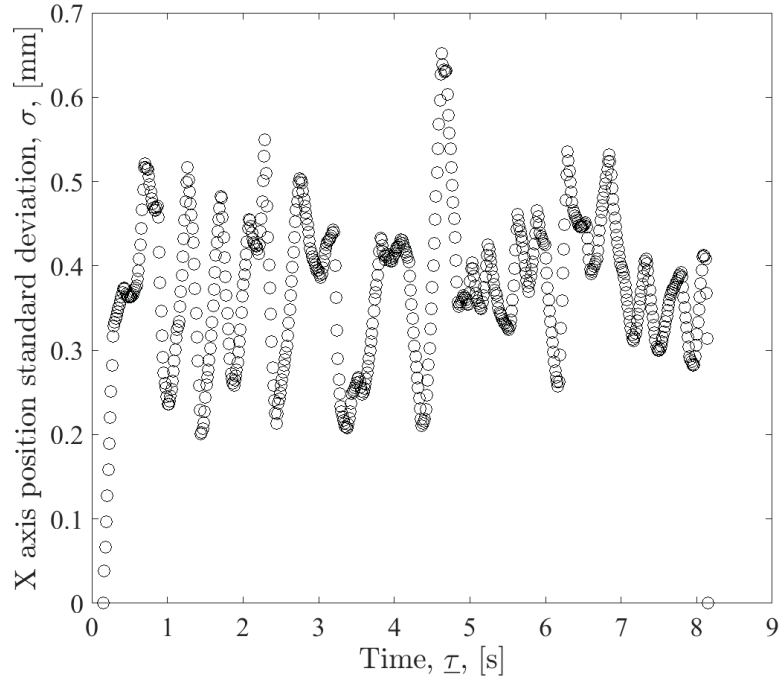
(a) Standard deviation in x-axis
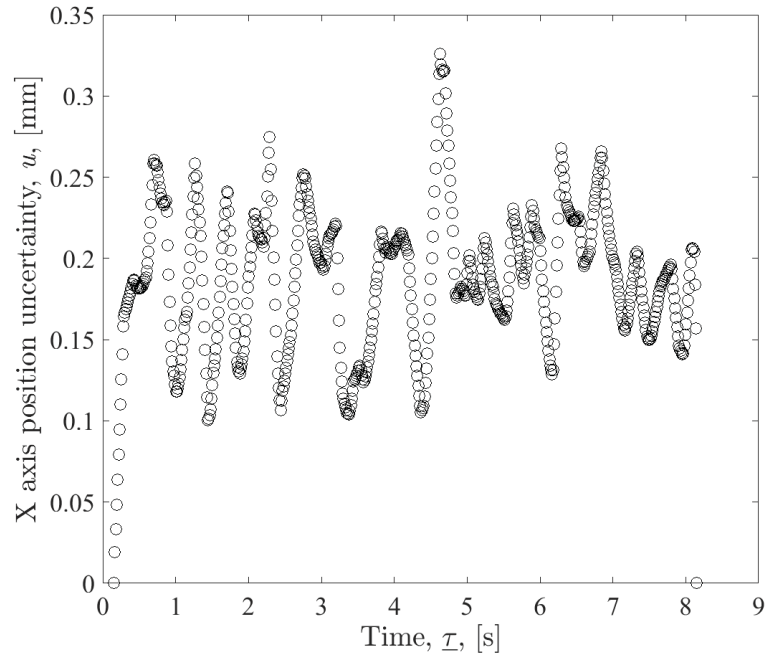
(b) Uncertainty in x-axis

Figure 5.5: Statistical analysis of x-axis positioning measurements. It is assumed that the bias is absent, and the measurements are mutually independent

(a) x-axis

(b) y-axis
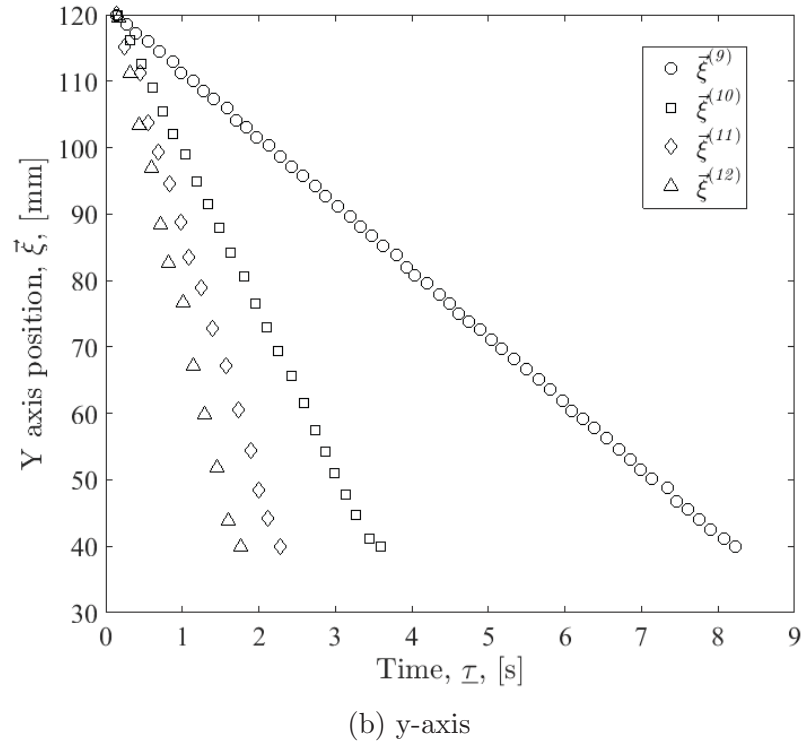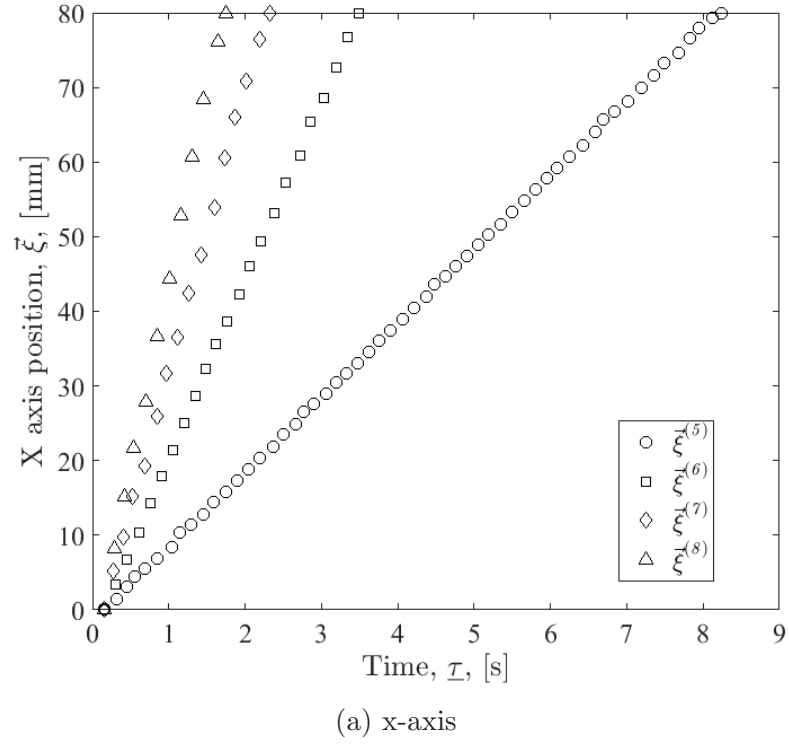
Figure 5.6: Positioning data at different speeds

5.2.3 Electrical domain

In the electrical domain, the current and the voltage of the PTA system are recorded. The current is measured through a current shunt connected in cascade to an amperage signal conditioner from the brand RED LION IAMA and an Omron analog input unit. The resolution of the signal conditioner is 40 mA, with an uncertainty of ±400 mA. For the analog unit, the resolution is 100 mA with an uncertainty of ±1.6 A. The combined current's resolution is 100 mA with an uncertainty of ±2.4 A. The voltage is measured with a current shunt connected to a RED LION IAMA voltage signal conditioner and an analog input unit from Omron. The resolution of the signal conditioner is 5 mV, with an uncertainty of ±50 mV. The analog unit has a resolution of 2.5 mV with an uncertainty of ±20 mV. Therefore, the voltage measurement has a resolution of 2.5 mV with a coupled uncertainty of ±150 mV.

The non-orthogonal basis describes the electrical domain as $\left\{\underline{\mathbf{e_k}}\right\}_{k=1}^{2}$. The lack of orthogonality is due to the relationship between voltage and current given by Ohm's law shown in Equation 5.6 [164].

$$V = RI \tag{5.6}$$

In this domain, the basis sub-sets correspond to the voltage and the current. The vector is represented by Equation 5.7:

$$\underline{\mathbf{\Phi}} = \Phi_k \underline{\mathbf{e_k}} \tag{5.7}$$

Similarly to the spatial domain, to represent the information in an experiment, the vector is expanded to its tensor form:

$$\vec{\mathbf{\Phi}} = \Phi_{ik} \underline{\mathbf{t_i}} \otimes \underline{\mathbf{e_k}} \tag{5.8}$$

The following transformation achieves a single sub-set, such as the voltage vector in the experiment:

$$
\begin{aligned}
\underline{\mathbf{V}} = \vec{\mathbf{\Phi}} \cdot \underline{\mathbf{e_1}} \\
= \Phi_{ik}\underline{\mathbf{t_i}} \otimes \underline{\mathbf{e_k}} \cdot \underline{\mathbf{e_1}} \\
= \Phi_{ik}\left(\underline{\mathbf{e_1}} \cdot \underline{\mathbf{e_k}}\right)\underline{\mathbf{t_i}} \\
= \Phi_{ik}\delta_{1k}\underline{\mathbf{t_i}} \\
= \Phi_{i1}\underline{\mathbf{t_i}}
\end{aligned}
\tag{5.9}
$$

The next transformation obtains the data for the current sub-set:

$$
\begin{aligned}
\underline{\mathbf{I}} = \vec{\mathbf{\Phi}} \cdot \underline{\mathbf{e_2}} \\
= \Phi_{ik}\underline{\mathbf{t_i}} \otimes \underline{\mathbf{e_k}} \cdot \underline{\mathbf{e_2}} \\
= \Phi_{ik}\left(\underline{\mathbf{e_2}} \cdot \underline{\mathbf{e_k}}\right)\underline{\mathbf{t_i}} \\
= \Phi_{ik}\delta_{2k}\underline{\mathbf{t_i}} \\
= \Phi_{i2}\underline{\mathbf{t_i}}
\end{aligned}
\tag{5.10}
$$

Figure 5.7 shows the voltage and the current information for the experiment $\vec{\mathbf{\Phi}}^{(1)}$. Although the voltage variations are produced due to different process parameters (see subsection 5.3.1), the current is typically held constant to a defined value for the experiment. In the example provided in Figure 5.7b, the current is setup at 25 A and a variation of -0.5 A is observed.
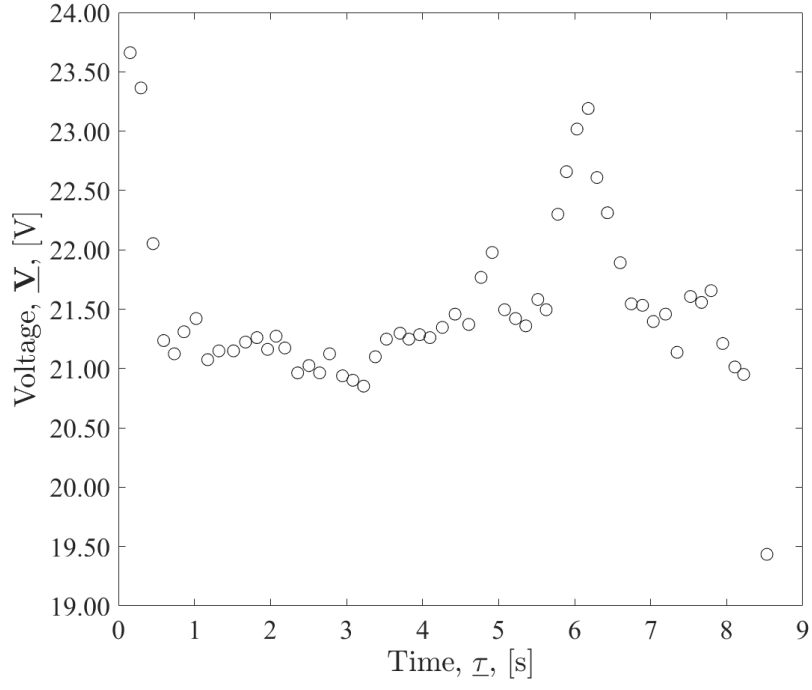
(a) Voltage
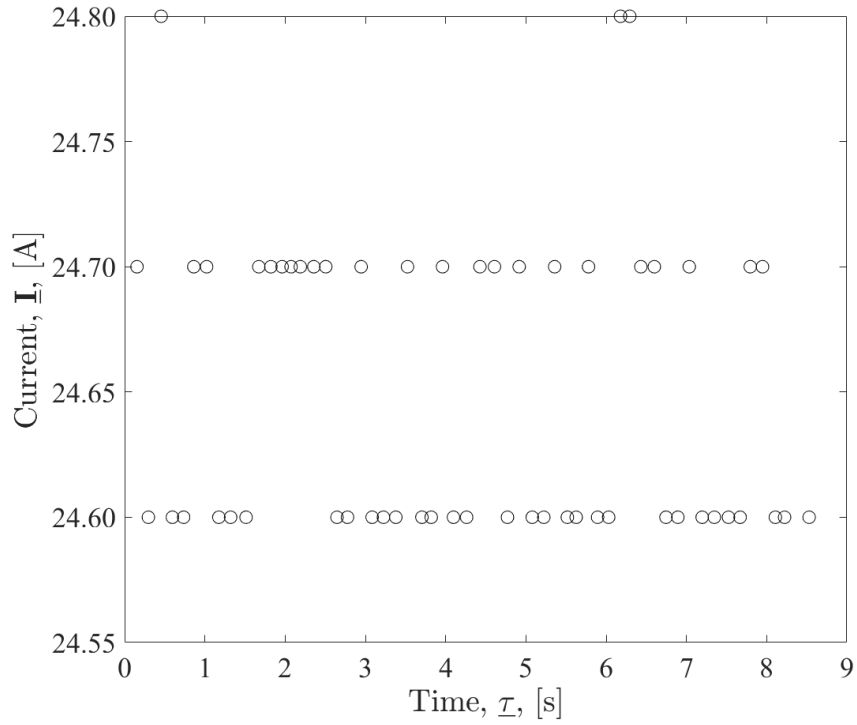
(b) Current

Figure 5.7: Data in the electrical domain for experiment $\vec{\mathbf{\Phi}}^{(1)}$

5.2.4 Thermal domain

Data acquisition for the thermal domain is achieved through a 16-point thermocouple array [Fig. 5.8]. The K-type thermocouples were mounted inside ceramic insulators and inserted in holes distributed through a 152.40 mm x 152.40 mm x 12.7 mm (6" x 6" x 1/2") hot-rolled flat bar made of ASTM A36 steel. The array is clamped between the substrate and the building plate. Since plasma generates intense heat capable of melting the thermocouples at direct contact, this method allows the recording of the temperature indirectly from under the substrate. These are unsheathed precision fine gauge thermocouples from the brand OMEGA with a measuring range from -270°C to 1260°C, a resolution of 0.1°C, and uncertainty of ±0.75%. The thermocouples are connected to an AD8495 precision thermocouple amplifier with a cold junction compensation. The cold junction is used as a reference to determine the actual temperature by compensating changes in temperature at the reference junction so that the output voltage is an accurate representation of the hot junction measurement. The amplification device has a resolution of 5 mV/°C and an uncertainty of ±2°C. For the range of temperatures in the thermocouples, the uncertainty of the amplifiers corresponds to ±0.13%. The output voltage from the amplifier is collected with the analog input module from a National Instruments sbRIO-9637 board. The resolution of the unit is 305μV and the uncertainty is ±0.042%. Accounting for the information supplied at every stage, the overall resolution of the thermal domain is calculated as 0.1°C with an uncertainty of ±0.922%.

The orthogonal bases $\left\{\underline{\mathbf{h_l}}, \underline{\mathbf{h_m}}\right\}_{l=1,m=1}^{4}$ depicts the thermal domain. The basis $\underline{\mathbf{h_l}}$ corresponds to the thermocouple's position in the row location. The basis $\underline{\mathbf{h_m}}$ is related to the column position. Moreover, the domain is expressed by the tensor shown in Equation 5.11:
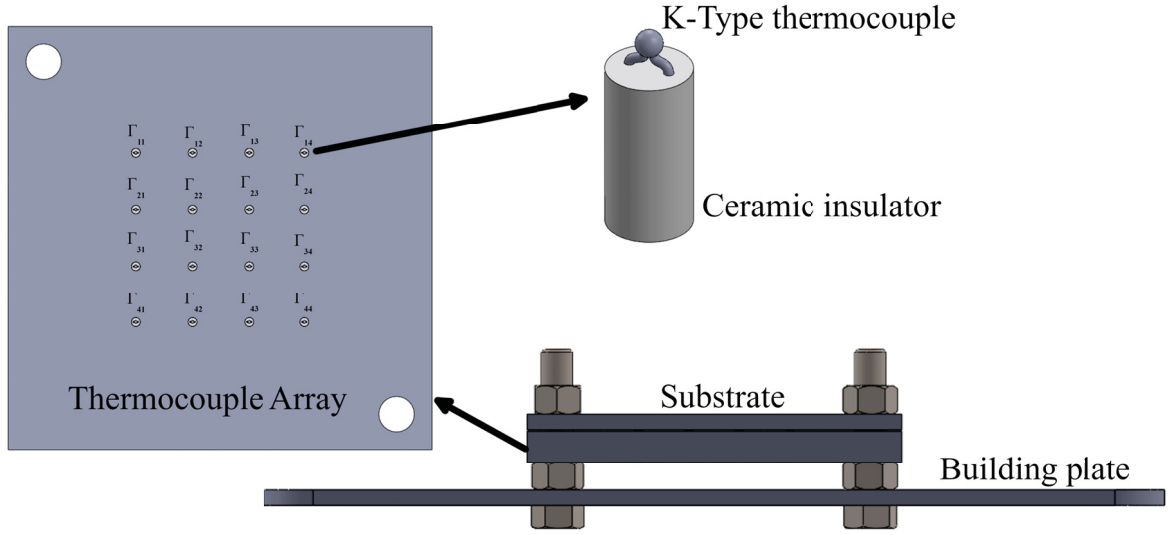
Figure 5.8: CAD model of the thermocouple array designed and developed for the thermal domain to collect the temperature under the substrate.

$$\vec{\Gamma} = \Gamma_{lm}\left(\underline{\mathbf{h_l}} \otimes \underline{\mathbf{h_m}}\right) \tag{5.11}$$

Similarly to other domains, the representation in an experiment is declared by expanding the tensor to its triad form:

$$\vec{\vec{\Gamma}} = \Gamma_{ilm}\left(\underline{\mathbf{t_i}} \otimes \underline{\mathbf{h_l}} \otimes \underline{\mathbf{h_m}}\right) \tag{5.12}$$

The triad has to be transformed to obtain the data of the experiment for a single thermocouple. Equation 5.13 shows the transformation to collect the thermocouple's data in the third row and the second column:

$$\vec{\mathbf{\Gamma_{32}}} = \underline{\mathbf{h_3}} \cdot \vec{\overline{\Gamma}} \underline{\mathbf{h_2}} = \underline{\mathbf{h_3}} \cdot \Gamma_{ilm}\left(\underline{\mathbf{t_i}} \otimes \underline{\mathbf{h_l}} \otimes \underline{\mathbf{h_m}}\right)\underline{\mathbf{h_2}}$$

$$= \underline{\mathbf{h_3}} \cdot \Gamma_{ilm}\left(\underline{\mathbf{h_2}} \cdot \underline{\mathbf{h_m}}\right)\left(\underline{\mathbf{t_i}} \otimes \underline{\mathbf{h_l}}\right)$$

$$= \underline{\mathbf{h_3}} \cdot \Gamma_{ilm}\delta_{2m}\left(\underline{\mathbf{t_i}} \otimes \underline{\mathbf{h_l}}\right)$$

$$= \underline{\mathbf{h_3}} \cdot \Gamma_{il2}\left(\underline{\mathbf{t_i}} \otimes \underline{\mathbf{h_l}}\right)$$

$$= \Gamma_{il2}\left(\underline{\mathbf{t_i}} \otimes \underline{\mathbf{h_l}}\right) \cdot \underline{\mathbf{h_3}}$$

$$= \Gamma_{il2}\left(\underline{\mathbf{h_3}} \cdot \underline{\mathbf{h_l}}\right)\underline{\mathbf{t_i}}$$

$$= \Gamma_{il2}\delta_{3l}\underline{\mathbf{t_i}}$$

$$= \Gamma_{i32}\underline{\mathbf{t_i}}$$

(5.13)

Individual measurement of the thermal domain is shown in Figure 5.9. The data present the information for the thermocouple in the second row and the second column in the thermocouple array.
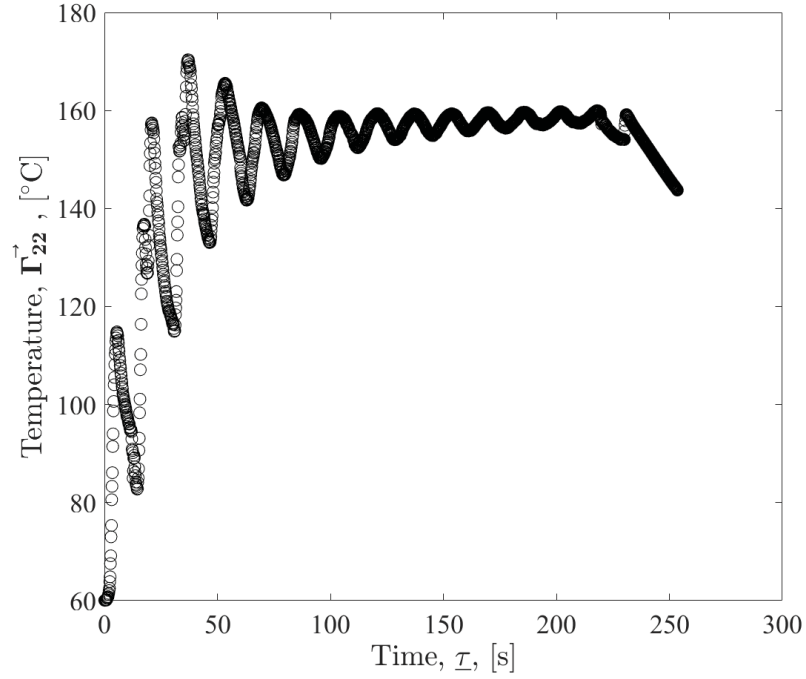
Figure 5.9: Thermocouple measurements of the second row and second column in the thermocouple array for a single-track multiple-layers experiment.

The experiment is a single-track multiple-layer experiment in which the thermal cycle through the process is evident by the oscillations of the heat generated by the plasma torch going back and forward. The data demonstrates the tendency of thermal equilibrium in the experiment.

Figure 5.10 exhibits the spatial representation of the thermocouple array data. The information is presented at nine different points in time. The figure demonstrates the heat displacement and heat accumulation during that time interval.

(a) t=1.388 sec   (b) t=2.853 sec   (c) t=4.259 sec

(d) t=5.714 sec   (e) t=7.177 sec   (f) t=8.685 sec

(g) t=10.151 sec   (h) t=11.563 sec   (i) t=13.023 sec
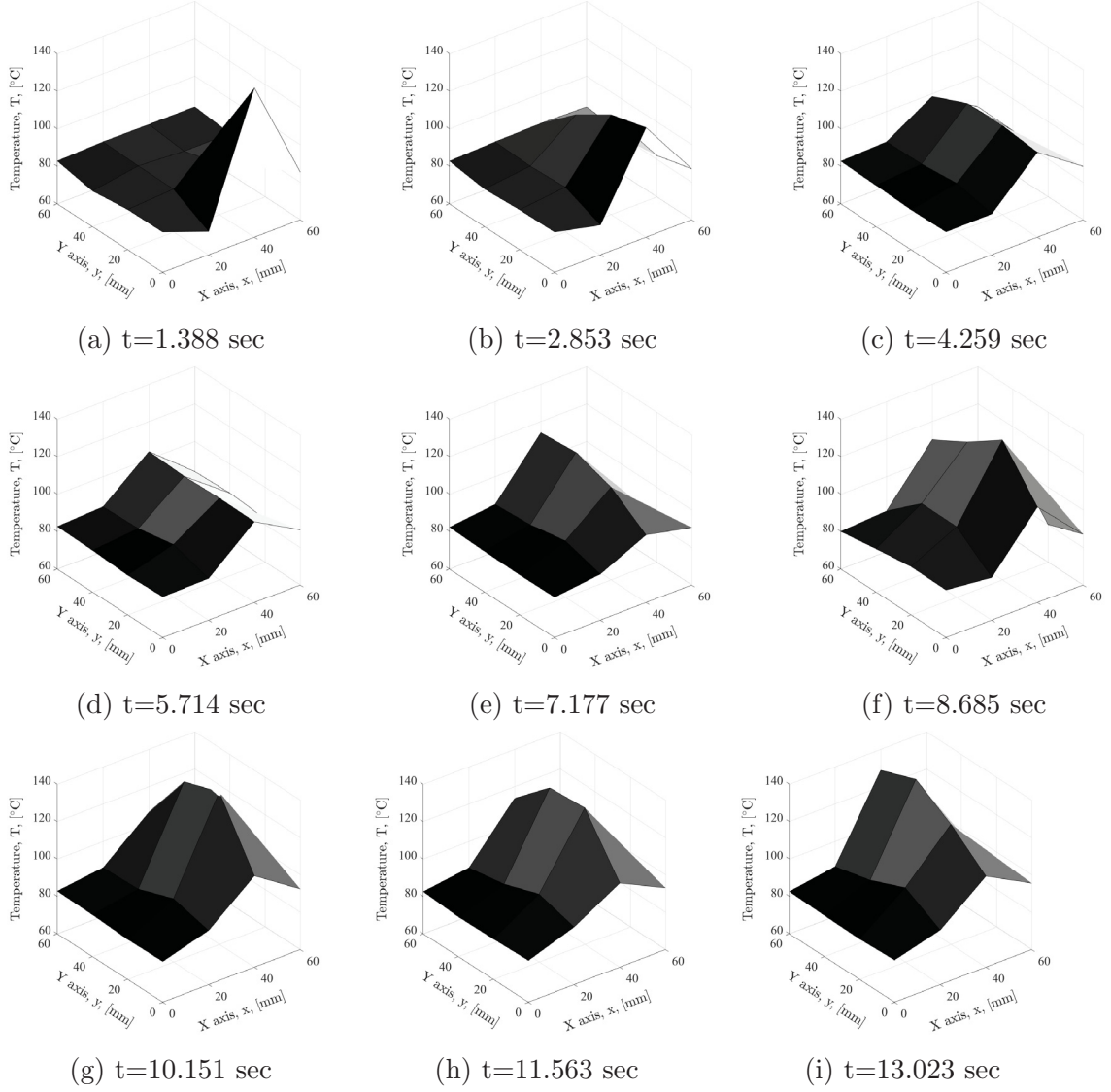
Figure 5.10: Data in the thermocouple array $\vec{\Gamma}$ at different times

5.2.5 Geometrical domain

The geometrical domain data are gathered through a laser profilometer from the company Sick Sensor Intelligence. The sensor is mounted near the PTA torch and calibrated to acquire the bead width and height [Fig. 5.11]. The sensor has a resolution in the x-axis of 25 μm with an uncertainty of ± 270 μm. In the z-axis, the resolution is 2 μm with an uncertainty of ± 50 μm.
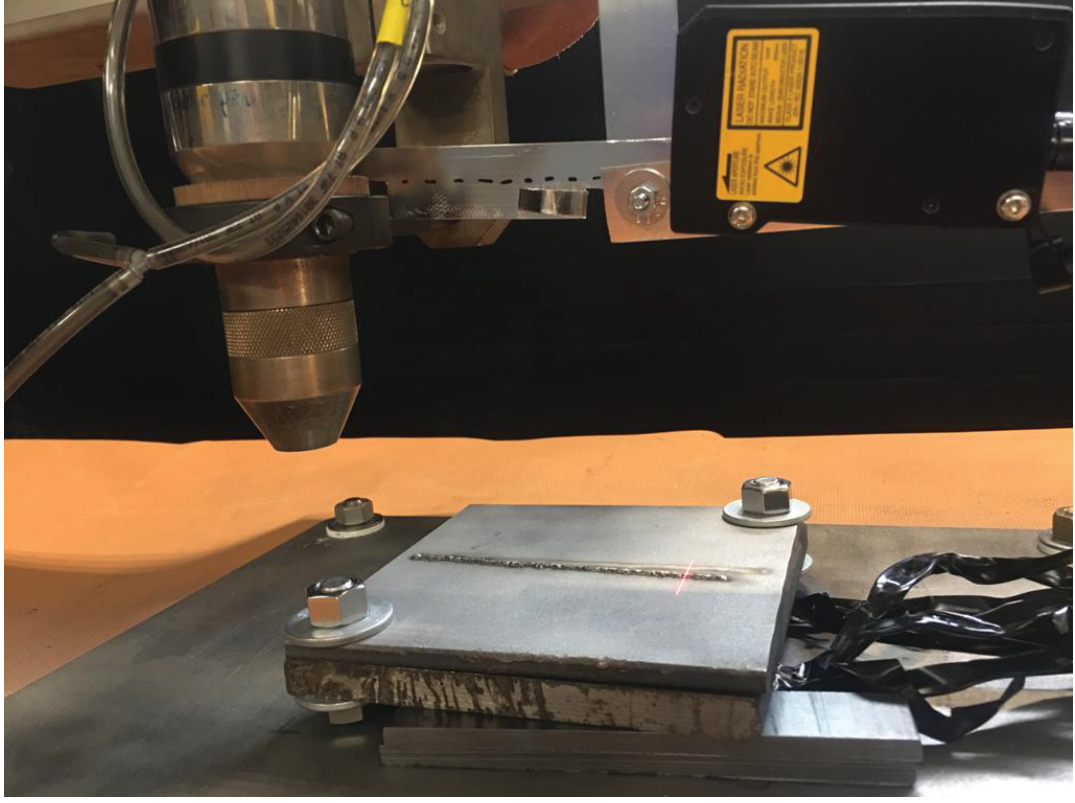
Figure 5.11: Laser profilometer mounted in the PTA-AM system.

The orthogonal basis $\left\{\underline{\mathbf{g_n}}\right\}_{n=1}^{2}$ describes the geometrical domain. The base $\underline{\mathbf{g_1}}$ corresponds to the bead height, while the base $\underline{\mathbf{g_2}}$ is for the bead width. The vector in Equation 5.14 represents the geometrical domain:

$$\underline{\mathbf{\Lambda}} = \Lambda_n \underline{\mathbf{g_n}} \tag{5.14}$$

In an experiment, the vector is extended to its tensor form by:

$$\vec{\mathbf{\Lambda}} = \Lambda_{in} \left(\underline{\mathbf{t_i}} \otimes \underline{\mathbf{g_n}} \right) \tag{5.15}$$

Geometric benchmark test artifacts (GBTAs) were used to evaluate the capabilities and limitations of the geometrical domain. GBTAs predict and assess capabilities and uncertainties in the AM process [165]. Different artifacts were built with differ-

ent characteristics to analyze the robustness of the sensing capabilities in the laser profilometer. Four angle profiles with half-inch in thickness and 90° angle were water-jetted with the following results: steps in mm, ramps in mm, steps in inches, and ramps in inches [Fig. 5.12].
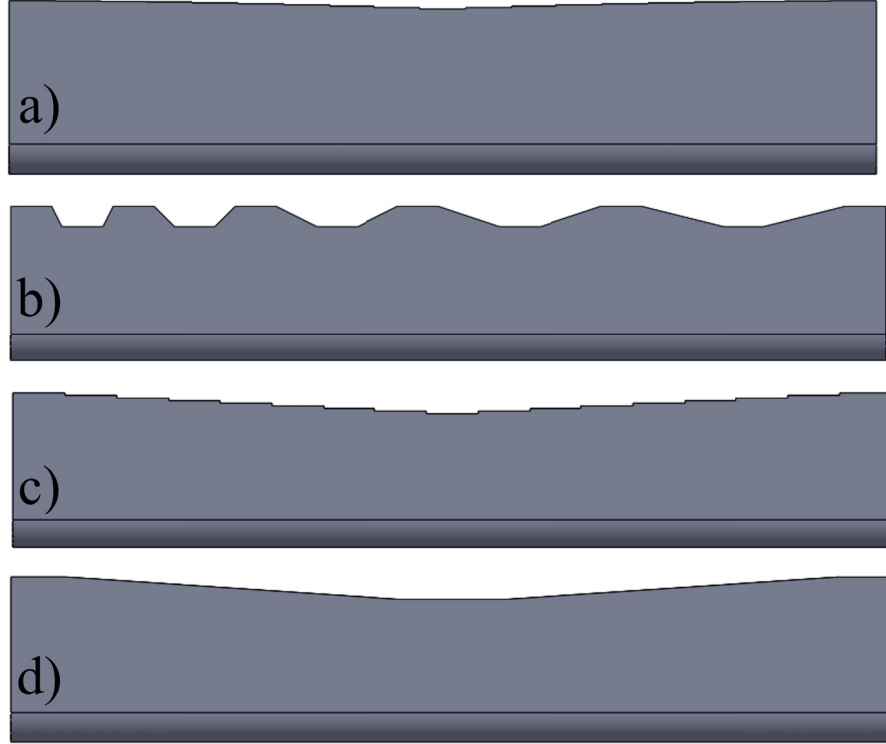
Figure 5.12: CAD of the calibration profiles, a) steps in mm, b) ramps in mm, c) steps in inches, and d) ramps in inches.

The customized GBTAs were checked with the use of a Mitutoyo Crysta-Plus M443 coordinated measuring machine (CMM) with a resolution of 0.5 μm [Fig. 5.13]. The as-built values were then updated in the CAD models. Finally, the GBTAs were measured using the sensing device described at the beginning of current section.

The GBTAs were mounted under the Sick laser profilometer to collect the profile information. Due to positioning constraints, only the first 300 mm of the GBTAs

107

Figure 5.13: Measuring of the as-built calibration profile with CMM.

were scanned. The data were then pre-processed to compensate for the sensor position considering a minimum stand-off-distance of 2.54 mm (0.1 in) at its closest location to the nozzle. Figure 5.14 shows a superposition of the data collected with the CMM and the laser profilometer. For each pair of the GBTA data information, an uncertainty analysis is performed.

For the steps in mm GBTA, the mean distance is 4.291 mm for the laser and 4.2544 mm for the CMM. The ranges are 3.92 mm and 3.9000 mm, and the standard deviations are 1.181 mm and 1.1928 mm. The uncertainty is 91 μm for both the laser profilometer and the CMM. Comparing both data, the Mean Squared Error (MSE) is 0.0067 mm^2 and the Root Mean Squared Deviation (RMSD) is 82 μm.
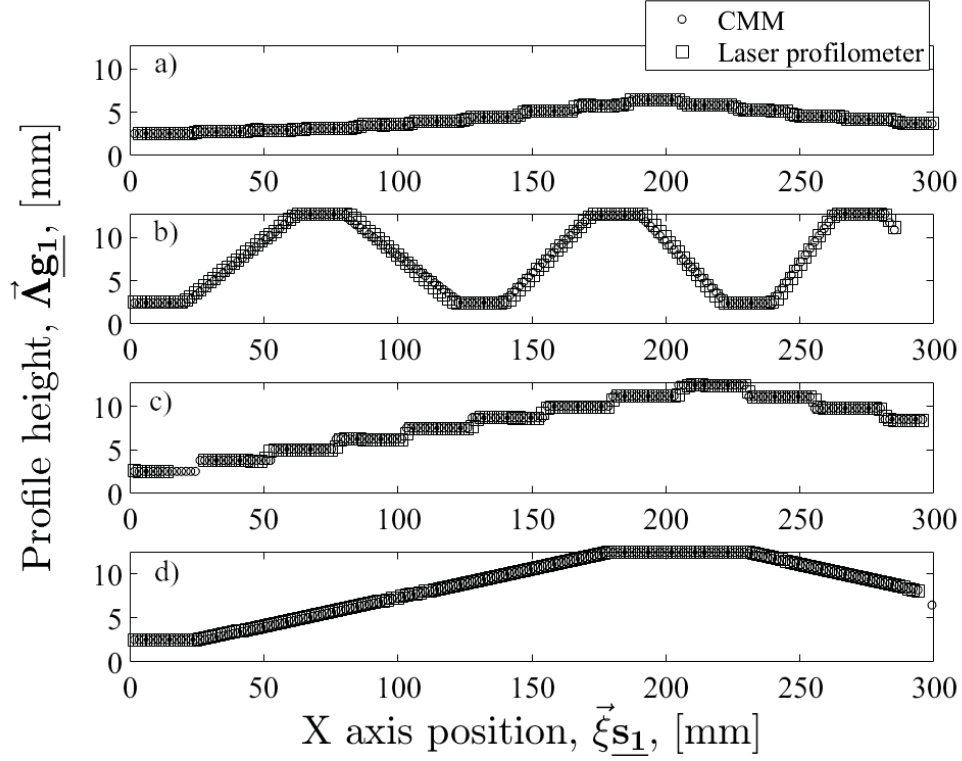
Figure 5.14: Geometrical domain data acquisition of the GBTAs compared to the CMM measurements a) Steps in mm, b) ramp in mm, c) step in inches, and d) ramp in inches.

Similarly, for the ramp in mm GBTA, the mean distance is 7.658 mm for the laser and 7.6562 mm for the CMM. The ranges are 10.308 mm and 10.3800 mm, and the standard deviations are 4.021 mm and 3.9453 mm. The uncertainty is 222 μm for the laser profilometer and 309 μm for the CMM. Comparing both data, the MSE is 0.0704 mm^2, and the RMSD is 265.3 μm.

In the case of the step in inches GBTA, the mean distance is 8.254 mm for the laser and 8.0665 mm for the CMM. The ranges are 9.908 mm and 9.9060 mm, and the standard deviations are 2.874 mm and 3.0343 mm. The uncertainty is 225 μm for the laser profilometer and 233 μm for the CMM. Comparing both data, the MSE is 0.0444 mm^2, and the RMSD is 210.7 μm.

For the ramp in inches GBTA, the mean distance is 8.552 mm for the laser and 8.5146 mm for the CMM. The ranges are 10.045 mm and 9.9060 mm, and the standard deviations are 3.431 mm and 3.4353 mm. The uncertainty is 265 μm for both the laser profilometer and the CMM. Comparing both data, the MSE is 0.0039 mm^2, and RMSD of 62.9 μm.

From the data comparison, it can be concluded that the sensor adopted for the geometrical domain can achieve a performance deviation between 63 and 266 μm compared to a CMM. These numbers validate that the sensor operates as an accurate in-situ measurement device.

Once the limitations of the geometrical domain sensor were calculated, a single-track single-layer (STSL) bead was considered as an example for data acquisition of the domain [Fig. 5.15]. The experiment consisted of a bead of 130 mm in length, and it was built using a current of 180 A. The positioning device speed was 1100 mm/min, and the powder quantity was 70 grams per minute.
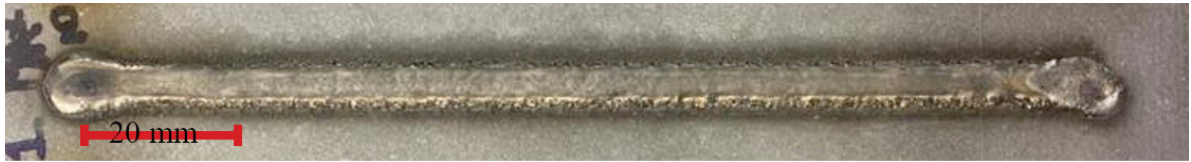
Figure 5.15: Single-Track Single-Layer bead.

The height in the geometrical domain $\vec{\Lambda}\underline{\mathbf{g_1}}$ is shown in Figure 5.16a. At the beginning and end of the graph, there are some transition zones. These zones correspond to the laser profilometer progressing from the substrate to the bead and backwards. Similarly, the information for the width in the geometrical domain is depicted in Figure 5.16b.

(a) Bead height   (b) Bead width
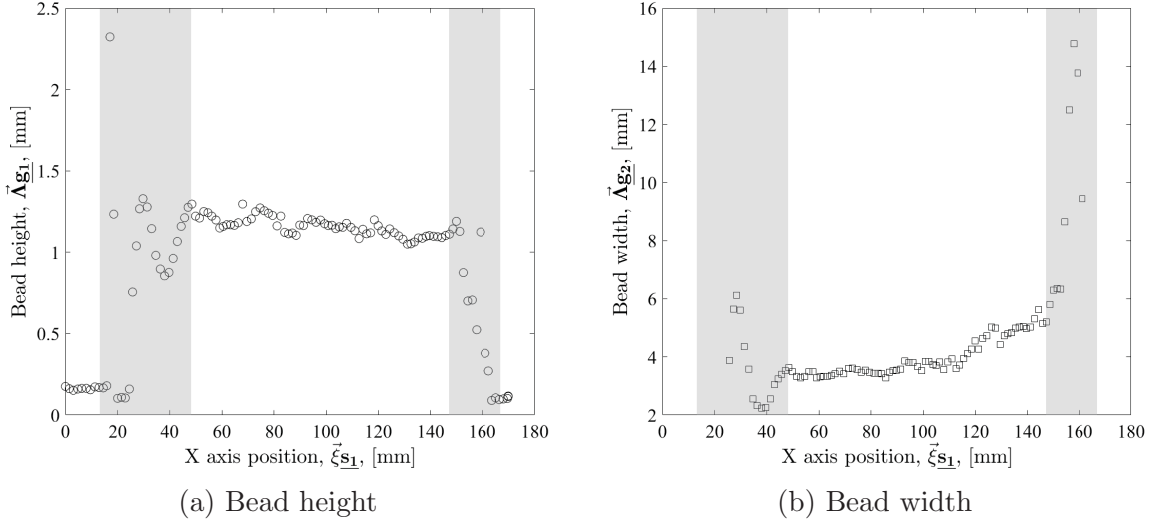
Figure 5.16: Geometrical domain data in $\vec{\mathbf{\Lambda}}$

5.2.6 Data monitoring and storage

The data collected from the experiments in the five domains is acquired and stored in a file in the following order: Timestamp, spatial domain, electrical domain, thermal domain, geometrical domain, and time domain. The data acquisition starts with the G-code instruction M115 invoked from the KmotionCNC software. Once the instruction is executed, the software integration in LabVIEW detects the command and launches the data collection. Figure 5.17 shows the WHILE loop that gets activated during the data acquisition with the stacked sequence structure showing its second frame.

From left to right, the process starts with the initialization of the variable labelled as Te, which accounts for the execution time. In the WHILE loop, a stacked sequence structure starts with three frames. The first frame initializes a second time variable called Ti with tick count in milliseconds. The second frame invokes the spatial, electrical, thermal, and geometrical measuring domains. Additionally, the variable number 40 stored in the Kflop is continuously monitored. In case of another execution of instruction M115, the data collection stops. Finally, the last frame reads a new tick

111
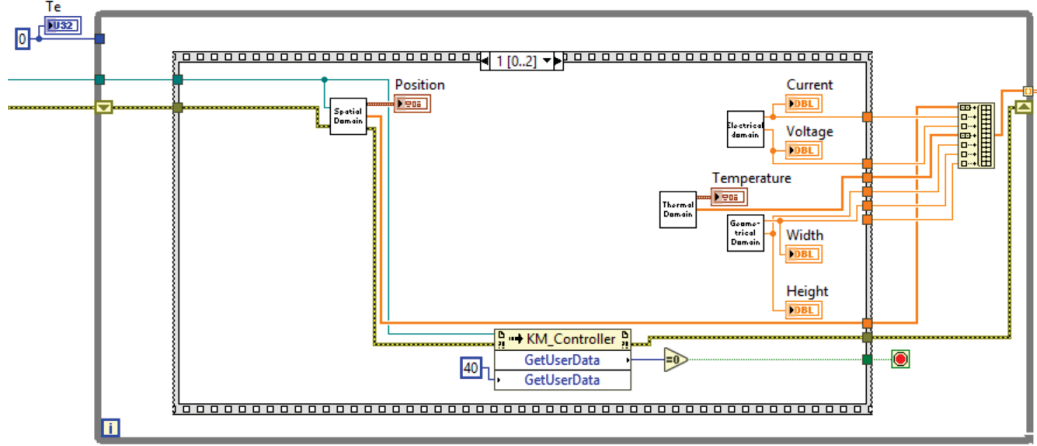
Figure 5.17: Active loop for the data acquisition in LabVIEW

count, which is compared with the one collected on frame one. The difference in counts represents the time that the data collection took for one sample rate. The time is added to the total acquisition time variable Te to record the overall execution time. This process is constantly repeated until the execution of another M115 instruction. A key feature is that because the integration software is running on a PC, the data acquisition is not time deterministic. Specialized equipment suitable for real-time applications is necessary to provide a time deterministic process for a standardized sample rate.

Figure 5.18 presents the process diagram for the data storage. Parallel to the data acquisition, the setup for paths and files in local and cloud storage is prepared.

After the experiment, the data are available, and the software automatically assigns the headers and timestamp. The information is locally stored on an SD card, and then a Google drive service reference is employed to upload the file to the cloud. Therefore, the data are immediately available for research purposes.
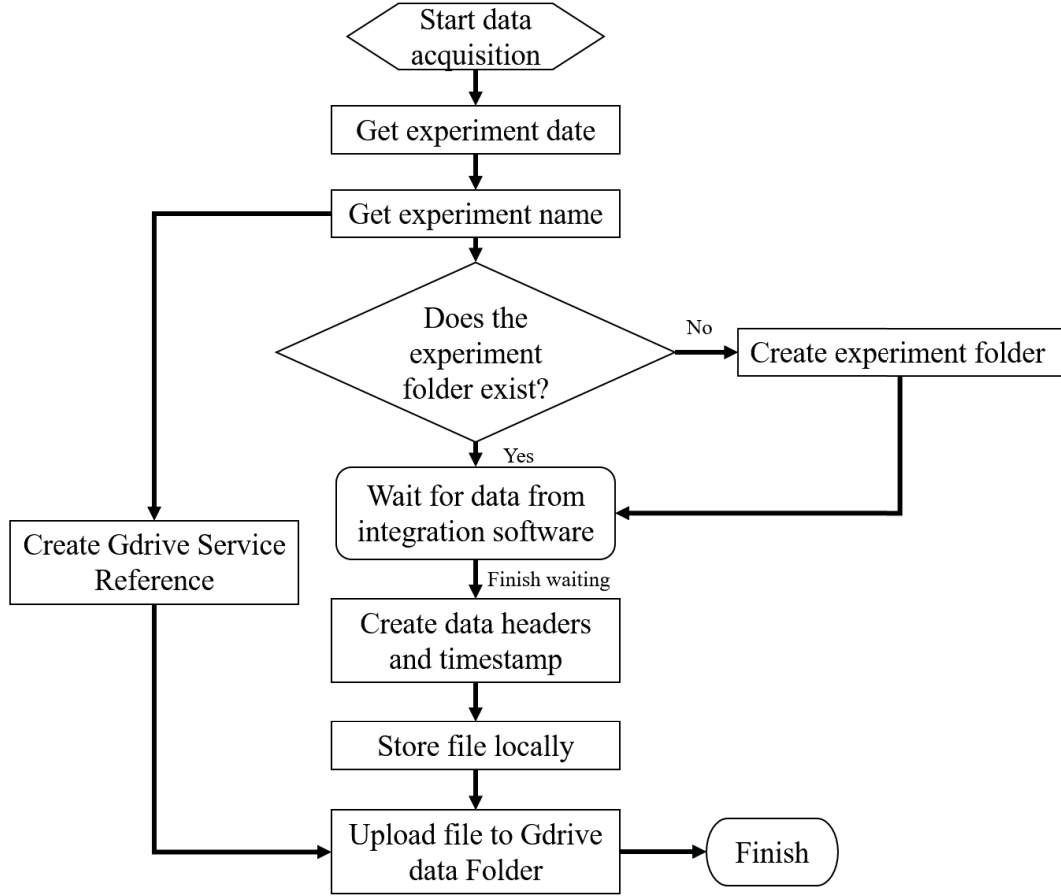
Figure 5.18: Process diagram for data storage

5.3 Results & discussion

The data collected in the different domains provide the first insight into the AM process for the PTA-AM system. The spatial, electrical, thermal, and geometrical data collected synchronously support the analysis to understand their relationship. This section presents some scenarios in which the data allowed a multi-variable analysis.

5.3.1 Voltage multiple regression

The information collected in the calibration experiments pointed to a straight connection between the voltage acquired and the process parameters. Equation 5.6, presented in the electrical domain section 5.2.3 of this chapter, describes the relationship between the current and the voltage with the use of Ohm's law. In the PTA-AM

system, the current is a process parameter that is controlled accurately as an input for the process. Moreover, the voltage depends on the resistance between the nozzle's tip and the substrate. Additionally, the resistance is a multi-variable parameter that depends on the following factors:

- Stand-off-distance (SOD)

- Resistivity of the material (M_ρ)

- Powder flow rate (P_f)

- Shielding gas flow rate (Sh_f)

- Shielding gas type (Sh_t)

- Center gas flow rate (C_f)

- Center gas type (C_t)

- Powder gas flow rate (Pg_f)

- Powder gas type (Pg_t)

- Nozzle angle (N_A)

- Nozzle diameter (N_d)

- Nozzle wear (N_w)

- Electrode setback (E_s)

- Electrode diameter (E_d)

- Electrode tip shape (E_t)

- Electrode wear (E_w)

- Electrode material (E_m)

Hence, the voltage in the torch is considered a function of these parameters. These parameters were quantitatively linked to the voltage through a linear regression in which 693 data points were used. As a first approach, the regression assumes that each parameter has a linear dependency on the voltage. Additionally, the interactions between dependant variables are minimal, so the variables' interactions are neglected. The following variables were assumed as constant in the analysis:

- M_ρ= 5.16 Ω·m

- Sh_t= 0 (argon)

- C_t= 0 (argon)

- Pg_t= 0 (argon)

- N_d= 3.175 mm [1/8 in]

- N_w= 0 (no wear)

- E_s= 4 mm

- E_d= 4.7625 mm [3/16 in]

- E_t= 20°

- E_w= 0 (no wear)

- E_m= 0 (tungsten)

The regression predicts the voltage based on the stand-off-distance (SOD), the powder flow rate (P_f), the shielding gas flow rate (Sh_f), the center gas flow rate (C_f), the powder gas flow rate (Pg_f), the nozzle angle (N_A), and the current (I). A regression equation was found $(F(7,693)=4808.6, p<.0000)$, with an R^2 of 0.9796. Equation 5.16

predicts the voltage between the nozzle tip and substrate based on these process parameters:

$$V = 28.77 + 0.78SOD + 0.04P_f - 0.66Sh_f$$
$$- 7.11C_f + 1.74Pg_f + 0.10I \quad (5.16)$$

The stand-off-distance is measured in millimetres, the powder flow rate in grams per minute, the shielding gas, center gas, and powder gas flow in standard litres per minute (slpm), the nozzle angle in degrees, and the current in amperes. The voltage increases by 0.78 volts for every mm of stand-off-distance, and it is raised 0.04 volts for each gram per minute of feedstock material. The voltage decreases by 0.66 volts for each standard litre per minute in the shield gas flow and by 7.11 volts for each slpm in the center gas flow. It rises by 1.74 volts for each slpm in powder gas flow and reduces by 0.001 volts for each degree in the nozzle angle. For each ampere, the voltage rises by 0.10 volts.

It is critical to predict the voltage through the process parameters planned for the experiments. To calculate the heat input, the energy provided by the torch is determined by the information in the electrical domain:

$$P = \eta \, V \, I \quad (5.17)$$

where η is the heat transfer efficiency, calculated for a plasma arc as 60% [166], V is the voltage of the process predicted through the multiple regression, and I is the current defined as an independent variable.

5.3.2 Bead height characteristics in depositions over GBTAs

The prediction of the voltage is the first phase towards understanding its relationship with the bead deposition. Although Equation 5.16 achieves some details describing the link of the voltage and the stand-off-distance, further information is needed to

measure the bead height accurately. Therefore, GBTAs were used to evaluate the bead height characteristics in depositions by using the data collected with the geometrical domain sensor.

Since the SOD plays a significant role in the deposition quality, two GBTAs were employed as substrate to deposit STSL beads to measure the bead height and bead quality in relation to the SOD [Fig. 5.19].
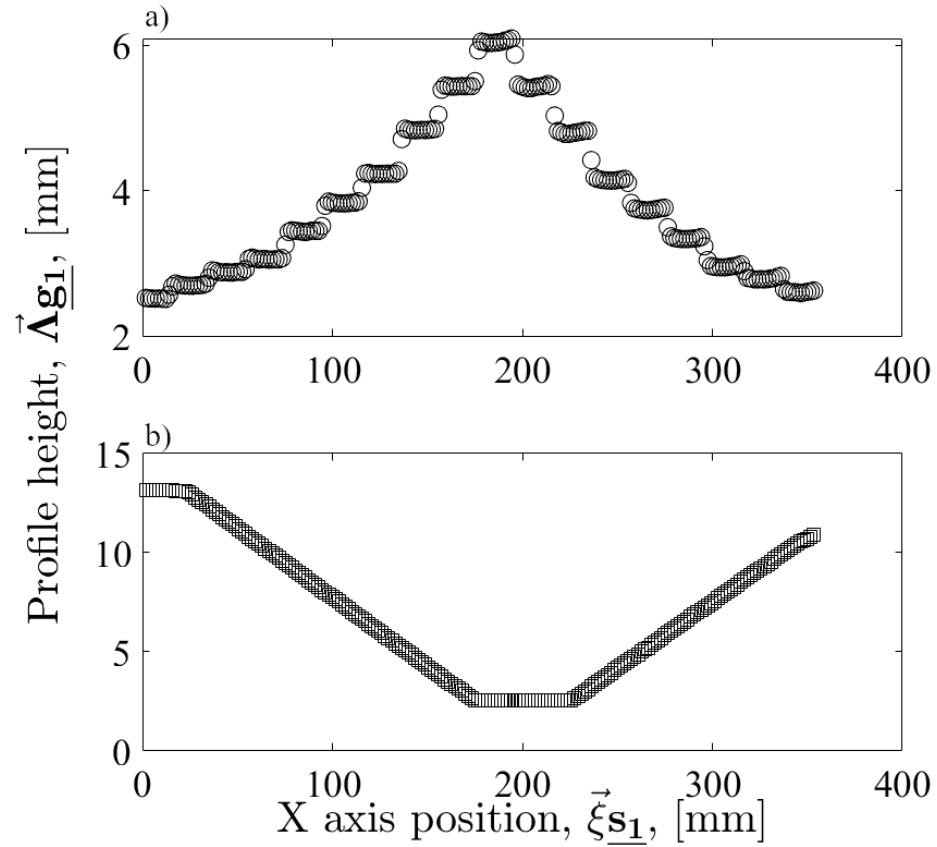
Figure 5.19: Geometrical domain data acquisition of the GBTAs used as substrate for bead height characterization a) steps in mm, and b) ramp in inches.

The GBTA described as a step in mm integrates a cascade of steps: three with a 200 μm increment, three with a 400 μm increment, and three with a 600 μm increment to reach the maximum SOD in the GBTA. The total range of the GBTA in the

z-axis is 3.58 mm, covering from a SOD of 2.54 mm to 6.09 mm. The other GBTA incorporates a ramp with a range in the z-axis of 10.63 mm with three stages: starting at 13.15 mm, lowering to 2.54 mm and returning to 10.89 mm. Due to positioning limitations of the laser sensor, a maximum displacement of 360 mm in the x-axis travel was considered.

For the deposition, the recommended process parameters obtained in Chapter 4, Section 7 were applied to deposit material on top of the GBTAs. The SOD between the nozzle and the artifacts is adapted to the minimum value for the PTA torch, which is 2.54 mm (0.1 inches). Because the nozzle tip's location remains constant during the movement in the x-axis direction, the travel over the GBTAs produces different ranges of SODs for the deposition.

Table 5.9 provides the process parameters values used to deposit an STSL deposition in the GBTAs. The powder and center gas are kept in 1.5 slpm, and the shielding gas in 10 slpm. The nozzle angle is rotated perpendicular to the deposition travel, which is 90 degrees from the x-axis direction. The powder flow rate is set to 40 grams per minute, the current to 50 A, and the positioning device speed to 500 mm/min.

Table 5.9: Process parameters for the deposition in the GBTAs

Powder gas (slpm)	Shielding gas (slpm)	Center gas (slpm)	Nozzle angle	Powder flow rate (gpm)	Current (A)	Table speed (mm/min)
1.5	10	1.5	90°	40	50	500

The deposition bead height was laser scanned and manually measured with scaled pictures incorporating the relationship between pixels and mm [Fig. 5.20]. The deposition is divided into sections 5 mm long. For each segment, the bead height is

measured at three discrete points. The resolution of the manual measurements is approximately 40 μm per pixel.
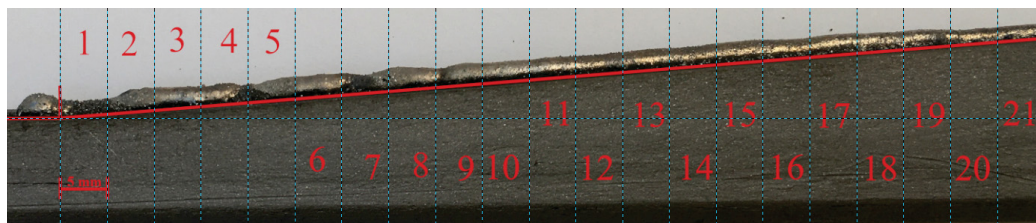
Figure 5.20: Deposition over ramp GBTA divided by sections of 5 mm.

The step GBTA starts with a SOD of 2.54 mm referenced to the nozzle. This distance does not allow the powder streams from the powder pores to strike simultaneously into the plasma. Hence, instead of a single bead, two low-quality beads are observed at the first steps [Fig. 5.21]. Each of those two beads corresponds to each of the powder pores in the torch. In the sixth step (4.14 mm of SOD), the two beads start merging into one. The metal powder flowing from the nozzle must melt at the intersection of the two streams to print a good bead.

Figure 5.21: Deposition over the step GBTA. The deposition in the initial steps is unstable due to short stand-off-distance.

After the bead merges, it starts to stabilize. In steps 6 and 7, the bead quality is low with some deviations due to the transition from two beads to one. During step eight (5.34 mm), the bead quality improves with less variance, which is when the bead deposition gets steady [Fig. 5.22].

Figure 5.23 demonstrates how the bead height changes over the steps in the GBTA. The bead height increases until the maximum SOD (6.09 mm), and then it decreases.

119
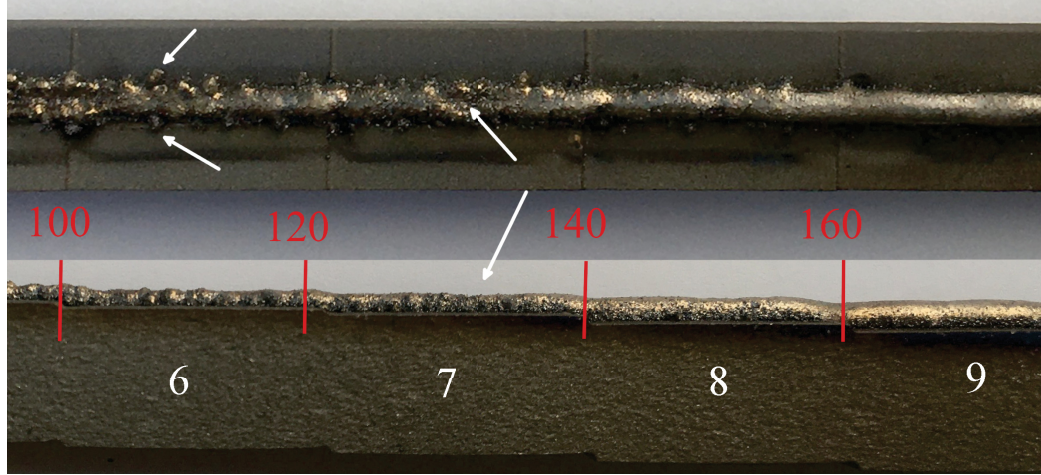
Figure 5.22: Deposition over the step GBTA. At a certain SOD, the deposition bead stabilizes.

The deviations in the deposition at the initial and final steps are a consequence of a small SOD that causes balling effect. Between steps 6 and 13, the bead is stable with fewer deviations. After step 14, the bead starts to separate again into two beads, and the variances increase.
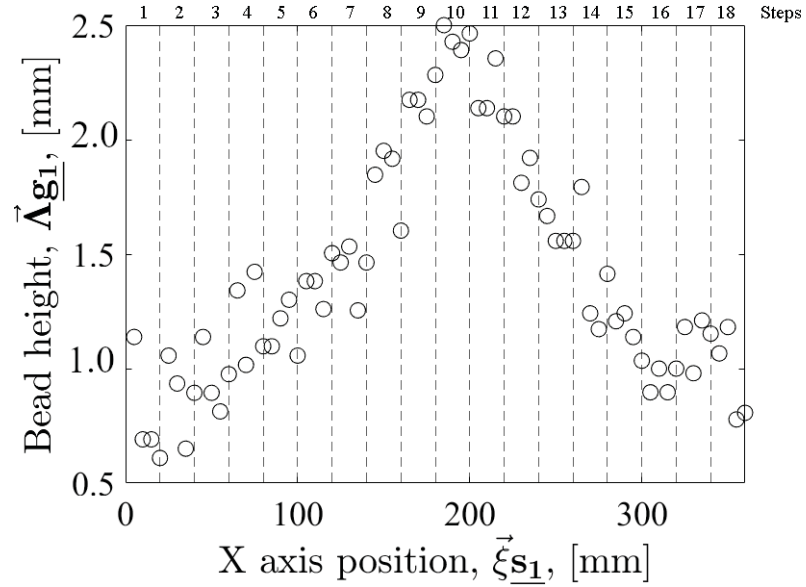
Figure 5.23: Bead height along the x-axis in the step GBTA. The balling effect on the initial and final steps shows more deviations.

It is concluded from the information in the step GBTA that to produce a continuous bead deposition, the SOD has to be above 4.14 mm. The maximum SOD depends on the system capability to generate a plasma transferred arc at higher distances. According to the supplier, the recommended maximum SOD is 12.7 mm (0.5 in). The next GBTA provides more information in the suggested operational SOD range.

The ramp GBTA starts at the maximum SOD. In the deposition, the bead starts with a continuous deposition, but with variances in the bead width. The bead stabilizes with fewer deviations once the deposition reaches the SOD of 9.75 mm at the x-axis position of 71.15 mm [Fig. 5.24]. When the SOD gets to 4.74 mm at the x-axis position of 143 mm, the bead starts to get unstable and split into two beads, producing a similar result to the phenomena described for the step GBTA. The GBTA is closest to the nozzle tip at the minimum SOD; a distance that hinders the deposition, causing a balling effect.
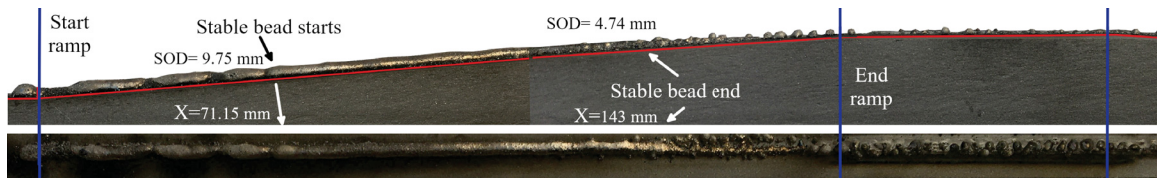
Figure 5.24: Deposition over the ramp GBTA. At the SOD range of 4.74-9.75 mm, the deposition bead is stable.

Figure 5.25 displays the bead height over the ramp GBTA. The bead height starts with a significant deviation at maximum SOD. As the SOD decreases, the variance likewise decreases to a point where the bead height starts falling happening at a stand-off-distance of approximately 8 mm. The bead height then plunges at the minimum SOD and increases as the SOD increases back.

121
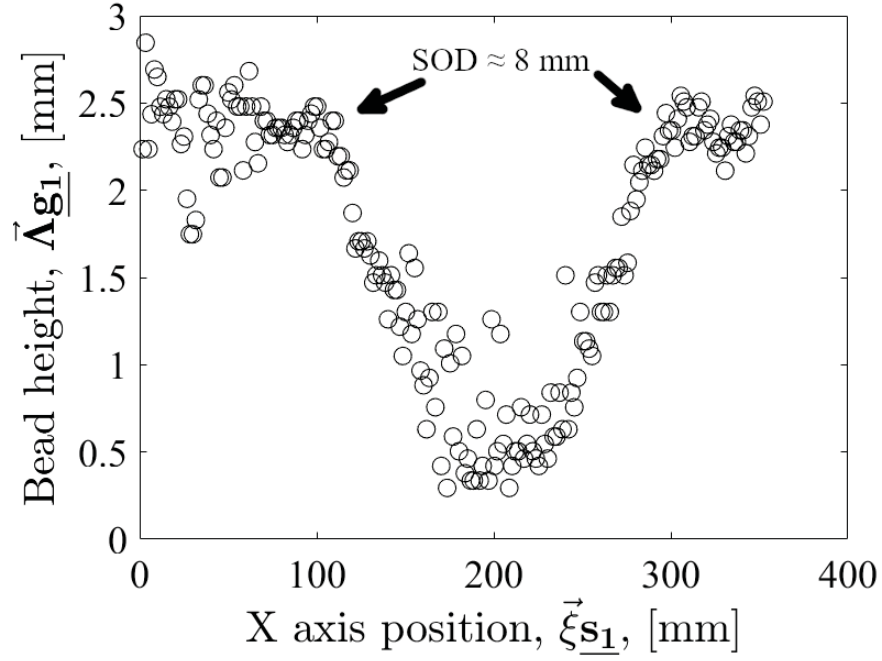
Figure 5.25: Deposition over the ramp GBTA. At the SOD of approximately 8 mm, the bead height is stable.

Similarly, the bead height is plotted against the different stand-off-distances achieved with the ramp GBTA [Figure 5.26]. On the low SOD, the bead height is smaller but with a significant dispersion. As the SOD increases, the bead height also increases and gets more stable. By around a stand-off-distance of 7 mm, the bead height is stable with a low variation. The bead height remains stable up to a SOD of 8.5 mm where the dispersion starts to increase. After this SOD, the bead height does not significantly improve, but it's dispersion increases. At the maximum SOD, as shown in the figure, there is a higher degree of instability in the bead height.
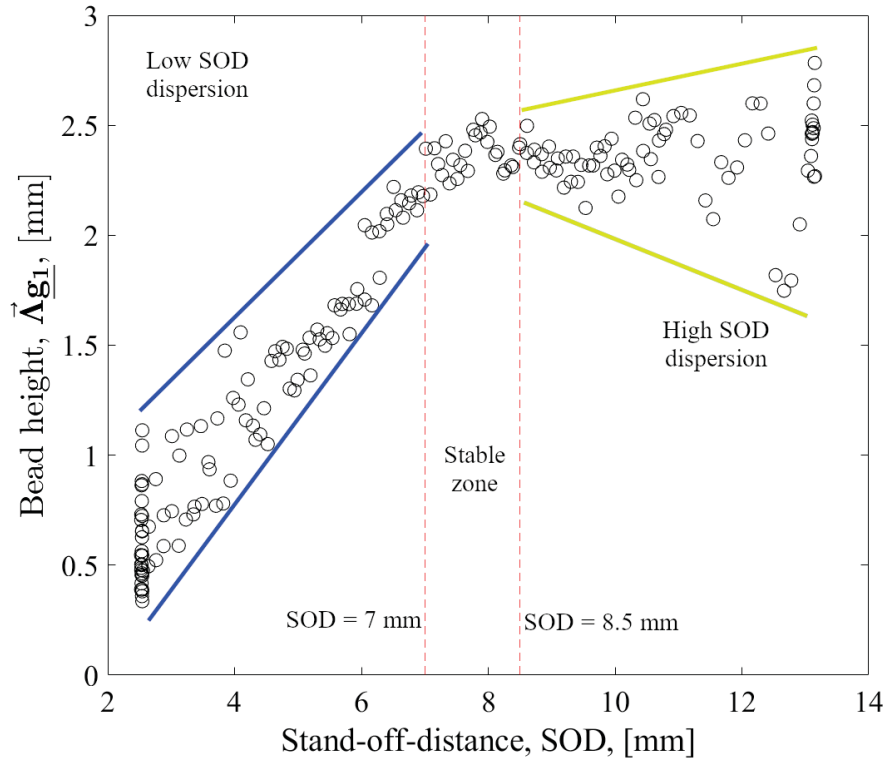
Figure 5.26: Bead height against stand-off-distance. There is a stable zone between 7 and 8.5 mm in which the variability of the bead height is minimized.
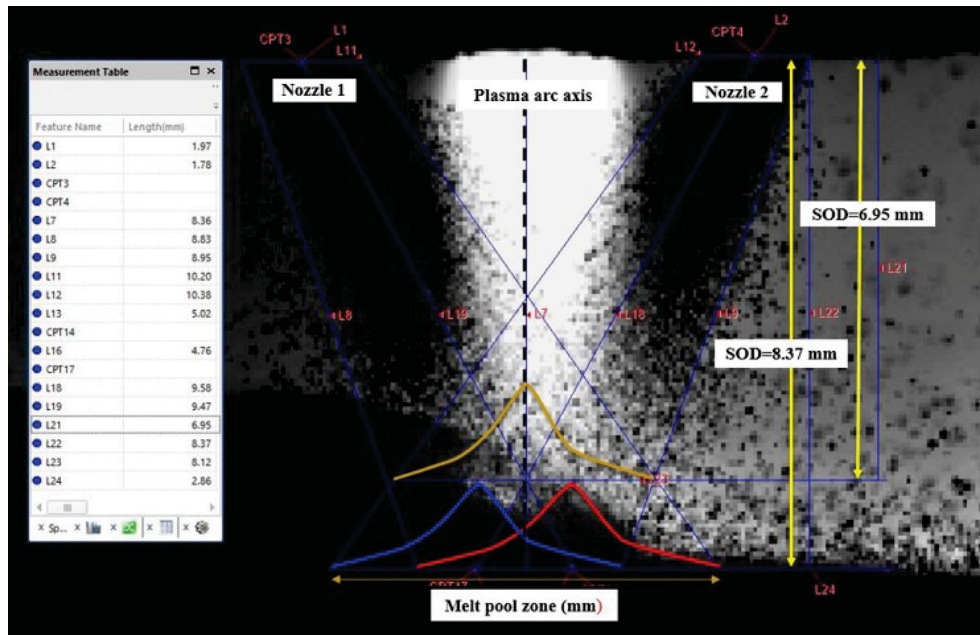
Figure 5.27: High-speed camera frame of the powder deposition. The powder Gaussian distribution is shown at 6.96 mm and 8.37 mm SODs.

The SOD result is validated by using a high-speed camera during the deposition process [Figure 5.27]. The plasma arc is at the center and the powder is delivered through the nozzles at the sides. By analyzing the particle trajectory of the powder, the powder Gaussian distribution is calculated. The analysis demonstrate that at a SOD of 6.95 mm the distribution of the intersection of both nozzles is maximized. At a higher SOD, the nozzles' distribution starts splitting generating a higher dispersion in the deposition, hence a higher variability in the bead height.

From both GBTAs, it is confirmed that for a continuous single bead deposition, the stand-off-distance has to be greater than 4.14 mm (0.16 inches). A SOD of 7 mm (0.27 in) provides a stable bead geometry, while distances greater than 8.5 mm (0.33 inches) induce instabilities in the deposition.

5.3.3 In-situ SOD measurement and bead height prediction using voltage data during autogenous energy deposition

Data in the electrical domain shows that the voltage reading is useful as an embedded sensors to implement in-situ measurements of the SOD. In this scenario, an autogenous energy deposition (AED) is applied to the top of the GBTAs used to evaluate the capabilities and limitations of the geometrical domain. The information collected in the AED experiments was used to correlate the SOD with the voltage recorded during the process.

The AED requires removing the powder-related process parameters for the experiments, allowing exclusively the heat transfer from the heat source to the substrate without metal powder deposition. Additionally, Equation 5.16 demonstrates the low contribution of the nozzle angle in the voltage, so this variable is neglected in the

analysis. Further simplification includes considering parameters such as shielding and center gases as constant. Therefore, the study consists of a SOD prediction based on in-situ measurements of the voltage and the current.

Analysis of the step GBTA in millimetres generates the following regression equation:

$$SOD_{Stepmm} = -45.02 + 0.02I + 2.53V \qquad (5.18)$$
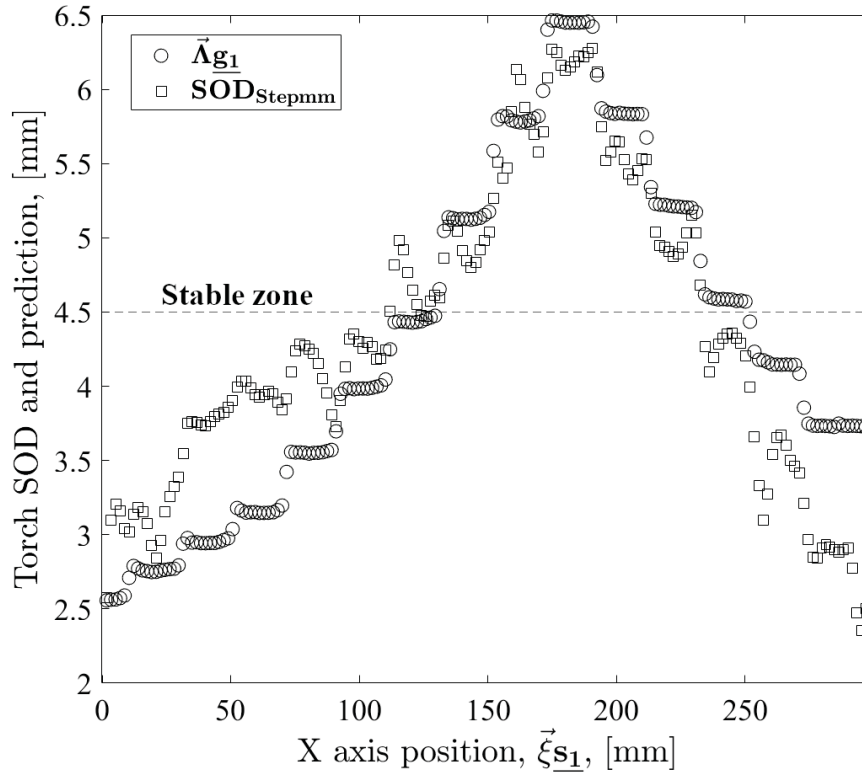
Figure 5.28: AED over the step GBTA in mm. After a SOD of 4.5 mm the SOD prediction is stable.

The predicted SOD average is 4.339 mm with a range of 3.924 mm, a standard deviation of 1.001 mm, and an uncertainty of 77 μm. Concerning the MSE and RMSD, the analysis report values of 0.277 mm^2 and 527 μm respectively. Figure 5.28 shows the laser measurement of the GBTA and the predicted SOD based on Equation 5.18.

Above a SOD of 4.5 mm, the prediction is better and stable. The lower section is closer to the torch where plasma arc is less stable; therefore, the variations in voltage are higher [Fig. 5.28].

A similar analysis is achieved for the ramp GBTA in millimetres. The regression Equation shown in 5.19 provides the intercept and coefficients to predict the SOD on the AED run for this GBTA.

$$SOD_{Rampmm} = -30.41 - 0.03I + 1.83V \qquad (5.19)$$
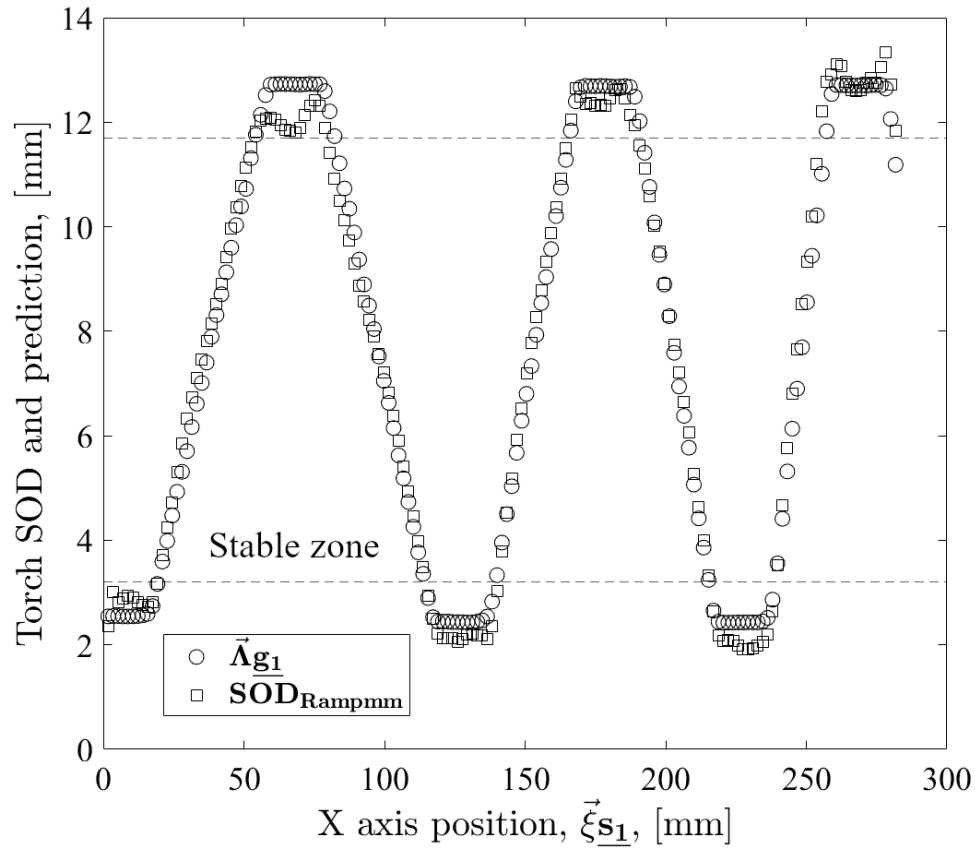
Figure 5.29: AED over the ramp GBTA in mm. An stable prediction can be obtained with a SOD between 3.2 mm and 11.7 mm.

The predicted SOD average is 7.721 mm with a range of 11.422 mm, an SD of 3.983 mm, and an uncertainty of 314 μm. When the laser measurement is compared

with the predicted SOD, a mean squared error of 0.1755 mm^2 and an RMSD of 419 μm are achieved. The stable zone for prediction is between 3.2 mm and 11.7 mm. A SOD close to the torch produces plasma arc instabilities due to short circuits with the nozzle. A large SOD develops plasma arc fluctuations due to the amount of energy required to keep it on [Fig. 5.29].

For the step GBTA in inches, the regression model provided the following Equation:

$$SOD_{Stepin} = 113.02 - 2.97I + 2.01V \tag{5.20}$$
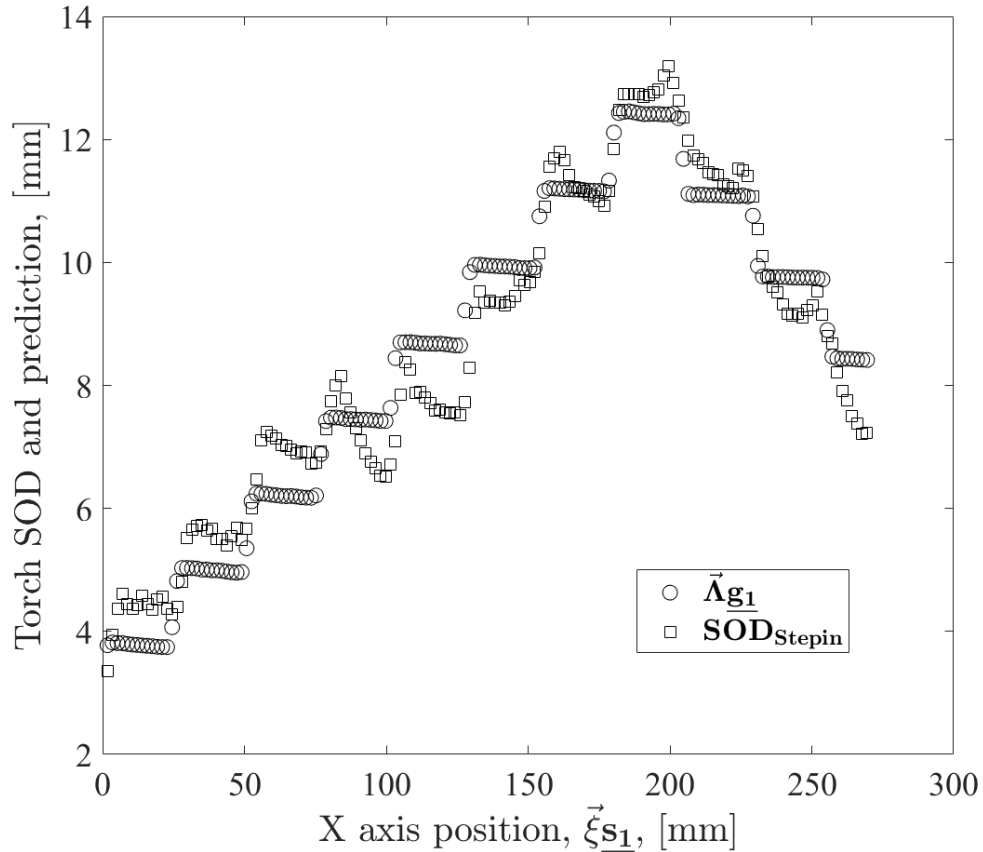
Figure 5.30: AED over the step GBTA in inches. The arc fluctuations are notable at higher step changes.

In the analysis of the step GBTA in inches, the average predicted SOD is 8.549 mm with a range of 9.826 mm; the standard deviation is 2.554 mm, and the uncer-

tainty is 206 μm. Comparing the predicted data with the actual GBTA, the MSE is 0.3869 mm^2, and the root-mean-squared deviation is 622 μm. In contrast with the step GBTA in mm, this GBTA has a constant step height of 1.27 mm (0.05 in), which causes higher plasma arc fluctuations between steps [Fig.5.30]. The distance between steps is short in the x-axis direction and does not allow the voltage to stabilize. The jump between steps induces a continuous deviation between the voltage and SOD. Besides the jump variations, each step starts with a sharp end. In these corners, the plasma electric field is stronger due to the excess of electrons. Negatively charged objects tend to distribute the particles in an attempt to reduce the effect of repulsive forces. Hence, charges are accumulated at a higher density in the location of the greater curvature, the step corner.

Finally, the analysis for the ramp GBTA in inches presents the following regression parameters:

$$SOD_{Rampin} = -19.57 + .03I + 1.17V \tag{5.21}$$

The predicted average SOD is 8.661 mm with a range of 11.037 mm, an SD of 3.326 mm, and an uncertainty of 259 μm. The error and deviation results at comparing the prediction against the actual SOD are 0.2488 mm^2 and 499 μm. The stable zone of the predicted SOD is between 3.3 mm and 11.3 mm in accordance with the ramp GBTA in mm. As stated before, the fluctuations in the voltage are caused by the short and long SOD that generate instabilities in the plasma arc [Fig. 5.31].

It is confirmed from the AED data that a voltage in-situ embedded sensor predicts the SOD of the torch in the PTA-AM system with certain limitations. The SOD has to be in a range between the 4.5 mm (approximate 0.17 in) and 11.3 mm (0.44 in). In the sensing limitations, the sensor is suitable to detect z-axis variations higher than 0.6 mm (0.02 in). Still, significant differences in the order of 1.27 mm (0.05 in) cause
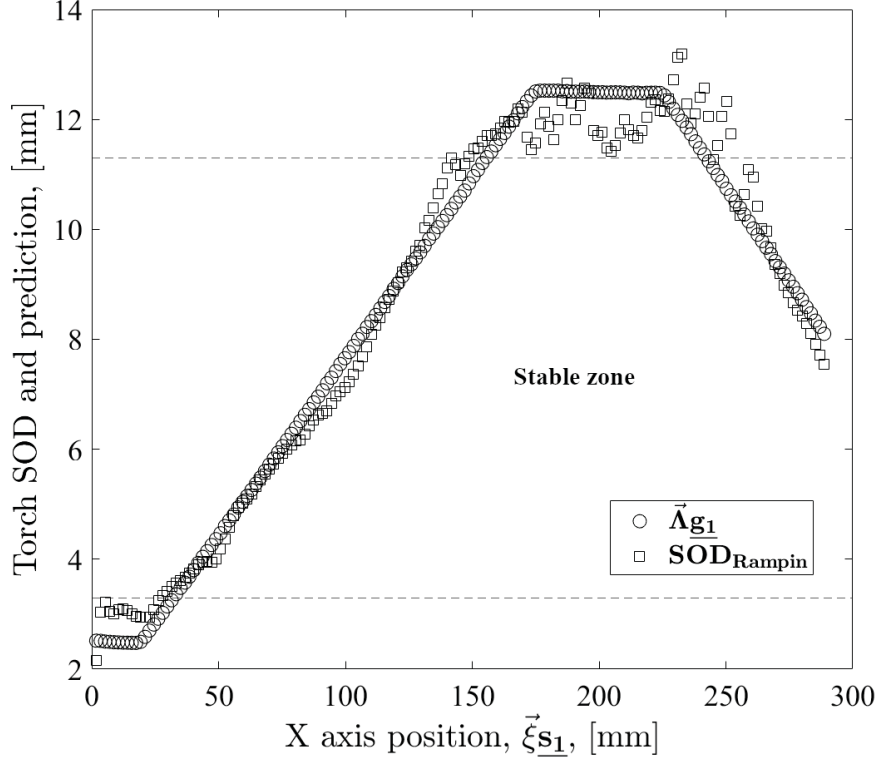
Figure 5.31: AED over the ramp GBTA in inches. The stable zone region is between 3.3 mm and 11.3 mm.

instabilities in the plasma arc. The deviation through the GBTAs is between 419 and 622 μm demonstrating suitable prediction, which can be improved by working in the limited range for the process parameters.

5.4 Validation

Validation of the embedded sensor is conducted by comparing the results in thirteen STSL depositions against its autogenous counterparts. The process parameters on each STSL bead are different to validate that the embedded sensor works regardless of the process parameter selection. Appendix E shows the relationship between experiments and process parameters, and this section provides a detailed analysis of five of the most relevant experiments. Additionally, single-track multiple-layer (STML) depositions in the shape of squares are printed to validate the effect of the voltage in

the perpendicular-to-deposition deviations. The influence generated by the current is neglected for the validation; therefore, only the direct relationship between voltage and SOD is considered.

5.4.1 Single-track single-layer analysis

V1 STSL bead analysis

Figure 5.32 shows the autogenous and deposition validation for the V1 STSL bead. A balling effect is shown for the deposition without achieving a continuous bead.
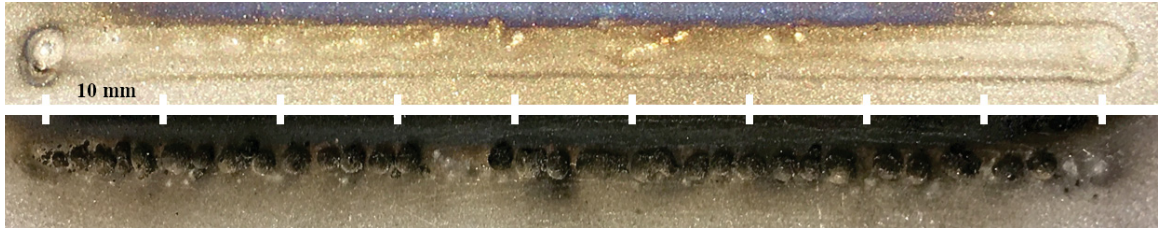
Figure 5.32: Autogenous and deposition results for STSL V1. A balling effect is noticed in the deposition sample.

With the voltage and laser profilometer data, linear regression models are obtained:

$$SOD_{V1A} = 1.06 + 0.15V \tag{5.22}$$

$$SOD_{V1D} = -13.78 + 0.83V \tag{5.23}$$

Table 5.10 provides the uncertainty analysis for the V1 STSL bead. The mean values are similar in the actual and predicted numbers for the autogenous and the deposition. The range decreases in the predicted values, and the standard deviation and uncertainties are higher for the deposition. The mean square error between the predicted SOD and the actual SOD is 0.043 mm^2 in the autogenous sample, and 0.327 mm^2 for the deposition sample. Comparing the root-mean-squared deviation, the autogenous is 206 μm, and for the deposition is 527 μm. The increment in the

measurements of the deposition sample, excluding the mean, is because of the presence of the balling effect. The decline in the mean value is because the deposition of material generates a lower SOD in relationship with the autogenous sample.

Table 5.10: Uncertainty analysis for the validation in the V1 STSL bead.

V1	Autogenous		Deposition	
	SOD	*Prediction*	*SOD*	*Prediction*
Mean [*mm*]	4.796	4.816	3.455	3.455
Range [*mm*]	0.889	0.620	2.374	1.569
SD [*mm*]	0.267	0.135	0.630	0.251
Uncertainty [μm]	34	17	88	35
MSE [mm^2]	0.043		0.327	
RMSD [μm]	206		572	

Figure 5.33 demonstrates the differences in the prediction of the SOD in the V1 autogenous and deposition STSL. The decline in the autogenous graph is due to the heat deformation of the substrate during the AED. The significant variations in the deposition graph show that the in-situ embedded sensor cannot pick up the balling effect with the voltage measurement. This limitation is because the distance between non-coalescence metal droplets is short, allowing the arc to jump between them with small perturbations. Besides this constraint, the voltage sensor detects the bead height with an RMSD of 572 μm.

The difference between the autogenous and deposition predictions allows the in-situ measurement of the voltage to collect the bead height [Fig.5.34]. The bead height dispersion is a consequence of the small perturbations in the arc due to the balling effect. The range of the predicted bead height is 1.653 mm.
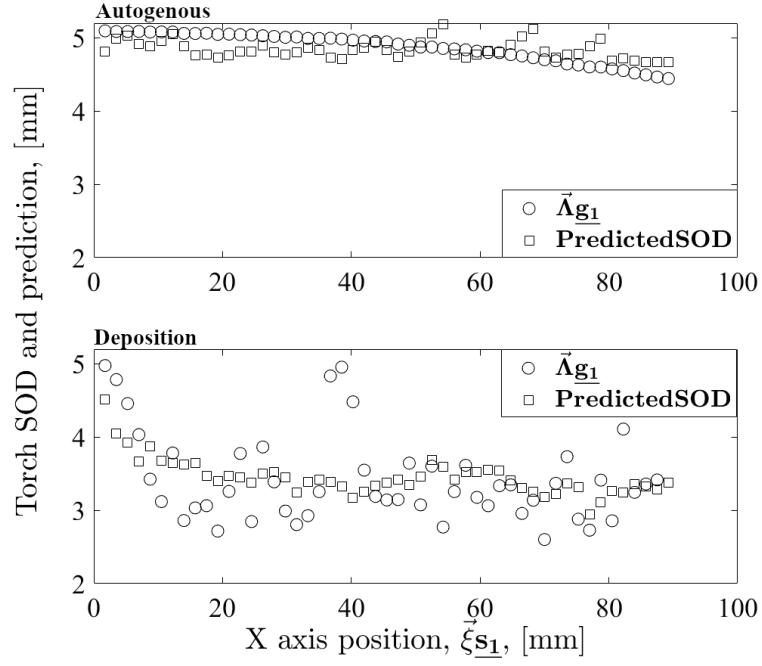
Figure 5.33: Autogenous and deposition predictions. The SOD in the deposition is lower due the balling deposition.
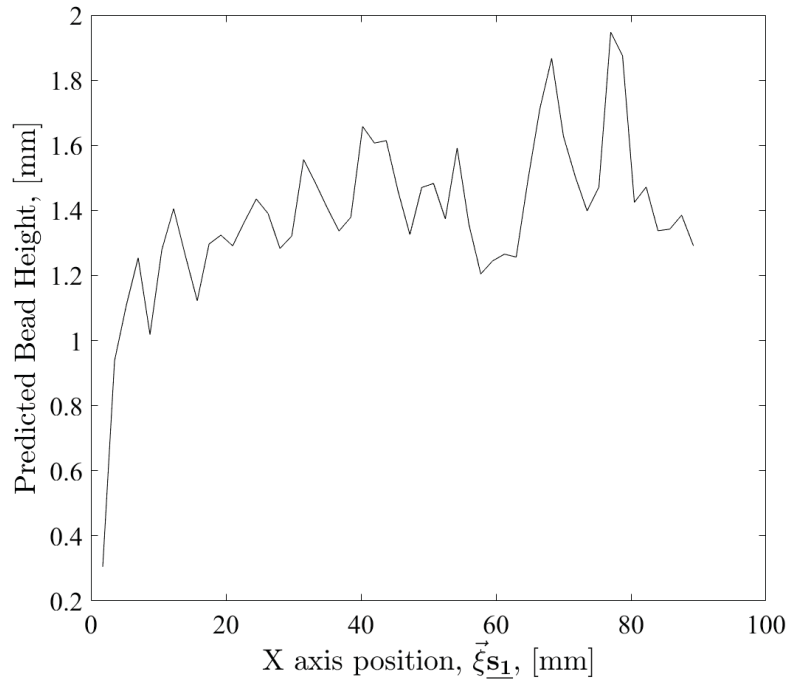
Figure 5.34: Bead height prediction based on voltage in-situ measurement for V1 STSL bead.

Figure 5.35 exhibits the statistical summary for the STSL V1 bead. There is less variation in the predicted values for the autogenous than on the deposition sample. The deviation is more evident in the deposition case because the sensor cannot detect the changes due to the balling effect, but the laser profilometer can. As stated previously, the mean value difference between the autogenous and deposition cases is due to the material being deposited in the deposition.
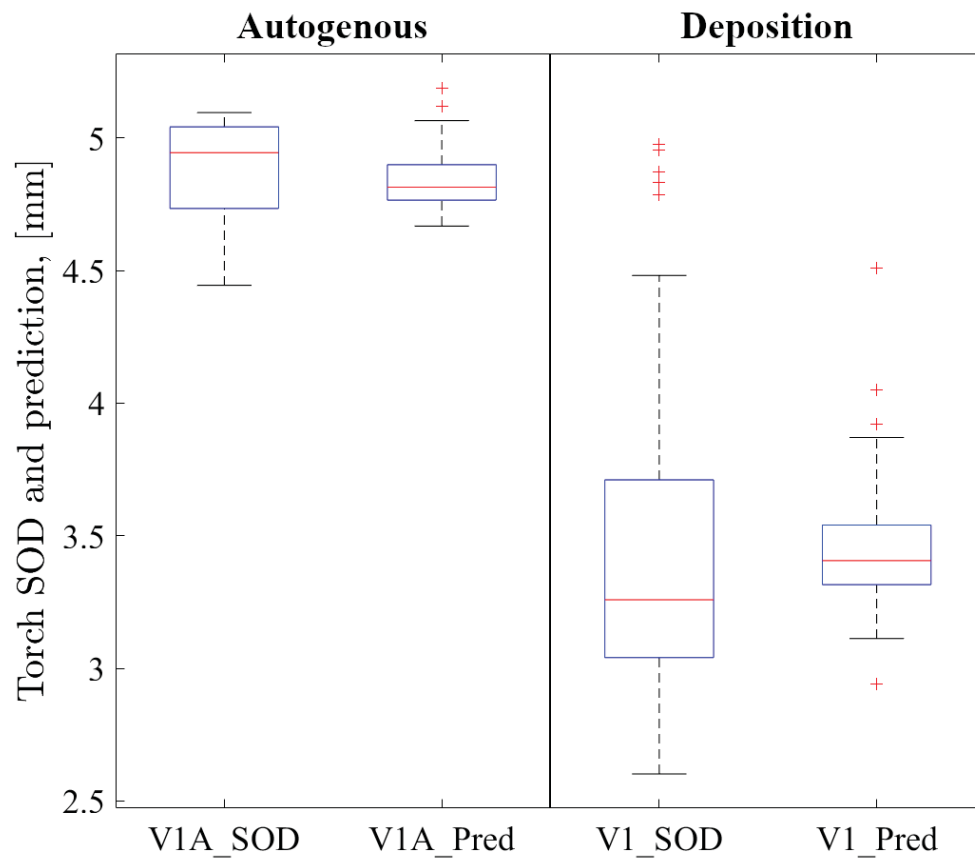
Figure 5.35: Summary statistics for the SOD and predicted SOD for autogenous and deposition of V1 STSL bead.

V2 STSL bead analysis

Figure 5.36 presents the autogenous and deposition of the V2 STSL. In the AED, there are waves at both sides of the bead. These waves are a consequence of the intense heat input exerted into the substrate, forcing out the melt pool's material. This phenomenon is called humping bead formation.
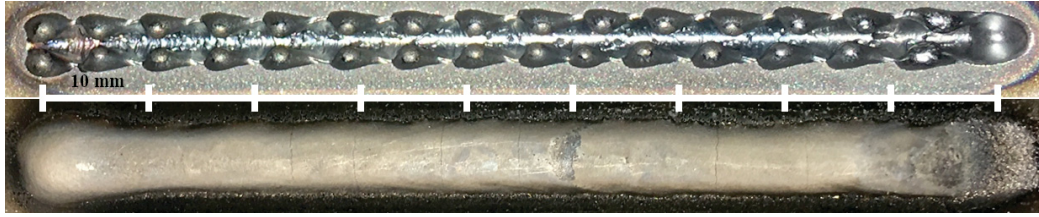
Figure 5.36: Autogenous and deposition results for STSL V2.

The data collected in V2 autogenous and deposition samples provide the information required to implement a linear regression for both scenarios. Equations 5.24 and 5.25 show the intercepts and coefficients to predict the SOD for each case.

$$SOD_{V2A} = 16.00 - 0.13V \tag{5.24}$$

$$SOD_{V2D} = 15.22 - 0.15V \tag{5.25}$$

Concerning the predicted data, the uncertainty analysis is presented in Table 5.11. The mean values are the same for predicted and actual SOD being 11.385 mm for autogenous and 9.351 mm for deposition. The increment in SOD for the autogenous is produced by the lack of material being deposited. The range and standard deviation in the autogenous SOD are higher than in the prediction. This variation is because of the waviness due to the excess heat in the AED. Therefore, the voltage sensor is not able to predict the waviness in the substrate. The uncertainty is higher in the autogenous SOD due to the variance caused by the peaks and valleys in the humping

bead formation. Comparing the SOD with the predictions, the MSE and the RMSD are higher in the autogenous case than in the deposition sample. The higher values in the autogenous case indicate that the bead deposition can be predicted accurately, but the sensor does not detect the waviness generated in the AED. In the AED, the plasma arc travels over the substrate without material deposition. The heat generates a humping bead formation in which its peaks and valleys are independent of the voltage's fluctuations.

Table 5.11: Uncertainty analysis for the validation in the V2 STSL bead.

V2	Autogenous		Deposition	
	SOD	*Prediction*	*SOD*	*Prediction*
Mean $[mm]$	11.385	11.385	9.351	9.351
Range $[mm]$	3.501	0.311	1.392	0.334
SD $[mm]$	0.857	0.084	0.223	0.096
Uncertainty $[\mu m]$	113	11	31	13
MSE $[mm^2]$	0.716		0.040	
RMSD $[\mu m]$	846		199	

Figure 5.37 presents the graph of the torch stand-off-distance and its predicted values. The variance displayed by the laser in the autogenous case corresponds to the waviness in the substrate. The predicted values remain constant, confirming that the sensor is unable to capture these variances. On the other hand, the predicted and actual SOD for the deposition case affirms that the sensor detects the variations accurately within a deviation of 200 μm.

The bead height is measured with the difference from the predicted values from the AED and the deposition. The plunge at the end of the bead is also predicted [Fig. 5.38].
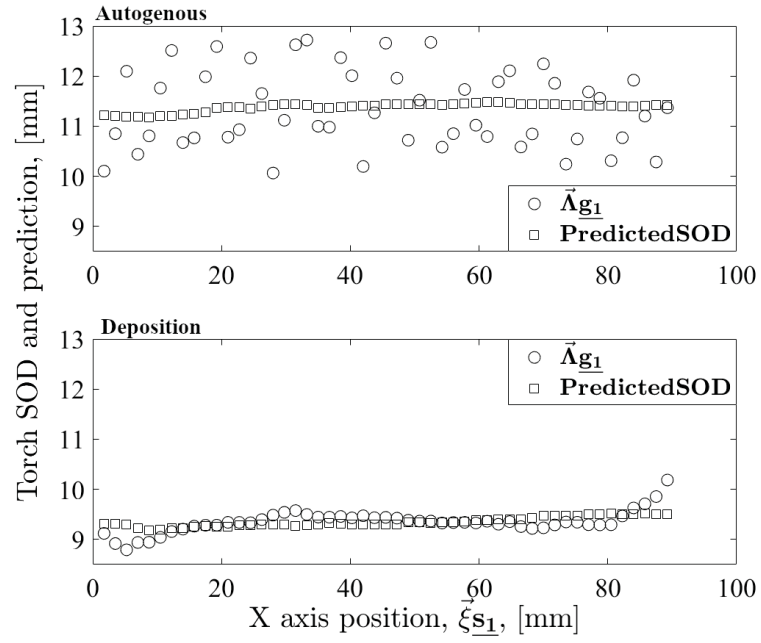
Figure 5.37: Autogenous and deposition predictions. Waviness in the AED is unable to be captured by the in-situ sensor.
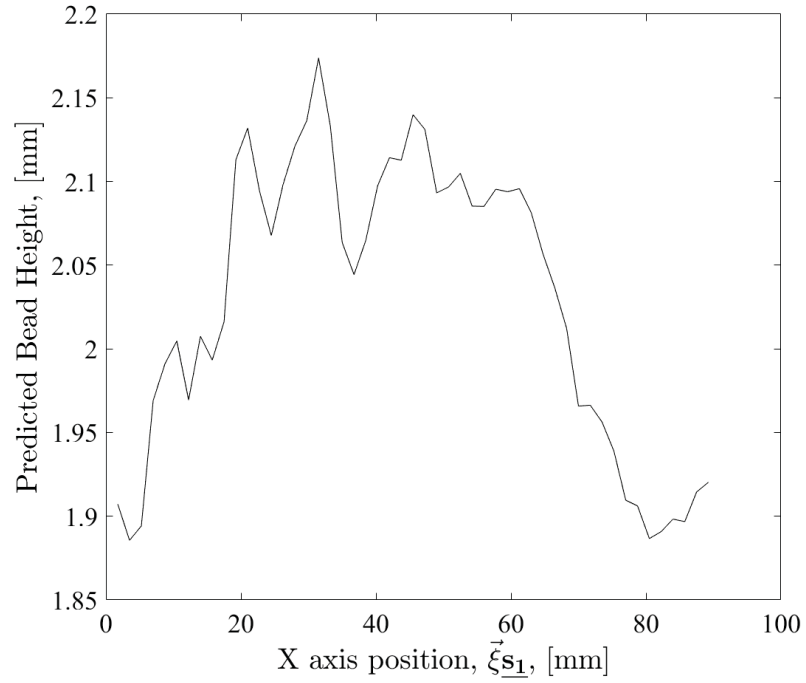
Figure 5.38: Bead height prediction based on voltage in-situ measurement for V2 STSL bead.

The range in the bead height prediction is 288 μm, establishing that it is predicted accurately.

Figure 5.39 shows the statistics summary of the SOD and predicted SOD for the V2 STSL bead. The data for the deposition case is very similar contrary to the one presented for the autogenous sample, which is an indicator of an accurate prediction. As stated previously, the difference in the dispersion shown for the autogenous case is due to the voltage sensor's inability to record the waviness in the humping bead formation of the substrate.
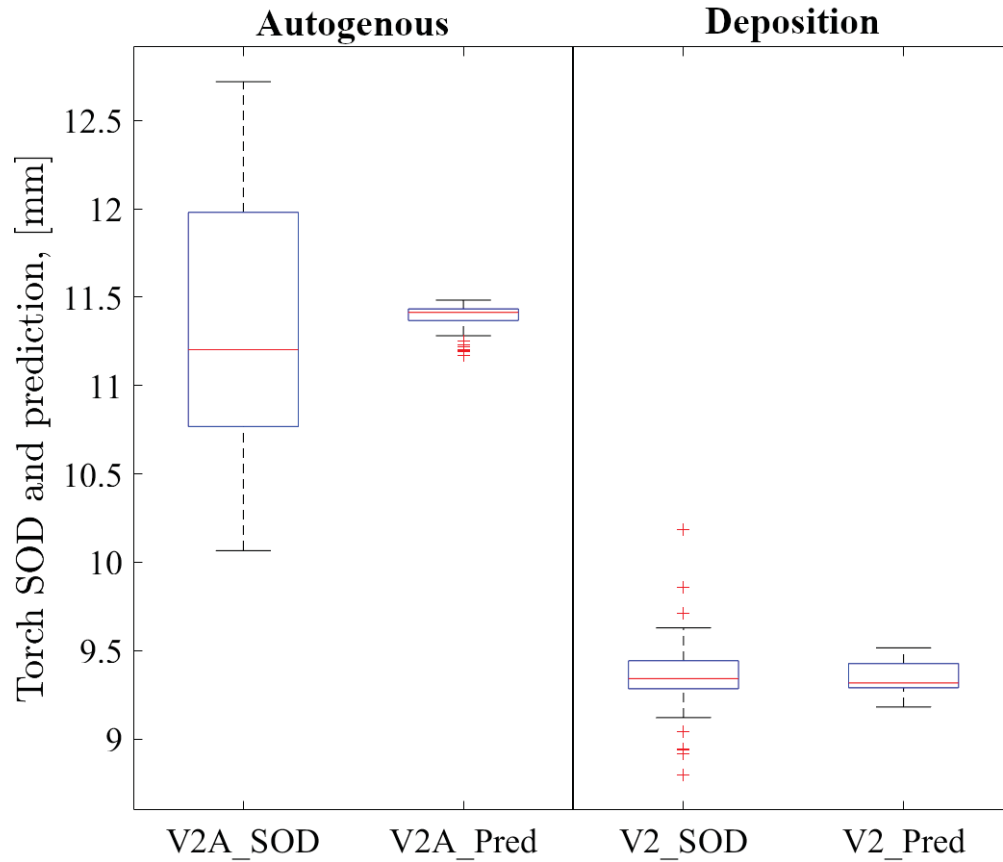
Figure 5.39: Summary statistics for the SOD and predicted SOD for autogenous and deposition of V2 STSL bead.

V5 STSL bead analysis

The STSL V5 bead's process parameters generated a balling effect with wider discontinuities in the deposition compared to the balling in the STSL V1 bead [Fig. 5.40]. This type of behaviour occurs due to the combination of increased powder flow and low current. For the AED, the substrate remained with minimum changes, apart from showing a heat-affected zone through the travel of the plasma arc.
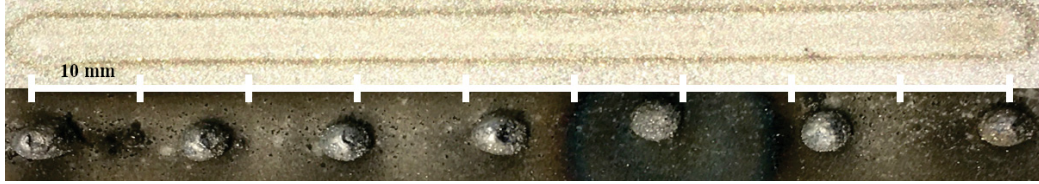
Figure 5.40: Autogenous and deposition results for STSL V5.

The Equations 5.26 and 5.27 present the coefficients and intercepts obtained for the linear regression corresponding to the STSL V5 bead.

$$SOD_{V5A} = 12.07 - 0.04V \tag{5.26}$$

$$SOD_{V5D} = -20.45 + 1.04V \tag{5.27}$$

The uncertainty analysis of STSL V5 shows a lower SOD mean value for the deposition due to the material being deposited [Table 5.12]. Additionally, the STSL V5 bead's deposition case has a higher range and standard deviation caused by the balling deposition. A critical difference compared to the balling presented in the STSL V1 bead is the spacing of the material. The STSL V5 bead has a broader distance between accumulated depositions, allowing the in-situ sensor to detect it.

The detection is supported by the low deviation between the SOD and the predicted SOD in the deposition case. The uncertainty, the MSE, and the RMSD are orders of magnitude smaller in the autogenous case in comparison to the deposition.

Table 5.12: Uncertainty analysis for the validation in the V5 STSL bead.

V5	Autogenous		Deposition	
	SOD	Prediction	SOD	Prediction
Mean [mm]	10.971	10.971	9.973	9.973
Range [mm]	0.208	0.038	3.413	3.295
SD [mm]	0.062	0.010	1.044	0.894
Uncertainty [μm]	8	1	146	125
MSE [mm^2]	0.004		0.285	
RMSD [μm]	61		534	

Comparing the graphs from the autogenous and deposition cases, the prediction on the autogenous is stable due to the low current applied. Low current creates low heat transfer to the substrate, hence, less distortion. In the deposition graph, the dispersion is more significant for both measurements, the laser profilometer and the prediction. The predicted SOD follows the laser profile with a deviation of 534 μm, meaning that the in-situ sensor distinguishes the balling effect. Large spacing between depositions allows the sensor to detect the voltage fluctuations. The detection is noticed by the seven regions with lower stand-off-distance shown due to the deposited spots on the substrate [Fig. 5.41].

With the information provided by the predicted values in the autogenous and deposition cases, the bead height is achieved [Fig. 5.42]. The seven peaks in the balling deposition were detected accurately.
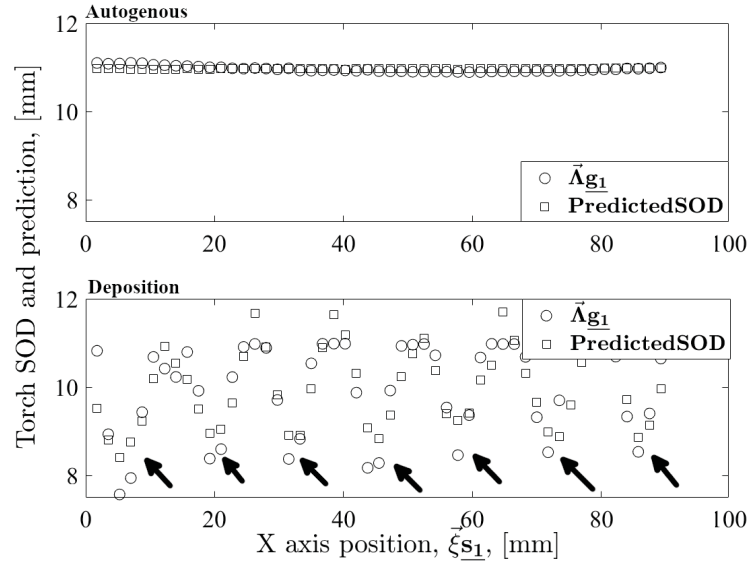
Figure 5.41: Autogenous and deposition predictions. The in-situ sensor is able to detect the seven balling depositions.
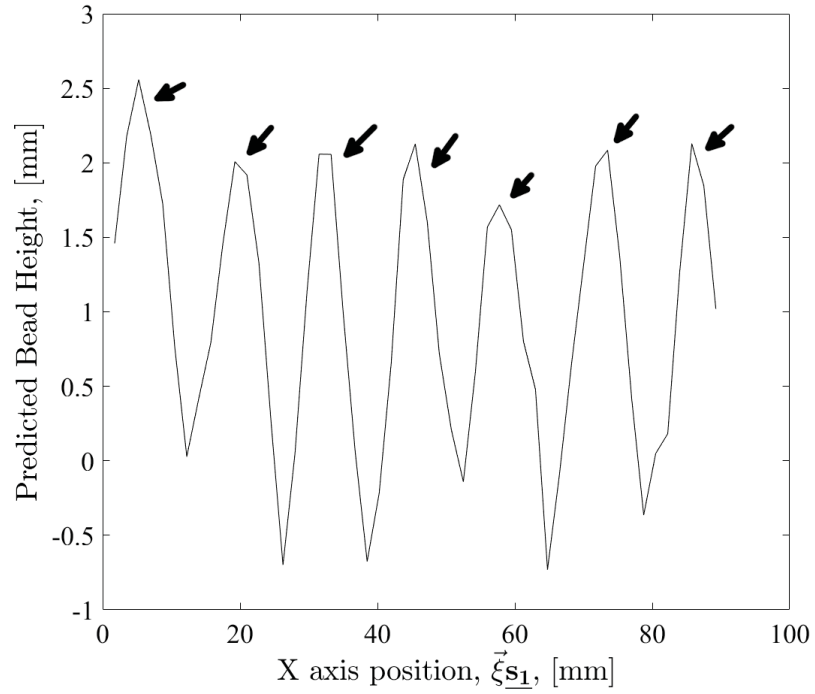
Figure 5.42: Bead height prediction based on voltage in-situ measurement for the STSL V5 bead.

Figure 5.43 provides insight into the statistic summary for the STSL V5 bead. Although the dispersion in the autogenous case is low, the prediction's deviations are smaller compared to the actual laser measurement. However, for the deposition case, the laser data and the predicted data are in agreement. That is an indication of the in-situ sensor detecting the balling in the deposition. The difference between the cases is due to the material being deposited in the second case, which lowers the SOD.
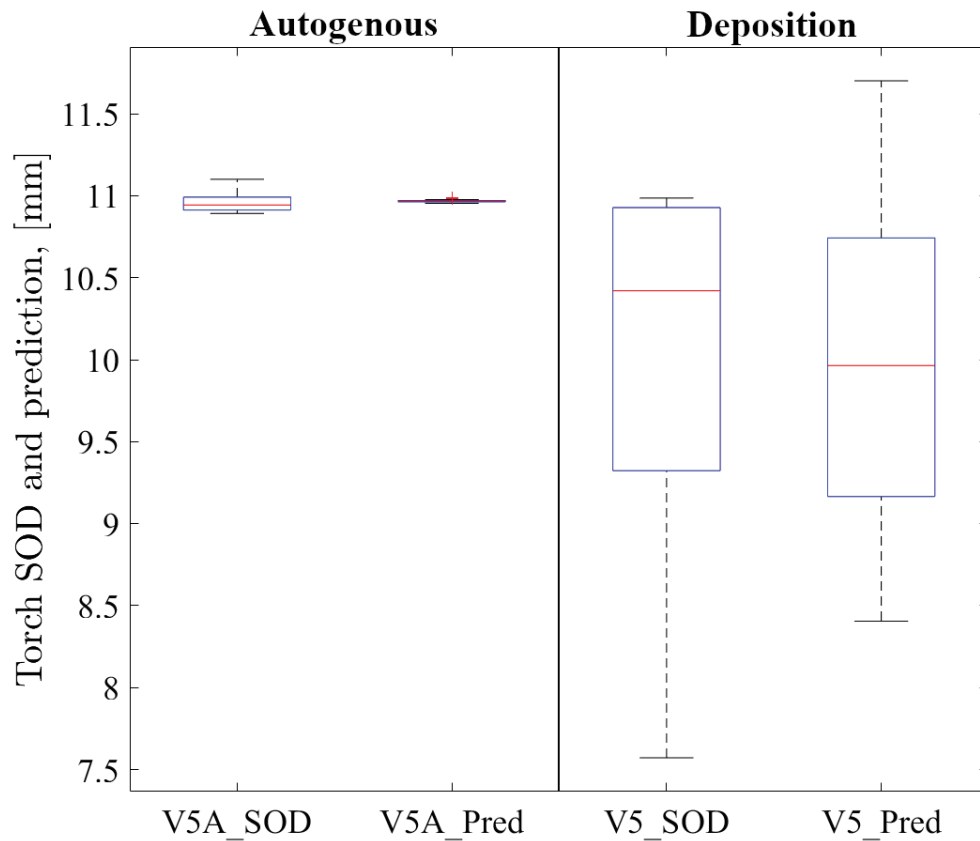
Figure 5.43: Summary statistics for the SOD and predicted SOD for autogenous and deposition of the STSL V5 bead.

V6 STSL bead analysis

The STSL V6 bead deposition presents an even material distribution. On the other hand, its AED generates a humping bead formation similar to the one shown in the STSL V2 bead but with less waviness [Fig. 5.44].
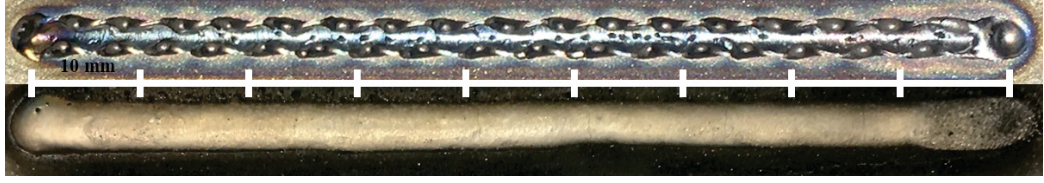
Figure 5.44: Autogenous and deposition results for STSL V6.

The linear regression between the voltage and the laser measurements provides the coefficients and intercepts for the autogenous and deposition cases:

$$SOD_{V6A} = 16.30 - 0.28V \tag{5.28}$$

$$SOD_{V6D} = -4.06 + 0.32V \tag{5.29}$$

For the uncertainty analysis presented in Table 5.13, the mean value of the SOD and the predicted SOD in the deposition is 5.644 mm. The mean is lower than in the autogenous case since the material is deposited in the substrate. The range, the standard deviation, and the uncertainty are higher in the laser measurement of the autogenous case because it responds to the waviness produced by the AED. On the other hand, the voltage sensor cannot detect the waviness caused by the heat input. The MSE and the RMSD are lower for the deposition case, which means that a accurate prediction is established.

Table 5.13: Uncertainty analysis for the validation in the V6 STSL bead.

V6	Autogenous		Deposition	
	SOD	Prediction	SOD	Prediction
Mean [mm]	8.007	8.007	5.644	5.644
Range [mm]	1.257	0.186	0.413	0.342
SD [mm]	0.252	0.046	0.106	0.082
Uncertainty [μm]	33	6	14	11
MSE [mm^2]	0.060		0.004	
RMSD [μm]	245		66	

Figure 5.45 shows the autogenous and deposition SOD and predicted SOD for the V6 STSL bead. The differences in the autogenous case for the laser and predicted SOD are due to the laser data detecting the substrate waviness caused by the pass of the plasma arc. The voltage sensor cannot identify the effects of the humping bead formation; therefore, some deviations are present in the graph. In the deposition case, the prediction is stable and agrees with the information from the laser profilometer showing an acceptable SOD prediction with a deviation of 66 μm according to the uncertainty analysis.

For the V6 STSL bead, the SOD predictions for the autogenous and deposition provide the bead height in the deposition. Figure 5.46 shows the development of the bead height through the x-axis position. The bead is stable with a continuous increment in the bead height in a range of 447 μm. The increase in the bead height is due to thermal accumulation, which allows more material to attach to the bead as the printing process progresses.
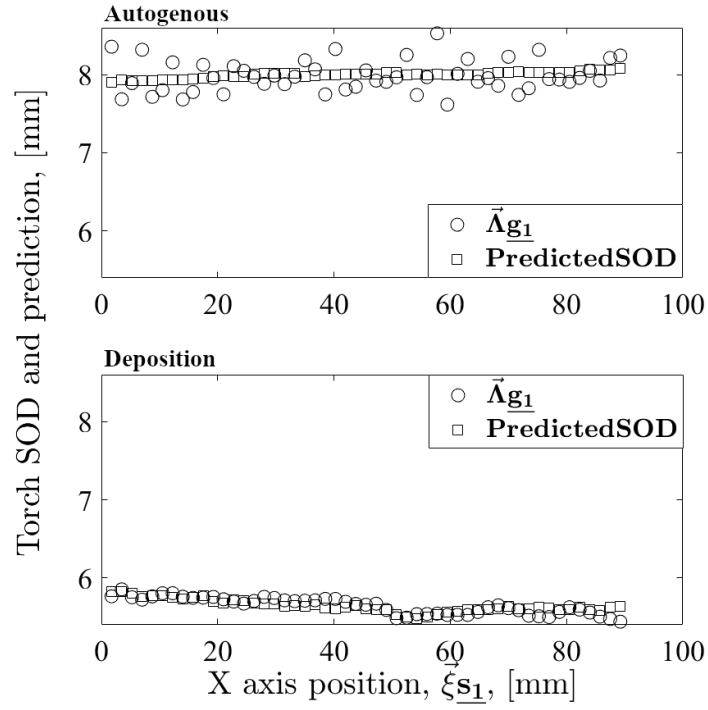
Figure 5.45: Autogenous and deposition SOD and SOD predictions in the V6 STSL. The waviness is detected in the autogenous laser profilometer, but not by the in-situ sensor.
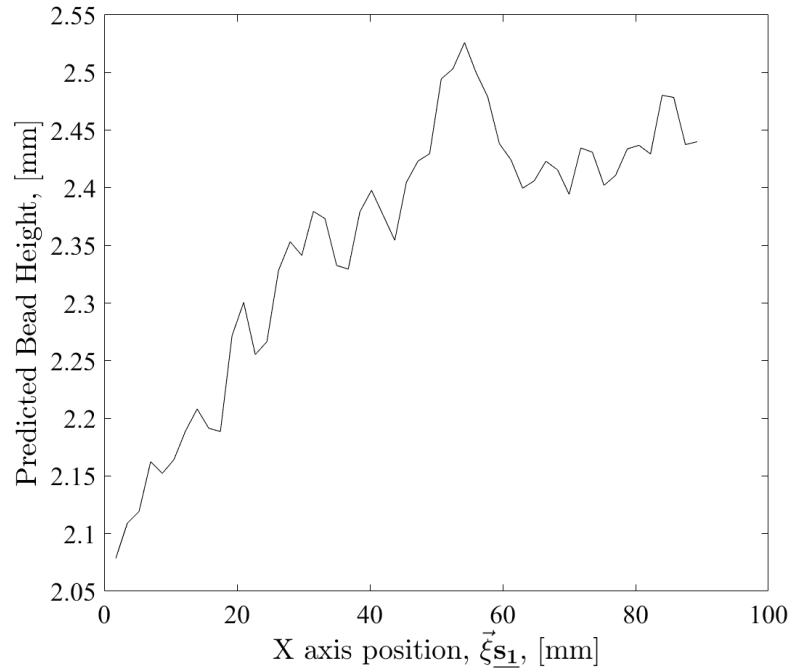
Figure 5.46: Bead height prediction based on voltage in-situ measurement for V6 STSL bead.

The statistical summary of the STSL V6 bead shows statistical agreement in the deposition data [Fig. 5.47]. Additionally, the predicted deviations in the autogenous and deposition cases are lower than in the measured SOD. Smaller predicted variations imply that the voltage sensor dismisses some features detected by the laser sensor. More specifically, the difference between the laser and the predicted data is due to the waviness phenomenon that the in-situ voltage sensor cannot distinguish.
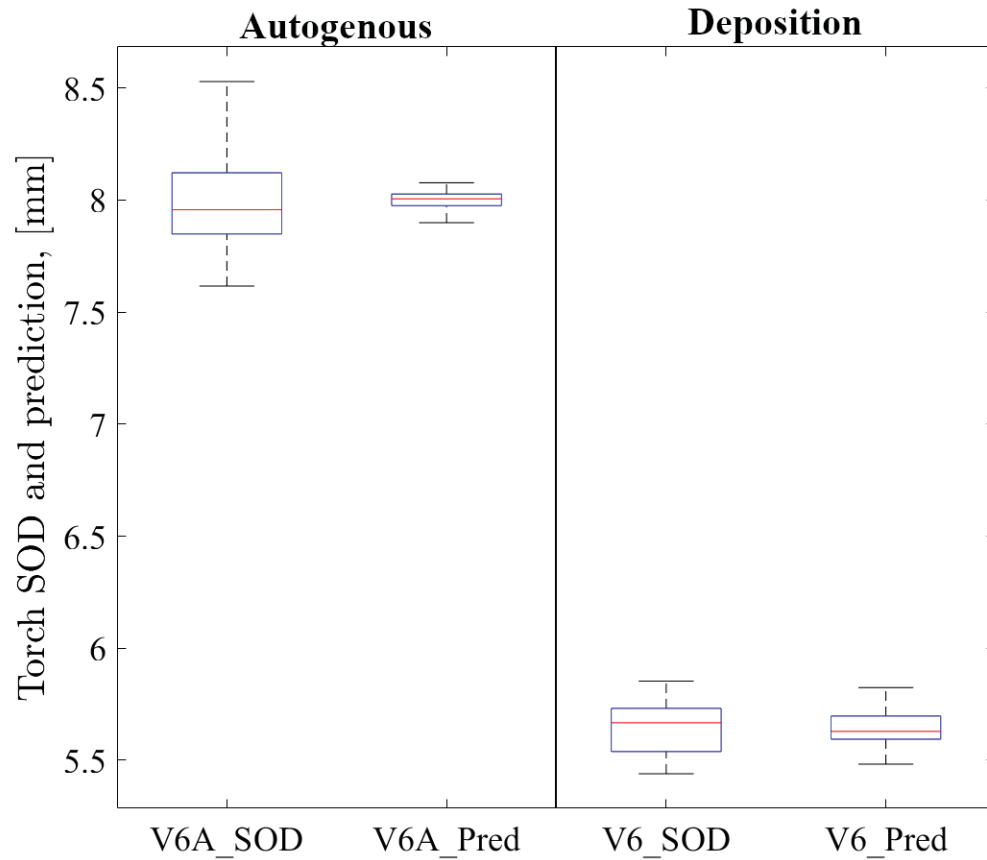
Figure 5.47: Summary statistics for the SOD and predicted SOD for autogenous and deposition of the STSL V6 bead.

STSL bead with recommended parameters analysis

The last validation for the STSL beads is through printing a bead with the recommended parameters presented in Table 5.9 of section 5.3.2. Figure 5.48 shows the

autogenous and deposition images for the recommended STSL. The deposition is notably thinner in the bead than in the previous STSL beads.
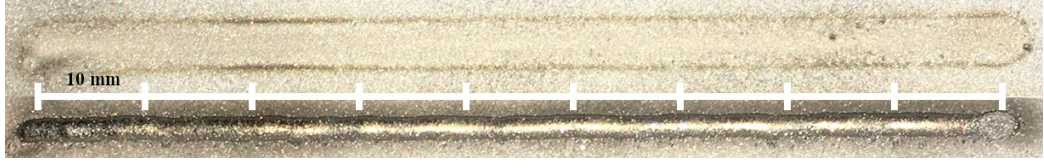
Figure 5.48: Autogenous and deposition results for a STSL bead printed with the recommended process parameters.

The following linear regressions are obtained by processing the data collected from the laser and the voltage in the autogenous and deposition cases:

$$SOD_{OptA} = -15.35 + 0.78V \tag{5.30}$$

$$SOD_{OptD} = 10.25 - 0.21V \tag{5.31}$$

The uncertainty analysis presented in Table 5.14 shows similar behaviour to the previous STSL when comparing the mean values of the autogenous and deposition cases. In the deposition case, the SOD is reduced due to the material being deposited to the substrate. In the autogenous case, the differences in the range, the standard deviation, and the uncertainty are minimal, which indicates a small impact to the substrate during the AED. Concerning the deposition, there are few perturbations in the bead that are detected by the laser profilometer but not by the in-situ sensor. These deviations are in the order of 136 μm, according to the RMSD.

The SODs data detected by the laser, and the predicted SOD are compared in the autogenous and deposition cases depicted in Figure 5.49. The decremented SOD in the autogenous case is due to heat accumulation in the substrate. More differences

Table 5.14: Uncertainty analysis for the validation in the STSL bead with the recommended process parameters.

Optimal	Autogenous		Deposition	
	SOD	*Prediction*	*SOD*	*Prediction*
Mean [mm]	5.961	5.961	4.189	4.189
Range [mm]	0.505	0.510	0.717	0.300
SD [mm]	0.138	0.110	0.156	0.075
Uncertainty [μm]	16	13	18	9
MSE [mm^2]	0.007		0.018	
RMSD [μm]	82		136	

are found in the deposition case. These differences, although minimum, are due to small variations detected in the bead by the laser profilometer, but not by the voltage sensor. The deviations could have been generated by coalescence of molten metal material and surface tension forces that deform the bead after the travel of the plasma arc; therefore, these variations are not captured by the voltage sensor.

The bead height is predicted with the information provided through the SOD prediction in the autogenous and deposition runs [Fig. 5.50]. The bead height for the STSL bead with recommended process parameters varies in a range of 537 μm.
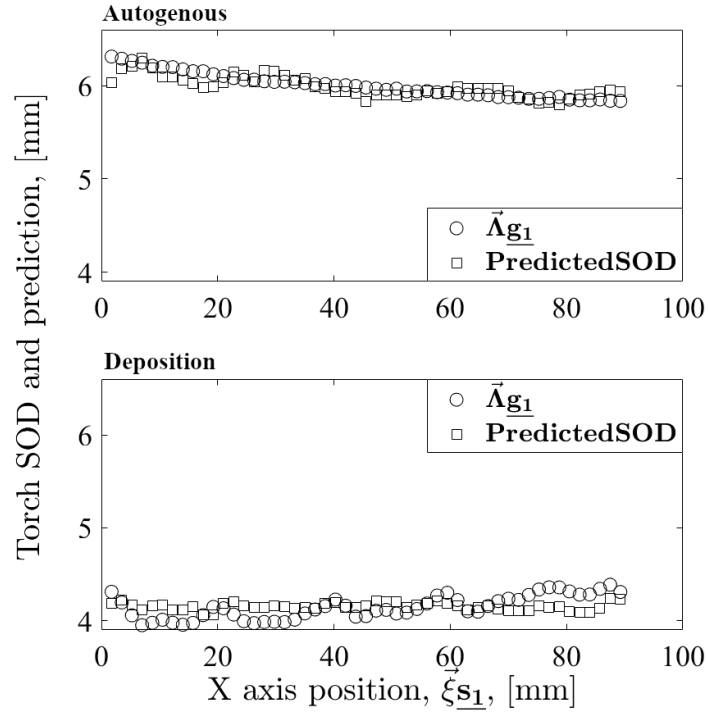
Figure 5.49: Autogenous and deposition predictions for the STSL bead with recommended process parameters. The deposition has some perturbations detected by the laser profilometer but not by the in-situ voltage sensor.
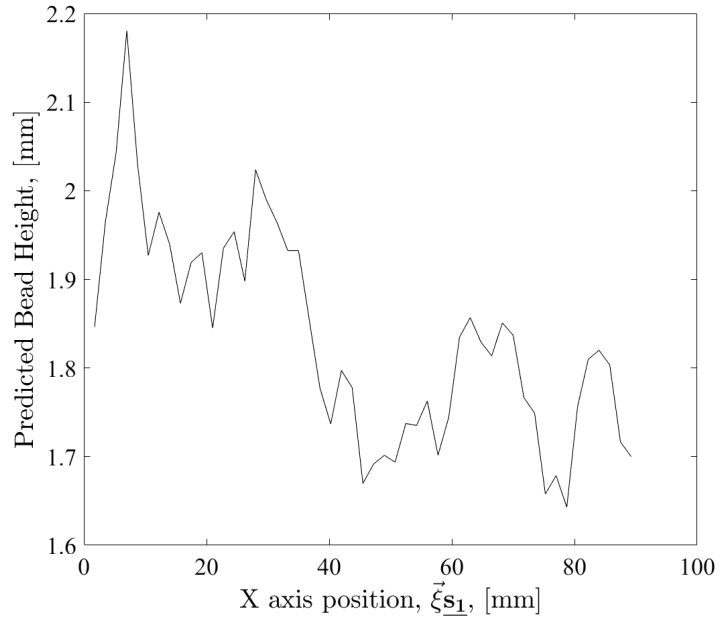
Figure 5.50: Bead height prediction based on voltage in-situ measurement for the STSL bead with recommended process parameters.

Figure 5.51 presents the statistical summary for the STSL bead with recommended process parameters. The autogenous SOD and predicted SOD show statistical agreement in the data. For the deposition case, the deviation is higher in the laser profilometer due to the variations detected in the bead, but the predicted SOD has a lower difference because the in-situ sensor does not recognize those variations.
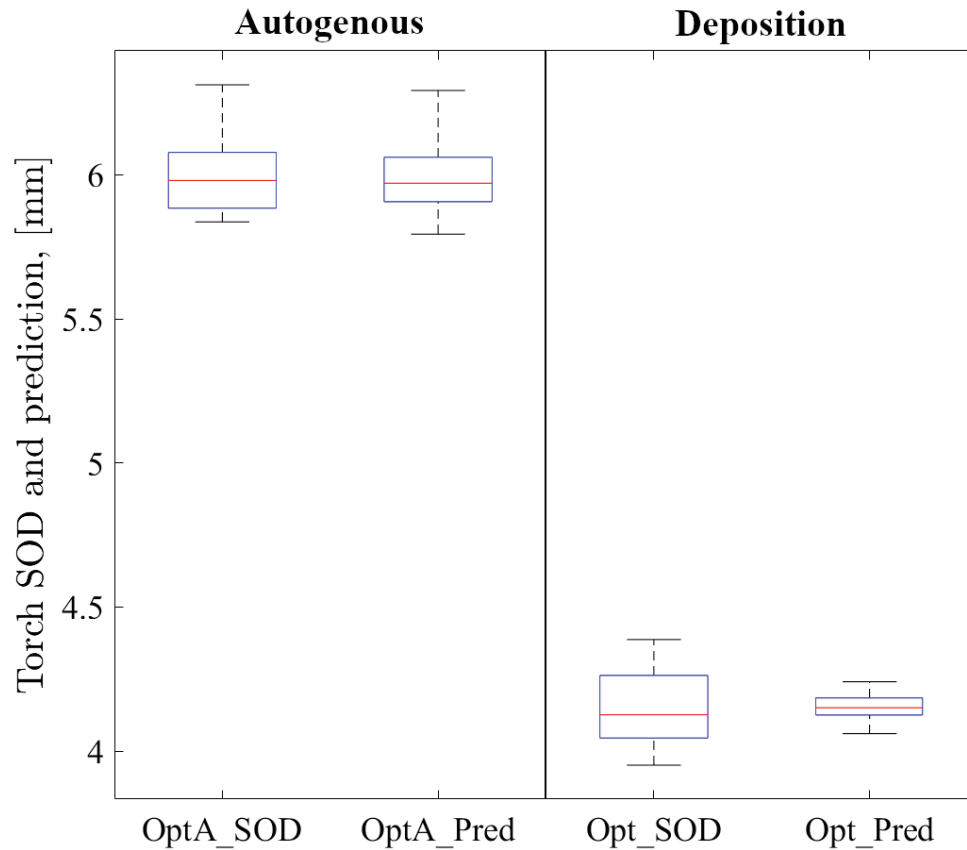
Figure 5.51: Summary statistics for the SOD and predicted SOD for autogenous and deposition of the STSL bead with recommended process parameters.

Other STSL information was collected and analyzed, but only those with critical characteristics were fully described in this section. All of the other uncertainty analyses are shown in Appendix E. Additionally, the information regarding the process parameters is shown as well in the appendix.

5.4.2 Perpendicular-to-deposition voltage sensor validation

The information for the in-situ voltage sensor and the positioning device is linked to supply data on the perpendicular-to-deposition faces. Figure 5.52 shows the voltage measured at different positions along the x, y, and z-axes during the printing of an STML deposition with a cuboid shape.
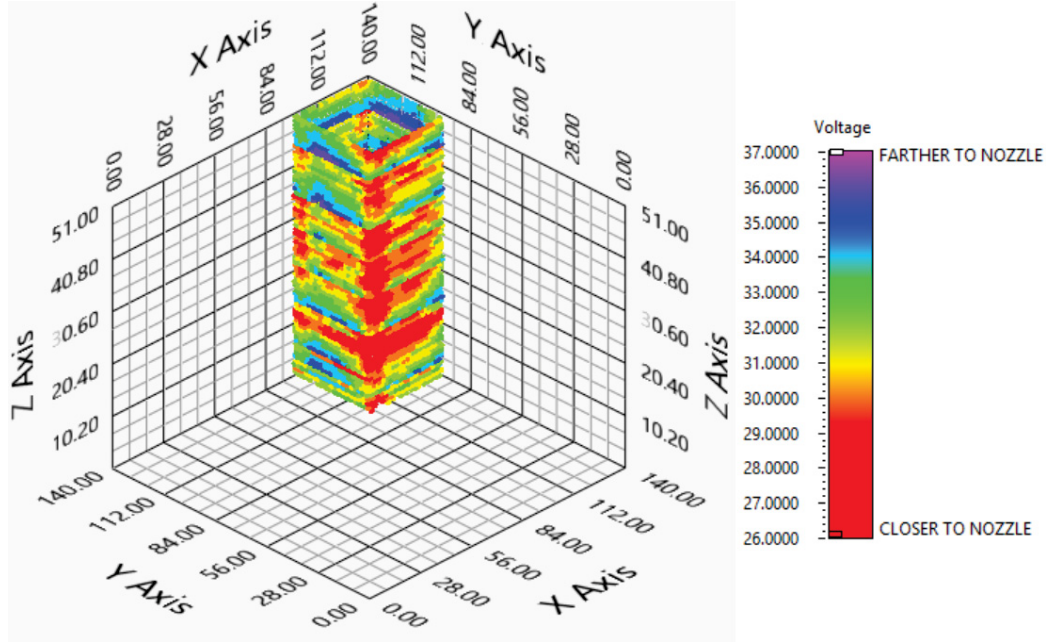
Figure 5.52: Voltage measured in a single-track multiple-layers deposition with a cuboid shape.

The cuboids measure 40 mm in length, 40 mm in width, and 50 mm in height. The deposition begins at the position of 100 mm in the x-axis, 100 mm in the y-axis, and 0 mm in the z-axis. The material is 17-4PH stainless steel in powder form deposited on open-loop mode; therefore, there is no feedback from the sensors to modify the position or the process parameters.

For the validation of the perpendicular-to-deposition response, three different STML samples were considered. Table 5.15 shows the selected process parameters. Side A, side B, and side C were laser scanned from each sample to detect the perpendicular-

to-deposition deviation (PDD) and to compare it against the mid-section (20 mm) voltage.

Table 5.15: Process parameters for the perpendicular-to-deposition side deviations

Sample	Powder gas (slpm)	Shielding gas (slpm)	Center gas (slpm)	Nozzle angle	Powder flow rate (gpm)	Current (A)	Table speed (mm/min)
1 (S2)	2	13	2	45°	25	60	800
2 (S4)	2	13	2	45°	30	50	800
3 (S5)	2	13	2	45°	30	60	700

Single-track multiple-layer S2 validation

The sides A, B, and C for sample STML S2 are depicted in Figure 5.53. The part was shorter than the expected 50 mm height due to the lack of deposition in some regions. The torch was manually adjusted to compensate for the difference between the deposited bead and the actual printing distance from the torch. A couple of adjustments are notable by sight in the mid-height section and 10 mm before the top of the part. These kinds of perturbations generate deviations in the perpendicular-to-deposition sides of the printed components. Additionally, the lack of fusion in some regions produces the deposition of metal spatter, which changes the surface finish of the sides.

Figure 5.54 shows the voltage in the sides during the deposition process. It is notable that from height 0 to 20 mm, the voltage is dropping, and at z=20 mm, the torch is manually adjusted. Although adjusted, there is a voltage deviation observed on the left of side C. At z=30 mm and z=32 mm, the torch is adjusted again. Still,
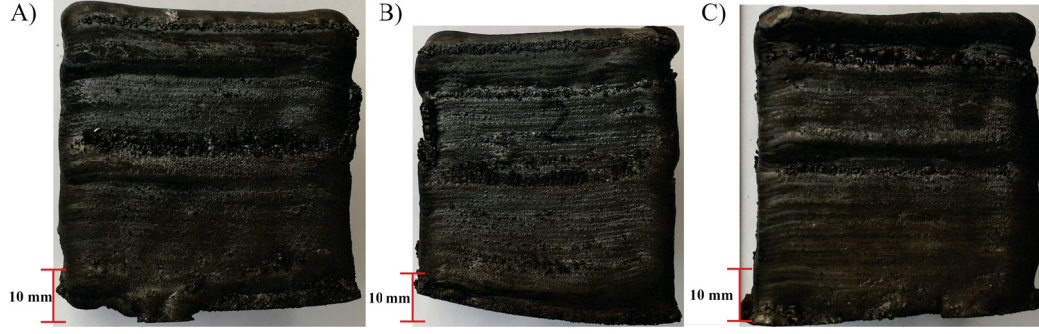
Figure 5.53: Sides of the STML sample S2. There are two notable changes in the bead due to manual adjustment of the nozzle.

the voltage remains constant in the right of side B and the left of side C, between z=32 mm and z=43 mm. At z=43 mm, the data show another torch's adjustment.
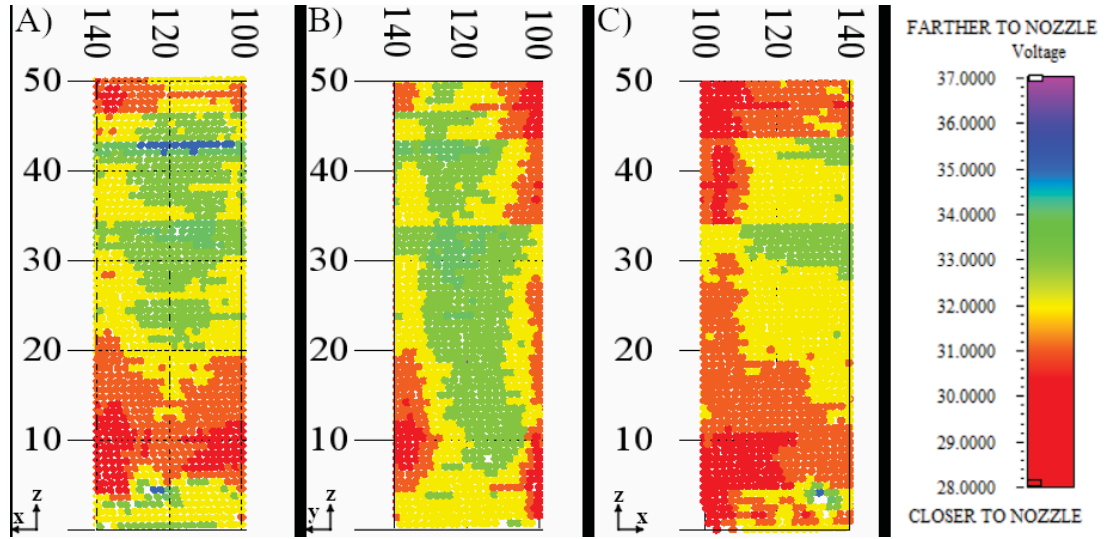
Figure 5.54: Voltage measurement for the STML S2 sides. The point-wise value of the voltage provide information regarding the material's deposition.

Linear regressions to determine the PDD based on the voltage are obtained with the information provided by laser scanning each side. The scanning data collected at the mid-section of the side is processed to be aligned perpendicular to the deposition. For the voltage, the mid-section point value for each layer is considered for the analysis. Equations 5.32, 5.33, and 5.34 show the intercepts and coefficients calculated.

$$PDD_{S2A} = -8.11 + 0.25V \tag{5.32}$$

$$PDD_{S2B} = 24.11 - 0.72V \tag{5.33}$$

$$PDD_{S2C} = 4.53 - 0.14V \tag{5.34}$$

The uncertainty analysis shown in Table 5.16 exhibits the mean value to be 0.000 due to the alignment implemented during the pre-processing of the data. The range, the standard deviation, and the uncertainty are lower in the predicted values for all of the sides, which indicates that the voltage sensor cannot account for all of the deviations in the scanning. In the comparison between the laser data and the predicted SOD, the mean squared error and the root-mean-squared deviation are higher for side B. The difference suggests that there are significant deviations not detected by the voltage.

Table 5.16: Uncertainty analysis for the validation in the STML S2.

S2	Side A		Side B		Side C	
	PDD	*PDD Pred*	*PDD*	*PDD Pred*	*PDD*	*PDD Pred*
Mean $[mm]$	0.000	0.000	0.010	0.010	0.000	0.000
Range $[mm]$	1.615	0.861	3.893	1.599	2.771	0.394
SD $[mm]$	0.529	0.211	0.941	0.385	0.574	0.108
Uncertainty $[\mu m]$	105	42	184	75	112	21
MSE $[mm^2]$	0.226		0.709		0.305	
RMSD $[\mu m]$	475		841		552	

Figure 5.55 shows the deviation and predicted deviation on each side. Significant variations at the bottom are due to the initial perturbations in the first layers of the

printing process. Although the part starts to stabilize, the adjustments in the torch provoke further deviations. The deposition of material, such as residual powder or spatter, after the travel of the plasma arc, triggers deviations in the form of different surface finishes, which are hard to identify by the in-situ voltage sensor.
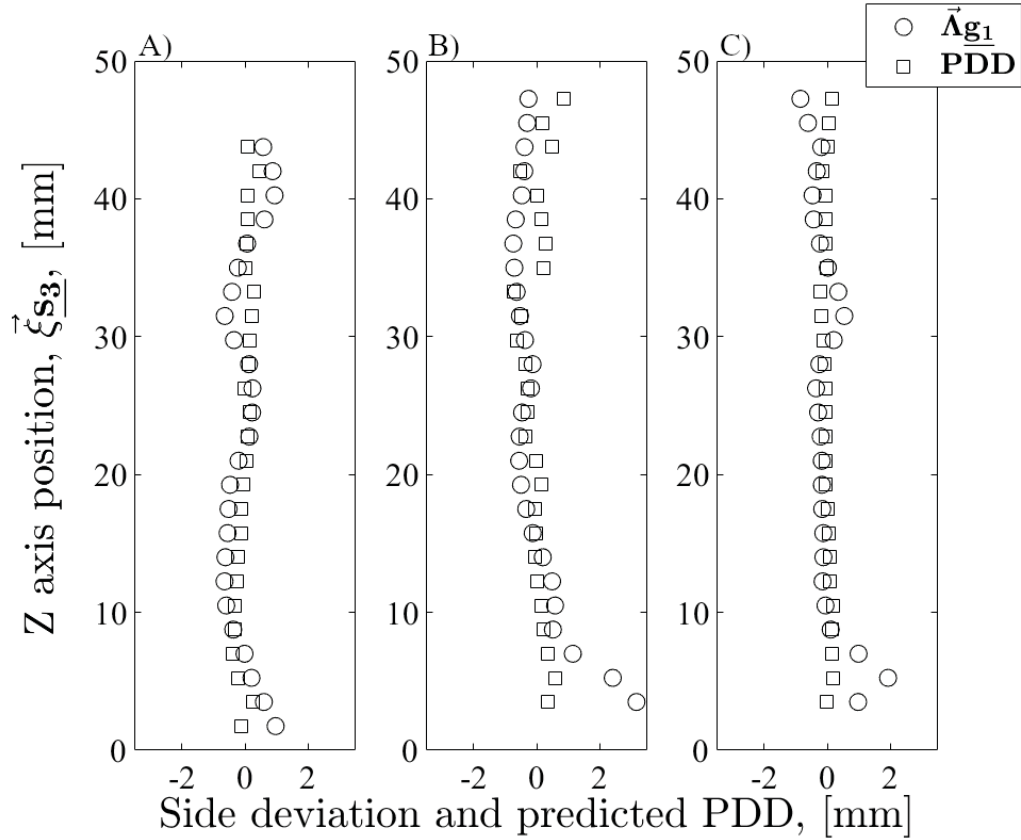
Figure 5.55: Comparision of the laser PDD and predicted PDD for the sides in sample STML S2.

Single-track multiple-layer S4 validation

The sample STML S4 is shown in Figure 5.56. Side A displays a different surface finish compared to sides B and C. The addition of spatter in the surface is due to the lack of deposition in the layer. Although the process generates enough heat to build a layer, there is not enough heat in subsequent layers to allow coalescence of powder. The lack of energy in the previous layers leads to powder attachment in the form

of spatter. Sides A and B exhibit a significant deviation at 3/4 of the total height, which is notable with spatter on sides B and C.
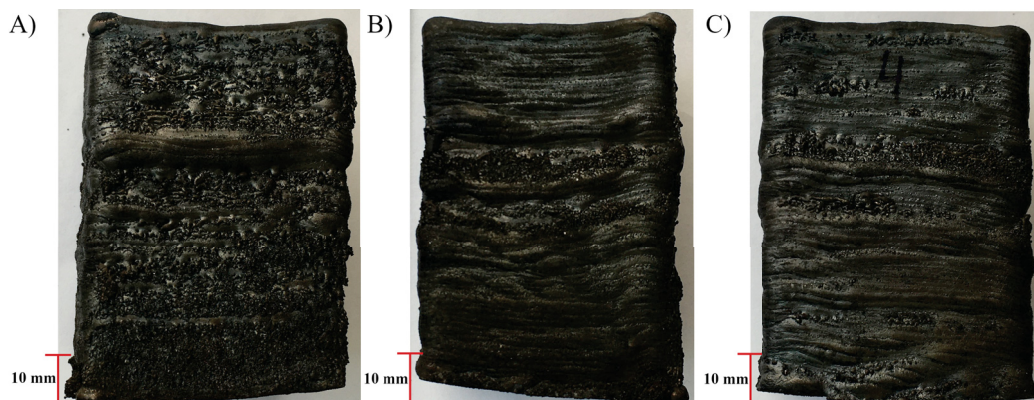
Figure 5.56: Sides of the STML sample S4. Side A shows more spatter compare to the other sides.

The voltage map for side A demonstrates higher voltage values than on the other sides [Fig. 5.57]. The voltage value is an indicator of the nozzle distance. If the nozzle distance is elevated, the heat input is decreased, causing the spattering effect observed and described previously. At z=30 mm, there is an increment in the voltage seen on the three sides. A manual lift of the torch caused the increment in the voltage. The perturbation generates PDDs observable on the sides.

The sides from the STML S4 were scanned using the laser profilometer. The data from the deviation at the mid-section was gathered and processed to align it perpendicular to the deposition. From the voltage data collected during the printing process, the mid-section of the layers in the sides was selected. The processed information is employed to build the linear regressions to predict the PDD in the sides. Equations 5.35, 5.36, and 5.37 present the obtained intercepts and coefficients.

$$PDD_{S4A} = 7.13 - 0.20V \qquad (5.35)$$
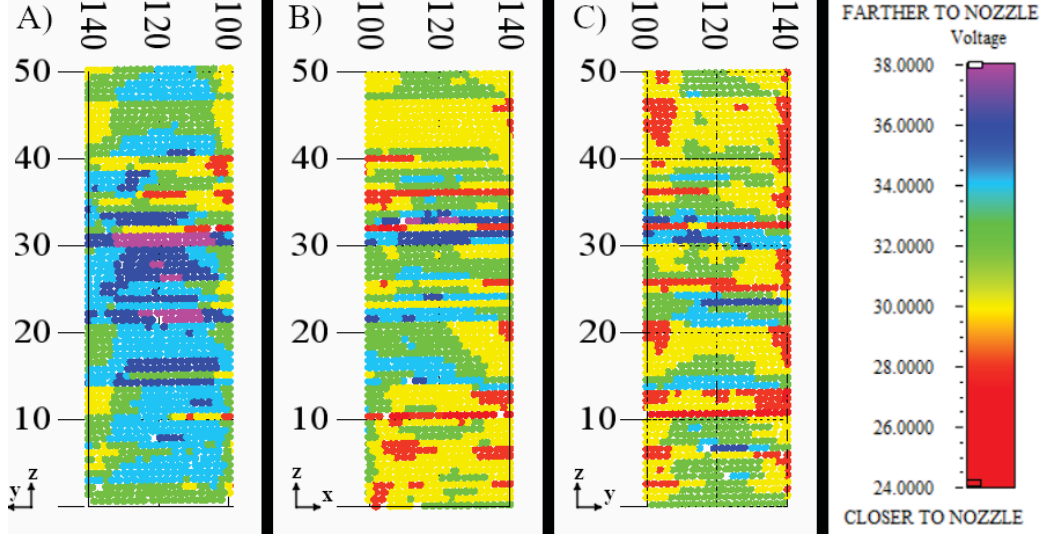
Figure 5.57: Voltage measurement for the STML S4 sides. The voltage in side A is higher than in other sides indicating a higher nozzle distance, hence less heat input.

$$PDD_{S4B} = 1.00 - 0.03V \qquad (5.36)$$

$$PDD_{S4C} = 1.10 - 0.03V \qquad (5.37)$$

The uncertainty analysis presented in Table 5.17 demonstrates the alignment of the mean values perpendicular to the building plate. The range on side A is higher than on the other sides due to the spattering. The standard deviation shows lower predicted values, indicating that the voltage sensor is not detecting some deviations. The uncertainty values are low, given the low deviations presented in all of the sides. Finally, the MSE and RMSD demonstrate that side B has more characteristics not detected by the sensor than the other sides, presenting a better PDD prediction.

The predictions for sides A and C envision an excellent measurement with a root-mean-squared deviation of 273 μm and 277 μm, respectably. Although the RMSD

Table 5.17: Uncertainty analysis for the validation in the STML S4.

S4	Side A		Side B		Side C	
	PDD	*PDD Pred*	*PDD*	*PDD Pred*	*PDD*	*PDD Pred*
Mean [mm]	-0.007	-0.007	-0.020	-0.020	-0.019	-0.019
Range [mm]	1.527	1.239	1.466	0.294	1.064	0.240
SD [mm]	0.423	0.319	0.440	0.055	0.238	0.058
Uncertainty [μm]	80	60	83	10	45	10
MSE [mm^2]	0.074		0.184		0.051	
RMSD [μm]	273		428		277	

in the prediction of the PDD on side B is 156 μm higher than on other sides, it is acceptable. There are critical deviations at z=8 mm, z=25 mm, and z=41 mm on side B not detected by the voltage sensor [Fig. 5.58].

Single-track multiple-layer S5 validation

Figure 5.59 exhibits the sides for the sample STML S5. Side A presents spattering in the surface finish. The other two sides display an even deposition beginning from z=20 mm until the top. Some instabilities are shown in the three sides at the beginning of the deposition and an important deviation at z=13 mm.

The voltage map displays behaviour consistent with the deviations presented on the sides [Fig. 5.60]. Side A displays a higher voltage compared to the other sides. This behaviour is related to an increase in spattering due to a reduction in the heat input. The stability in the upper region of sides B and C is denoted by a steady voltage after z=20 mm. In z=13 mm, the voltage increases because of a manual adjustment of the torch position. In the lower-left region of side B, a lower voltage section is linked to initial instabilities in the printed part. In that region, less powder was deposited, generating the deviations at the initial layers of the printing.
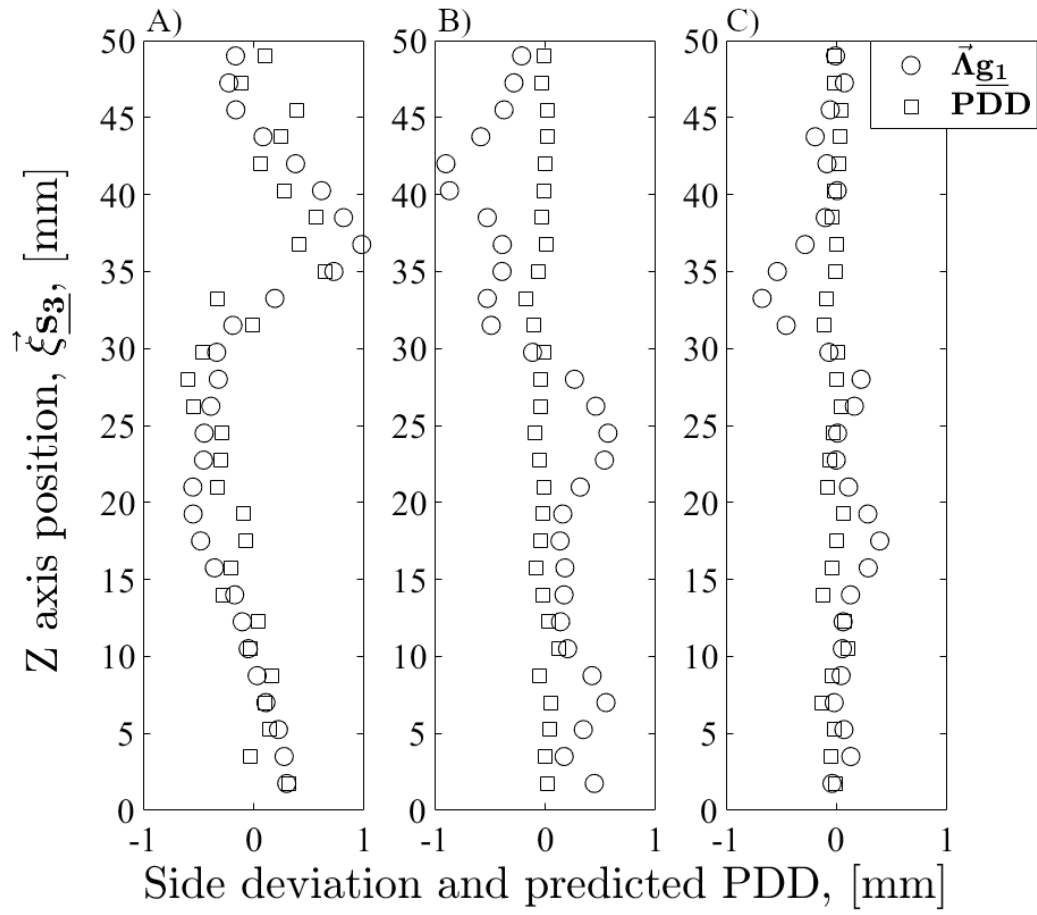
Figure 5.58: Comparison of the laser PDD and predicted PDD for the sides in sample STML S4.
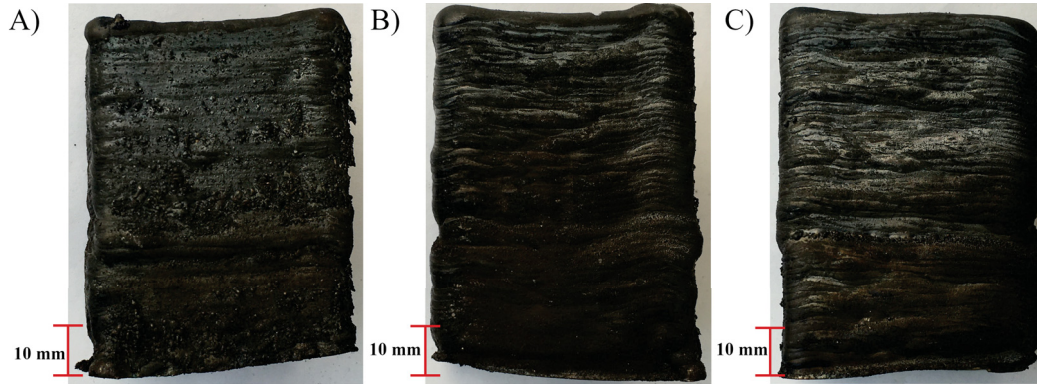
Figure 5.59: Sides of the STML sample S5. There is an even deposition shown in sides B and C beginning from Z=20 mm and important deviations in the lower section.
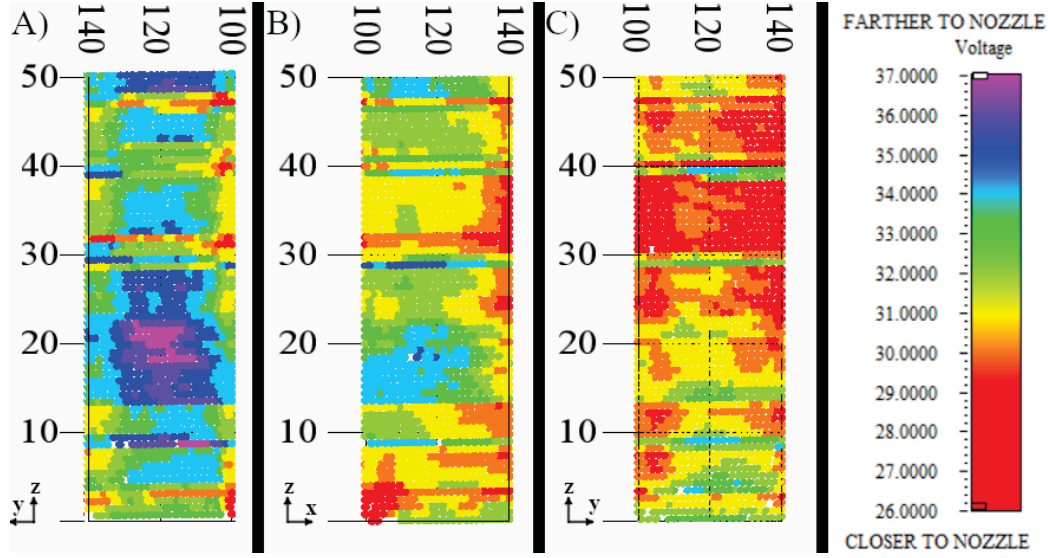
Figure 5.60: Voltage measurement for the STML S5 sides.

The sides of the STML S5 sample were laser scanned to relate the voltage to the perpendicular-to-deposition deviations. The deviations detected at the mid-sections and the voltage measured in the same location were employed to develop the linear regressions shown in Equations 5.38, 5.39, and 5.40.

$$PDD_{S5A} = -1.75 + 0.05V \tag{5.38}$$

$$PDD_{S5B} = -3.49 + 0.11V \tag{5.39}$$

$$PDD_{S5C} = -4.50 + 0.14V \tag{5.40}$$

Table 5.18 shows the uncertainty analysis. The mean values are aligned perpendicular to the deposition. The ranges, the standard deviations and the uncertainty in the predicted PPD are between 50% and 80%lower than the laser scanner. These differences indicate that there are fluctuations that are not detected by the voltage sensor. The comparison between the prediction and laser scanner data shows a mean

squared error of around 0.169 mm^2 and an RMSD of 410 μm, which means that the predicted deviation is within $\pm$ 0.4 mm.

Table 5.18: Uncertainty analysis for the validation in the STML S5.

S5	Side A		Side B		Side C	
	PDD	*PDD Pred*	*PDD*	*PDD Pred*	*PDD*	*PDD Pred*
Mean $[mm]$	-0.021	-0.021	-0.042	-0.042	0.054	0.054
Range $[mm]$	1.416	0.302	1.534	0.427	1.554	0.747
SD $[mm]$	0.420	0.084	0.436	0.123	0.460	0.173
Uncertainty $[\mu m]$	79	15	83	23	86	32
MSE $[mm^2]$	0.163		0.168		0.174	
RMSD $[\mu m]$	403		410		417	

Figure 5.61 displays the differences between the predicted and laser values for the PDD on each side. In the graph for side A, the deviations presented in z=0 mm, z=13 mm, z=20 mm, and z=45 mm are not detected by the in-situ sensor. On sides B and C, some of the deviations are detected, but with a reduced prediction. Although the voltage sensor can detect deviations produced during the travel of the plasma arc in the spot, deviations caused by heat accumulation after the movement of the torch conducted into previous layers are hard to detect. Efficient heat management through heat monitoring and closed-loop controls could prevent heat distortions and allow the in-situ voltage sensor to detect deviation on the spot in real-time.
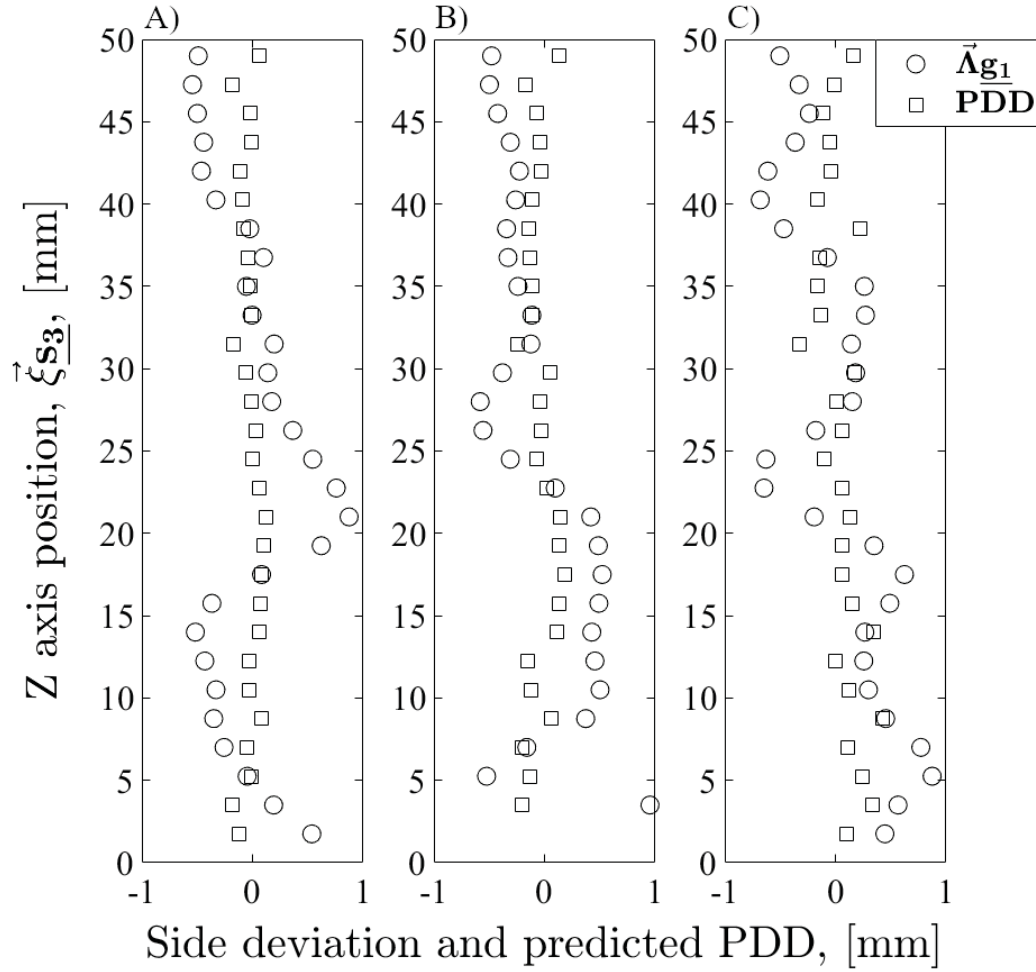
Figure 5.61: Comparison of the laser PDD and predicted PDD for the sides in sample STML S5.

5.5 Conclusions

The development of control strategies to improve the quality of metal additive manufacturing is a challenge currently under development. AM systems need to meet particular requirements concerning in-situ sensing and monitoring to achieve that goal. This chapter proposed the collection of data acquired in different domains to build reliable information about the process.

By integrating different domains that collect data through all the AM processes, it is possible to link them to better understand the process. Process parameters have an impact on the measurements of some variables. With the analysis of the collected data, it is possible to predict specific variables, such as the voltage. The prediction is useful to fine-tune a variable beforehand through the manipulation of process parameters.

The results showed a relationship between voltage and the stand-off-distance of the nozzle. The in-situ monitoring of the SOD provides relevant information to improve the material deposition. The bead height observation through broad values of SODs contributes to understanding the range in which the powder stream provides a better deposit of material.

In the particular case of an PTA-AM system, the employment of an electrical signal such as the voltage in the plasma arc is a novel way of in-situ monitoring. The capabilities and limitations of detecting stand-off-distance, bead height deposition, and perpendicular-to-deposition deviations contribute to deepening the knowledge of the printing process. The sensing and monitoring collection presented in this work is the foundation towards the establishment of control and machine learning techniques for plasma DED additive manufacturing.

Chapter 6

Conclusion, limitations, & future work

6.1 Conclusion

The adoption of new technology for the AM industry is a need that is currently expanding to include the development of systems to print new materials for new purposes, which creates new challenges to be solved. The research presented in this thesis proposes a solution to some of those challenges:

- The design methodology for the creation of new AM technology provides a framework for machine design.

- The validation and characterization of bead depositions are essential to understand the deposited materials' behaviour.

- The capacity to quantitatively evaluate the performance of the physical phenomena in 3D printing through in-situ monitoring.

The development of methodologies for design in AM speeds up the transition from concept to product. The implementation of integrated function modelling allows for a better understanding and integration between the different design layers. For the use case views, its application provides versatility in the methodology, which can be

harnessed with multiple functionalities. An iterative review of the actors and processes supplies the methodology with tools to increase the system's complexity and enhance it from the initial proposal.

The demand for printing advanced materials for the oil & gas industry leads to developing an additive manufacturing solution that employs a plasma transferred arc. This direct energy deposition system delivers enough heat input to support the adoption of a wide range of materials. The use of different feedstock for layer-by-layer deposition facilitates mechanical properties such as strength, toughness, hardness, abrasion, and corrosion resistance in printed elements. This work shows that the printing of metal matrix composites of nickel alloy with tungsten carbides is possible and satisfies the heavy-duty industry compared to current achievements in metal cladding.

The improvement of the bead through recommended process parameters, such as current, linear speed, powder flow rate, nozzle angle, and powder, shield, and center gases, generates better quality in printing parts. When using metal matrix composites, the particles' homogeneity must remain consistent through all the deposition. A methodology such as Taguchi's DOE leads to overlooking the performance of the process parameters and the adjustments required to meet particular goals. There are essential vital factors, such as current, powder flow rate, table speed, and powder gas, strengthening the printing process producing better heat management and a better bead quality. The bead characterization methodology presented in the second version of the PTA system in Chapter 4 validates the influence of process parameters in the bead geometry and how the intended goals are measurable through signal-to-noise ratios.

Finally, the development of control strategies to enhance the quality of metal additive manufacturing components is a current challenge in the AM industry. Better and new sensors need to comply with the harsh environments near the bead deposition before controlling the systems in a real-time manner. The intense heat, the powder spattering, and the gas flow dynamics under the torch limit the measuring devices to a significant adverse physical challenge. The research presented herein proposes integrating in-situ monitoring sensors to acquire information from the time, spatial, electrical, thermal, and geometrical domains. Additionally, this work also explores the use of alternative measurements to detect, in a novel way, geometrical characteristics of the bead's deposition.

6.2 Limitations

This section presents some limitations considering the experience collected in the development of this work:

- The current status of the PTA-AM system has a central computer with surrounding peripherals acquiring the data. The data collection is not deterministic, which produces some delays in data acquisition. The central computer and the peripherals have to be replaced by real-time targets to improve the system for a deterministic performance. Better targets will boost data collection and synchronization.

- The powder transportation phenomenon is complex and material dependent. The work presented in this thesis deals with a particular metal matrix composite, but other materials require a better understanding of the event. More research is needed to synchronize the powder delivery from the hopper to the

torch when the arc is turned on to produce consistent results with other materials.

- The printing process is currently a continuous deposition throughout the printing. To achieve better heat management, hence, better printing quality, a dwell time between the layers is recommended. In this layer inter-passing, the challenge is to synchronize the powder transportation phenomenon with the layer end. The positioning device's position and speed play a fundamental role in the layer's inter-passing mechanism. A buffer of future positions is required to foresee a layer end, and act accordingly.

- The nozzle design of the current torch has two powder ports. The bead deposition is dependant on the orientation of the ports and the travel of deposition. There are some perturbations associated with the nozzle's powder port orientation. Specific changes in process parameters need to be considered to compensate for these defects. Another alternative is to redesign the PTA torch taking into consideration these limitations.

6.3   Future Work

In consideration of the above-mentioned limitations for plasma transferred arc additive manufacturing, the following research directions can be pursued in future work:

- The implementation of modelling techniques to simulate thermal stresses, distortion, and warping could supply a visualization of the system and its boundary conditions. This future work could optimize the allocation of physical resources by replacing them with computational resources.

- The design and application of heat instruments such as heat sinks or airflow sys-

tems could generate a mean to more quickly dissipate the heat in the substrate and supply efficient heat management throughout the printing process.

- The work presented in this thesis is preliminary to the development of control and machine learning techniques. With the data acquired by the sensors deployed, future work could include the integration of control strategies for the deposition geometry and powder deposition.

- Further development for the PTA-AM could include the characterization and optimization of different printing materials such as satellite, 31655, CWI UK-Sandvikor, or Super12Cr. Each one of those printing materials could improve specific mechanical properties.

- The development of functionally graded materials with the PTA-AM system is proposed for future work. There are compelling improvements, such as the powder flow synchronization, to be adapted in the different design layers to extend the current capabilities into printing steel to Ni-WC.

- In Chapter 5, the efficiency and limitation of the sensors are described. The regressions proposed were all linear regressions. The study of higher rank regressions presents an opportunity to evaluate the sensors' results with other operational ranges.

- Single-track single-layer beads and single-track multiple-layer beads were discussed in the current work. Research in the context of multiple-track single-layer and multiple-track multiple-layers is an intriguing future direction for the PTA-AM system.

Although this future work is promising, future research directions are not limited to the scope defined herein. The PTA-AM system is broad enough to extend the research in a variety of directions on a variety of projects.

Bibliography

[1] Business Dictionary. *Manufacturing definition*. 2020. URL: http://www.businessdictionary. com/definition/manufacturing.html.

[2] D. K. Dwivedi. *Welding Engineering Lecture 1: Introduction*. 2013. URL: https: //nptel.ac.in/courses/112107090/#.

[3] Andreas Gebhardt. *Understanding Additive Manufacturing*. Munich, Germany, 2012.

[4] Frost and Sullivan's Global 360 Research Team. *Global Additive Manufacturing Market 2023 - Forecast*. Tech. rep. 2016. URL: http://namic.sg/wp-content/ uploads/2018/04/global-additive-manufacturing-market_1.pdf.

[5] The Information and Communications Technology Council. "Additive Manufacturing in Canada: The impeding talent paradigm". In: (July 2017). URL: https://www.ictc-ctic.ca/wp-content/uploads/2017/07/ICTC-Additive-Manufacturing-ENG-Final.pdf.

[6] Statistics Canada. *Gross domestic product (GDP) at basic prices, by industry, monthly (x 1,000,000)*. Tech. rep. 2019. URL: https://www150.statcan.gc.ca/ t1/tbl1/en/tv.action?pid=3610043401.

[7] Statistics Canada. *Survey of Advanced Technology (SAT)*. Tech. rep. 2014. URL: http://www23.statcan.gc.ca/imdb/p2SV.pl?Function=getSurvey%5C& SDDS=4223.

[8] Jerome Kaspar et al. "Integrated Product, Production and Material Definition for Conventional versus Generative Manufacturing Technologies". In: *Procedia CIRP* 70 (2018), pp. 180–185. DOI: 10.1016/j.procir.2018.03.140. URL: https: //doi.org/10.1016/j.procir.2018.03.140%20https://linkinghub.elsevier.com/ retrieve/pii/S221282711830297X.

[9] William E. Frazier. "Metal additive manufacturing: A review". In: *Journal of Materials Engineering and Performance* 23.6 (2014), pp. 1917–1928. DOI: 10.1007/s11665-014-0958-z.

[10] TANDELTA Oil Condition Monitoring. *Reducing Oilfield Equipment Downtime with Data-driven Maintenance*. 2019. URL: https://www.tandeltasystems. com/reducing-oilfield-equipment-downtime-with-data-driven-maintenance/.

[11]   ASTM International. *F3187-16 Standard Guide for Directed Energy Deposition of Metals*. Tech. rep. F3187-16. West Conshohocken, PA: ASTM, 2016. DOI: 10.1520/F3187-16.

[12]   Peter Marsh. "Ready to print the future". In: *Financial Times* (July 2012). URL: http://www.ft.com/cms/s/0/da2ccaa8-c5f5-11e1-b57e-00144feabdc0. html%7B%5C#%7Daxzz3O9hKCVgg.

[13]   Tim Berners-Lee. *Weaving the Web: The Original Design and Ultimate Destiny of the World Wide Web*. Harper, 1999.

[14]   Gartner. *Hype Cycle for Emerging Technologies, 2007*. 2007. URL: https:// www.gartner.com/en/documents/509710/hype-cycle-for-emerging-technologies-2007.

[15]   T. Kellner. "Mind Meld: How GE and a 3D-Printing visionary joined forces". In: *GE Reports* (July 2017).

[16]   Steinar Killi. *Additive Manufacturing Design, Methods, and Processes*. USA: Pan Stanford Publishing, 2017. ISBN: 978-1-315-19658-9.

[17]   Ralph Baker. *Method of making decorative articles*. Patent US1533300A. Apr. 1925.

[18]   H. Ingham. *Flame spraying employing laser heating*. Patent US3310423A. 1967.

[19]   Ujiie Akira. *Method of and apparatus for constructing substantially circular cross section vessel by welding*. Patent US3558846A. Jan. 1971.

[20]   Ujiie Akira. *Method of constructing substantially circular cross-section vessel by welding*. Patent US3665143A. 1972.

[21]   P.A. Ciraud. *A method and apparatus for manufacturing objects made of any arbitrary material meltable*. DE2263777A1. 1973.

[22]   David L Dl Bourell et al. "A brief history of additive manufacturing and the 2009 roadmap for additive manufacturing: looking back and looking ahead". In: *RapidTech 2009: US-TURKEY Workshop on Rapid Technologies* 2 (2009), pp. 2005–2005. URL: http://iweb.tntech.edu/rrpl/rapidtech2009/bourell.pdf.

[23]   A.Thyssen and H. Th. Brandi. *Method of making large structural one-piece parts of metal, particularly one-piece shafts*. Patent US3985995A. 1976.

[24]   K. Kussmaul, F.W. Schoch, and H. Luckow. "High Quality Large Components "Shape Welded" by a SAW Process". In: *Welding Journal* (1983), pp. 17–24.

[25]   N. Greavu et al. *Welding process using granular or powder filler delivered on open-channel strip*. Patent US3819901A. 1974.

[26]   C.M. Banas et al. *Skin melting*. Patent US4122240A. 1978.

[27]   E.D. Ditto. *Method of alloying and forming a valve seat*. Patent US4059876A. 1977.

[28]   C.O. Brown and B.H. Kear E.M. Breinan. *Method for fabricating articles by sequential layer deposition*. Patent US4323756A. 1982.

[29] R.F. Housholder. *Molding process.* US4247508A. 1981.

[30] J. Koch and J. Mazumder. *Apparatus and methods for monitoring and controlling multi-layer laser cladding.* Patent US6122564A. 2000.

[31] J. Mazumder and J.K. Kelly. *Closed-loop, rapid manufacturing of three-dimensional components using direct metal deposition.* Patent US6925346B1. 2005.

[32] J. Mazumder and F.A. DiPietro. *Method of fabricating composite tooling using closed-loop direct-metal deposition.* Patent US7139633B2. 2006.

[33] J. Mazumder et al. *Direct metal deposition apparatus utilizing rapid-response diode laser source.* Patent US7765022B2. 2010.

[34] J. Mazumder, J. Ni, and A. Shih. *High-speed, ultra precision manufacturing station that combines direct metal deposition and edm.* Patent US8629368B2. 2014.

[35] T.W. Skszek. *Fabrication of laminate tooling using closed-loop direct metal deposition.* Application US20020165634A1. 2002.

[36] Jyoti Mazumder, Dwight Morgan, and Timothy W. Skszek. "U.S. Application No.20020142107". (United States). 2002.

[37] Jyoti Mazumder. "U.S. Application No.20040020625". (United States). 2004.

[38] Jyoti Mazumder and Frank A. DiPietro. "U.S. Application No.20050038551". (United States). 2005.

[39] Jyoti Mazumder, Jun Ni, and Albert Shih. "U.S. Application No.20070205184". (United States). 2007.

[40] Lijun Song and Jyoti Mazumder. "U.S. Application No.20080296270A". (United States). 2008.

[41] Ehsan Toyserkani, Amir Khajepour, and Stephen F. Corbin. "U.S. Patent No.7043330". (United States). 2006.

[42] Ehsan Toyserkani, Amir Khajepour, and Stephen F. Corbin. "Canadian Patent No.2504368". (Canada). 2012.

[43] Ehsan Toyserkani, Amir Khajepour, and Stephen F. Corbin. "U.S. Application No.20040133298A". (United States). 2004.

[44] Ehsan Toyserkani, Amir Khajepour, and Stephen F. Corbin. "World Patent No.2004039531". (Geneva, Switzerland). 2004.

[45] Jinguo Ge et al. "Location-related thermal history, microstructure, and mechanical properties of arc additively manufactured 2Cr13 steel using cold metal transfer welding". In: *Materials Science and Engineering A* 715.August 2017 (2018), pp. 144–153. DOI: 10.1016/j.msea.2017.12.076.

[46] Yongzhe Li et al. "Enhanced beads overlapping model for wire and arc additive manufacturing of multi-layer multi-bead metallic parts". In: *Journal of Materials Processing Technology* 252.December 2016 (2018), pp. 838–848. ISSN: 09240136. DOI: 10.1016/j.jmatprotec.2017.10.017. URL: http://dx.doi.org/10.1016/j.jmatprotec.2017.10.017.

[47] Chen Zhang et al. "Wire arc additive manufacturing of Al-6Mg alloy using variable polarity cold metal transfer arc as power source". In: *Materials Science and Engineering: A* 711 (2018), pp. 415–423. DOI: 10.1016/j.msea.2017.11.084.

[48] Jun Xiong et al. "Heat propagation of circular thin-walled parts fabricated in additive manufacturing using gas metal arc welding". In: *Journal of Materials Processing Technology* 251 (2018), pp. 12–19. DOI: 10.1016/j.jmatprotec.2017.08.007.

[49] Ali Gökhan Demir. "Micro laser metal wire deposition for additive manufacturing of thin-walled structures". In: *Optics and Lasers in Engineering* 100.January 2018 (2018), pp. 9–17. DOI: 10.1016/j.optlaseng.2017.07.003.

[50] Suyog Jhavar, N. K. Jain, and C. P. Paul. "Development of micro-plasma transferred arc (μ-PTA) wire deposition process for additive layer manufacturing applications". In: *Journal of Materials Processing Technology* 214.5 (2014), pp. 1102–1110. DOI: 10.1016/j.jmatprotec.2013.12.016.

[51] E Herderick. "Additive manufacturing of metals: A review". In: *Materials Science & Technology Conference and Exhibition 2011*. Vol. 1. Columbus, Ohio, USA: Curran Associates, 2011, pp. 1413–1425.

[52] J.G. Mercado Rojas et al. "Design modeling for additive manufacturing in the case study of a systematic methodology applied to plasma transferred arc additive manufacturing". In: *Procedia CIRP* (2019). ISSN: 2212-8271. DOI: 10.1016/j.procir.2019.04.198.

[53] Elnaz Asadollahi-Yazdi, Julien Gardan, and Pascal Lafon. "Integrated Design for Additive Manufacturing Based on Skin-Skeleton Approach". In: *Procedia CIRP* 60.2212 (2017), pp. 217–222. DOI: 10.1016/j.procir.2017.02.007. arXiv: arXiv:1011.1669v3. URL: http://dx.doi.org/10.1016/j.procir.2017.02.007%20https://linkinghub.elsevier.com/retrieve/pii/S2212827117300720.

[54] Uzair Khaleeq uz Zaman et al. "Integrated design-oriented framework for Resource Selection in Additive Manufacturing". In: *Procedia CIRP* 70 (2018), pp. 96–101. ISSN: 22128271. DOI: 10.1016/j.procir.2018.02.039. URL: https://doi.org/10.1016/j.procir.2018.02.039%20https://linkinghub.elsevier.com/retrieve/pii/S2212827118304025.

[55] Felician Campean and Unal Yildirim. "Enhanced Sequence Diagram for Function Modelling of Complex Systems". In: *Procedia CIRP* 60 (2017), pp. 273–278. ISSN: 22128271. DOI: 10.1016/j.procir.2017.01.053. URL: http://dx.doi.org/10.1016/j.procir.2017.01.053%20https://linkinghub.elsevier.com/retrieve/pii/S2212827117300549.

[56] Boris Eisenbart et al. "Integrating Different Functional Modeling Perspectives". In: *International Conference on Research into Design*. Madras, Chennai: ICoRD 2013, 2013.

[57] B. Eisenbart, K. Gericke, and L. Blessing. "Application of the ifm framework for modelling and analysing system functionality". In: *Proceedings of International Design Conference, DESIGN* 2014-Janua.Section 4 (2014), pp. 153–162. ISSN: 18479073.

[58] B. Eisenbart, Y. I. Khan, and A. J. Qureshi. "Integrated product modelling through IFM-CPM/PDD". In: *Proceedings of International Design Conference, DESIGN*. Vol. DS 84. May. 2016, pp. 183–192.

[59] Edgar C. Tamayo et al. "Design automation of control panels for automated modular construction machines". In: *Procedia CIRP* 70 (2018), pp. 404–409. ISSN: 22128271. DOI: 10.1016/j.procir.2018.02.004. URL: https://doi.org/10.1016/j.procir.2018.02.004%20https://linkinghub.elsevier.com/retrieve/pii/S221282711830012X.

[60] Nam Pyo Suh. "Axiomatic Design Theory for Systems". In: *Research in Engineering Design* 10.4 (Dec. 1998), pp. 189–209. ISSN: 0934-9839. DOI: 10.1007/s001639870001. arXiv: 1712.01541. URL: http://link.springer.com/10.1007/s001639870001.

[61] B. Berenbach et al. *Software & Systems Requirements Engineering: In Practice*. New York, USA, 2012.

[62] N. Suh. *Complexity: theory and application*. New York, USA, 2005.

[63] S.D. Eppinger and Browning T.R. *Design Structure Matrix Methods and Applications*. London, England, 2012.

[64] Ali A. Yassine. "An introduction to modeling and analyzing complex product development processes using the design structure matrix (DSM) method". In: *Quaderni di Manage. (Italian Manage. Rev.)* 9 (2004), pp. 71–88.

[65] Edgar C. Tamayo et al. "Conceptual design of an automated steel wall framing assembly using axiomatic design and integrated function model". In: *Construction Robotics* 3.1-4 (Dec. 2019), pp. 83–101. ISSN: 2509-811X. DOI: 10.1007/s41693-019-00022-8. URL: https://doi.org/10.1007/s41693-019-00022-8%20http://link.springer.com/10.1007/s41693-019-00022-8.

[66] J.G. Mercado Rojas et al. "Plasma transferred arc additive manufacturing of Nickel metal matrix composites". In: *Manufacturing Letters* (2018). ISSN: 22138463. DOI: 10.1016/j.mfglet.2018.10.001.

[67] J.G. Mercado Rojas et al. "Preliminary geometrical and microstructural characterization of WC-reinforced NiCrBSi matrix composites fabricated by plasma transferred arc additive manufacturing through Taguchi-based experimentation". In: *The International Journal of Advanced Manufacturing Technology* (2021). DOI: 10.1007/s00170-020-06388-2.

[68] C. S. Wu et al. "Plasma arc welding: Process, sensing, control and modeling". In: *Journal of Manufacturing Processes* 16.1 (2014), pp. 74–85. ISSN: 15266125. DOI: 10.1016/j.jmapro.2013.06.004.

[69] Tonya Wolfe. "Homogeneity of Metal Matrix Composites Deposited by Plasma Transferred Arc". PhD thesis. Department of Chemical and Materials Engineering, University of Alberta, 2010, p. 364. DOI: https://doi.org/10.7939/R3K64Q. URL: https://doi.org/10.7939/R3K64Q.

[70] J.L Shohet. *Encyclopedia of Plasma Technology Volume I*. Boca Raton, USA, 2017.

[71] N. Venkatramani. "Industrial plasma torches and applications". In: *Current Science* 83.3 (2002), pp. 254–262. ISSN: 00113891. URL: http://www.jstor.org/stable/24106883.

[72] S. Kalpakjian and S.R. Schmid. *Manufacturing Engineering and Technology*. Pearson, 2001, pp. 789–790. ISBN: 978-0-13-522860-9.

[73] E.B Hackett et al. "U.S. Application No.5760363A". (United States). 1998.

[74] Wurikaixi Aiyiti et al. "Investigation of the overlapping parameters of MPAW-based rapid prototyping". In: *Rapid Prototyping Journal* 12.3 (2006), pp. 165–172. ISSN: 13552546. DOI: 10.1108/13552540610670744.

[75] K. Yu Nagulin et al. "Optical diagnostics and optimization of the gas-powder flow in the nozzles for laser cladding". In: *Optics and Laser Technology* 108 (2018), pp. 310–320. ISSN: 00303992. DOI: 10.1016/j.optlastec.2018.07.001. URL: https://doi.org/10.1016/j.optlastec.2018.07.001.

[76] Simone Zanzarin. "Laser cladding with metallic powder". PhD thesis. Department of Materials Science and Engineering, University of Trento, 2015, p. 133.

[77] Srdja Zekovic, Rajeev Dwivedi, and Radovan Kovacevic. "Numerical simulation and experimental investigation of gas-powder flow from radially symmetrical nozzles in laser-based direct metal deposition". In: *International Journal of Machine Tools and Manufacture* 47.1 (2007), pp. 112–123. ISSN: 08906955. DOI: 10.1016/j.ijmachtools.2006.02.004.

[78] Z. H. Rao, S. M. Liao, and H. L. Tsai. "Effects of shielding gas compositions on arc plasma and metal transfer in gas metal arc welding". In: *Journal of Applied Physics* 107.4 (Feb. 2010), p. 044902. ISSN: 0021-8979. DOI: 10.1063/1.3291121. URL: http://aip.scitation.org/doi/10.1063/1.3291121.

[79] Adrita Dass and Atieh Moridi. "State of the Art in Directed Energy Deposition: From Additive Manufacturing to Materials Design". In: *Coatings* 9.7 (June 2019), p. 418. ISSN: 2079-6412. DOI: 10.3390/coatings9070418. URL: https://www.mdpi.com/2079-6412/9/7/418.

[80] T. Artaza et al. "Design and integration of WAAM technology and in situ monitoring system in a gantry machine". In: *Procedia Manufacturing* 13 (2017), pp. 778–785. ISSN: 23519789. DOI: 10.1016/j.promfg.2017.09.184. URL: https://doi.org/10.1016/j.promfg.2017.09.184%20https://linkinghub.elsevier.com/retrieve/pii/S2351978917308223.

[81] Scott M. Thompson et al. "An overview of Direct Laser Deposition for additive manufacturing; Part I: Transport phenomena, modeling and diagnostics". In: *Additive Manufacturing* 8 (2015), pp. 36–62. ISSN: 22148604. DOI: 10.1016/j.addma.2015.07.001. URL: http://dx.doi.org/10.1016/j.addma.2015.07.001.

[82] H Wang et al. "Microplasma powder deposition as a new solid freeform fabrication process". In: *Proceedings of the Institution of Mechanical Engineers, Part B: Journal of Engineering Manufacture* 217.12 (Dec. 2003), pp. 1641–1650. ISSN: 0954-4054. DOI: 10.1243/095440503772680578. URL: http://journals.sagepub.com/doi/10.1243/095440503772680578.

[83] Douglas C. Montgomery. *Design and Analysis of Experiments*. Wiley, 2019. ISBN: 978-1-119-49244-3.

[84] Abhay Sharma, Navneet Arora, and Bhanu K. Mishra. "A practical approach towards mathematical modeling of deposition rate during twin-wire submerged arc welding". In: *The International Journal of Advanced Manufacturing Technology* 36.5-6 (Mar. 2008), pp. 463–474. ISSN: 0268-3768. DOI: 10.1007/s00170-006-0847-1. URL: http://link.springer.com/10.1007/s00170-006-0847-1.

[85] S. C. Juang and Y. S. Tarng. "Process parameter selection for optimizing the weld pool geometry in the tungsten inert gas welding of stainless steel". In: *Journal of Materials Processing Technology* 122.1 (2002), pp. 33–37. ISSN: 09240136. DOI: 10.1016/S0924-0136(02)00021-3.

[86] Mohammad K. Alam et al. "Predictive modeling and the effect of process parameters on the hardness and bead characteristics for laser-cladded stainless steel". In: *International Journal of Advanced Manufacturing Technology* 94.1-4 (2018), pp. 397–413. ISSN: 14333015. DOI: 10.1007/s00170-017-0898-5.

[87] Navid Nazemi, Jill Urbanic, and Mohammad Alam. "Hardness and residual stress modeling of powder injection laser cladding of P420 coating on AISI 1018 substrate". In: *International Journal of Advanced Manufacturing Technology* 93.9-12 (2017), pp. 3485–3503. DOI: 10.1007/s00170-017-0760-9.

[88] Subrata Mondal, Asish Bandyopadhyay, and Pradip Kumar Pal. "Application of artificial neural network for the prediction of laser cladding process characteristics at Taguchi-based optimized condition". In: *International Journal of Advanced Manufacturing Technology* 70.9-12 (2014), pp. 2151–2158. ISSN: 02683768. DOI: 10.1007/s00170-013-5393-z.

[89] Bhaskarananda Dasgupta and Pinaky Bhadury. "Optimization of Weld Bead Parameters of Nickel Based Overlay Deposited by Plasma Transferred Arc Surfacing with Adequacy Test". In: *International Journal of Engineering Research and Applications* 4.7 (2014), pp. 201–206.

[90] J. Wilden, J. P. Bergmann, and H. Frank. "Plasma transferred arc welding—modeling and experimental optimization". In: *Journal of Thermal Spray Technology* 15.4 (2006), pp. 779–784. ISSN: 1059-9630, 1544-1016. DOI: 10.1361/105996306X146767. URL: http://link.springer.com/article/10.1361/

105996306X146767%5Cnhttp://link.springer.com/article/10.1361/105996306X146767%5Cnhttp://link.springer.com/content/pdf/10.1361/105996306X146767.pdf.

[91] Ravi Parekh, Ramesh Kumar Buddu, and R.I. Patel. "Multiphysics Simulation of Laser Cladding Process to Study the Effect of Process Parameters on Clad Geometry". In: *Procedia Technology* 23 (2016), pp. 529–536. ISSN: 22120173. DOI: 10.1016/j.protcy.2016.03.059. URL: http://linkinghub.elsevier.com/retrieve/pii/S2212017316300603.

[92] S. M. Saqib and R. J. Urbanic. "Investigation of the Transient Characteristics for Laser Cladding Beads Using 420 Stainless Steel Powder". In: *Journal of Manufacturing Science and Engineering* 139.8 (2017), p. 081009. ISSN: 1087-1357. DOI: 10.1115/1.4036488. URL: http://manufacturingscience.asmedigitalcollection.asme.org/article.aspx?doi=10.1115/1.4036488.

[93] Chigozie Obidigbo, Eric-Paul Tatman, and Joy Gockel. "Processing parameter and transient effects on melt pool geometry in additive manufacturing of Invar 36". In: *The International Journal of Advanced Manufacturing Technology* 104.5-8 (Oct. 2019), pp. 3139–3146. ISSN: 0268-3768. DOI: 10.1007/s00170-019-04229-5. URL: http://link.springer.com/10.1007/s00170-019-04229-5.

[94] Sandy Moghazi et al. "Plasma Transfer Arc Additive Manufacturing of 17-4 PH: Assessment of Defects". In: *The International Journal of Advanced Manufacturing Technology* In press (2020).

[95] J. Beuth and N. Klingbeil. "The role of process variables in laser-based direct metal solid freeform fabrication". In: *Jom* 53.9 (2001), pp. 36–39. ISSN: 10474838. DOI: 10.1007/s11837-001-0067-y. URL: http://www.scopus.com/inward/record.url?eid=2-s2.0-0035440352%5C&partnerID=tZOtx3y1.

[96] Alireza Fathi et al. "Prediction of melt pool depth and dilution in laser powder deposition". In: *Journal of Physics D: Applied Physics* 39.12 (June 2006), pp. 2613–2623. ISSN: 0022-3727. DOI: 10.1088/0022-3727/39/12/022.

[97] Huan Qi, Magdi Azer, and Prabhjot Singh. "Adaptive toolpath deposition method for laser net shape manufacturing and repair of turbine compressor airfoils". In: *International Journal of Advanced Manufacturing Technology* 48.1-4 (2010), pp. 121–131. ISSN: 02683768. DOI: 10.1007/s00170-009-2265-7.

[98] Andrea Angelastro et al. "Optimization of Ni-based WC/Co/Cr composite coatings produced by multilayer laser cladding". In: *Advances in Materials Science and Engineering* 2013 (2013). ISSN: 16878434. DOI: 10.1155/2013/615464.

[99] Tarak Amine, Joseph W. Newkirk, and Frank Liou. "An investigation of the effect of direct metal deposition parameters on the characteristics of the deposited layers". In: *Case Studies in Thermal Engineering* 3.9-12 (July 2014), pp. 21–34. ISSN: 2214157X. DOI: 10.1016/j.csite.2014.02.002. URL: http://dx.doi.org/10.1016/j.csite.2014.02.002%20http://link.springer.com/10.1007/s00170-014-5951-z%20https://linkinghub.elsevier.com/retrieve/pii/S2214157X14000070.

[100] S. Saqib, R.J. Urbanic, and K. Aggarwal. "Analysis of Laser Cladding Bead Morphology for Developing Additive Manufacturing Travel Paths". In: *Procedia CIRP* 17 (2014), pp. 824–829. DOI: 10.1016/j.procir.2014.01.098. URL: http://dx.doi.org/10.1016/j.procir.2014.01.098%20https://linkinghub.elsevier.com/retrieve/pii/S2212827114003564.

[101] J.L. Prado-Cerqueira, J.L. Diéguez, and A.M. Camacho. "Preliminary development of a Wire and Arc Additive Manufacturing system (WAAM)". In: *Procedia Manufacturing* 13 (2017), pp. 895–902. ISSN: 23519789. DOI: 10.1016/j.promfg.2017.09.154. URL: https://doi.org/10.1016/j.promfg.2017.09.154%20https://linkinghub.elsevier.com/retrieve/pii/S2351978917307916.

[102] Mariacira Liberini et al. "Selection of Optimal Process Parameters for Wire Arc Additive Manufacturing". In: *Procedia CIRP* 62 (2017), pp. 470–474. ISSN: 22128271. DOI: 10.1016/j.procir.2016.06.124. URL: http://dx.doi.org/10.1016/j.procir.2016.06.124%20https://linkinghub.elsevier.com/retrieve/pii/S2212827117301968.

[103] E. M. Ryan et al. "The influence of build parameters and wire batch on porosity of wire and arc additive manufactured aluminium alloy 2319". In: *Journal of Materials Processing Technology* 262.April (2018), pp. 577–584. ISSN: 09240136. DOI: 10.1016/j.jmatprotec.2018.07.030. URL: https://doi.org/10.1016/j.jmatprotec.2018.07.030.

[104] Mayur S. Sawant and N. K. Jain. "Investigations on additive manufacturing of Ti-6Al-4V by microplasma transferred arc powder deposition process". In: *Journal of Manufacturing Science and Engineering, Transactions of the ASME* 140.8 (2018), pp. 1–11. ISSN: 15288935. DOI: 10.1115/1.4040324.

[105] F. Martina et al. "Investigation of the benefits of plasma deposition for the additive layer manufacture of Ti-6Al-4V". In: *Journal of Materials Processing Technology* 212.6 (2012), pp. 1377–1386. ISSN: 09240136. DOI: 10.1016/j.jmatprotec.2012.02.002. URL: http://dx.doi.org/10.1016/j.jmatprotec.2012.02.002.

[106] Joy Gockel, Jack Beuth, and Karen Taminger. "Integrated control of solidification microstructure and melt pool dimensions in electron beam wire feed additive manufacturing of Ti-6Al-4V". In: *Additive Manufacturing* 1-4 (Oct. 2014), pp. 119–126. ISSN: 22148604. DOI: 10.1016/j.addma.2014.09.004. URL: https://linkinghub.elsevier.com/retrieve/pii/S2214860414000141.

[107] E Herderick. "Additive manufacturing of metals: A review". In: *Materials Science and Technology Conference and Exhibition 2011, MS and T'11* 2.176252 (2011), pp. 1413–1425. URL: http://www.scopus.com/inward/record.url?eid=2-s2.0-84856301323%7B%5C&%7DpartnerID=40%7B%5C&%7Dmd5=e02018d10b2ca37a7e2ae1773e4fcaec.

[108] Jun Xiong, Ziqiu Yin, and Weihua Zhang. "Forming appearance control of arc striking and extinguishing area in multi-layer single-pass GMAW-based additive manufacturing". In: *International Journal of Advanced Manufacturing Technology* 87.1-4 (2016), pp. 579–586. ISSN: 14333015. DOI: 10.1007/s00170-016-8543-2. URL: http://dx.doi.org/10.1007/s00170-016-8543-2.

[109] Giuseppe Venturini et al. "Feature based three axes computer aided manufacturing software for wire arc additive manufacturing dedicated to thin walled components". In: *Additive Manufacturing* 22.May (Aug. 2018), pp. 643–657. ISSN: 22148604. DOI: 10.1016/j.addma.2018.06.013. URL: https://doi.org/10.1016/j.addma.2018.06.013%20https://linkinghub.elsevier.com/retrieve/pii/S2214860418301684.

[110] Oerlikon Metco. *Material Product Data Sheet Monocrystalline Tungsten Carbide / Nickel Chromium Boron Silicon Powder for Plasma Transferred Arc (PTA)*. Tech. rep. Oerlikon Metco, 2019, pp. 1–4. URL: https://www.oerlikon.com/ecomaXL/files/metco/oerlikon_DSM-0246.0_PlasmaDur_MTC_NiCrBSi.pdf%5C&download=0.

[111] NACE. *Joint Surface Preparation Standard Near-White Metal Blast Cleaning*. Tech. rep. 21066. NACE International, 2006, pp. 1–8.

[112] ASTM. *A36-A36M19 Standard Specification for Carbon Structural Steel*. Tech. rep. ASTM, 2005, pp. 1–4.

[113] Prakash R. Apte. *Why/When is Taguchi Method Appropriate? Chapter 5: Taguchi Method SN-Ratio for Quality Characteristics approaching IDEAL value*. 2001. URL: Retrieved%20from:%20http://www.ee.iitb.ac.in/~apte/WhyTaguchiMethodTip5.ppt.

[114] T. Mukherjee et al. "Mitigation of thermal distortion during additive manufacturing". In: *Scripta Materialia* 127 (Jan. 2017), pp. 79–83. ISSN: 13596462. DOI: 10.1016/j.scriptamat.2016.09.001. URL: https://linkinghub.elsevier.com/retrieve/pii/S1359646216304195.

[115] C.R. Cunningham et al. "Invited review article: Strategies and processes for high quality wire arc additive manufacturing". In: *Additive Manufacturing* 22.June (Aug. 2018), pp. 672–686. ISSN: 22148604. DOI: 10.1016/j.addma.2018.06.020. URL: https://doi.org/10.1016/j.addma.2018.06.020%20https://linkinghub.elsevier.com/retrieve/pii/S2214860418303920.

[116] Bintao Wu et al. "Effects of heat accumulation on the arc characteristics and metal transfer behavior in Wire Arc Additive Manufacturing of Ti6Al4V". In: *Journal of Materials Processing Technology* 250.December 2016 (Dec. 2017), pp. 304–312. ISSN: 09240136. DOI: 10.1016/j.jmatprotec.2017.07.037. URL: http://dx.doi.org/10.1016/j.jmatprotec.2017.07.037%20https://linkinghub.elsevier.com/retrieve/pii/S0924013617303370.

[117] W. J. Sames et al. "The metallurgy and processing science of metal additive manufacturing". In: *International Materials Reviews* 61.5 (July 2016), pp. 315–360. ISSN: 0950-6608. DOI: 10.1080/09506608.2015.1116649. URL: http://www.tandfonline.com/doi/full/10.1080/09506608.2015.1116649.

[118] Sarah K. Everton et al. "Review of in-situ process monitoring and in-situ metrology for metal additive manufacturing". In: *Materials and Design* 95 (2016), pp. 431–445. ISSN: 18734197. DOI: 10.1016/j.matdes.2016.01.099.

[119] Jay Lee, Hung An Kao, and Shanhu Yang. "Service innovation and smart analytics for Industry 4.0 and big data environment". In: *Procedia CIRP* 16 (2014), pp. 3–8. ISSN: 22128271. DOI: 10.1016/j.procir.2014.02.001. URL: http://dx.doi.org/10.1016/j.procir.2014.02.001.

[120] Abdalla R. Nassar et al. "Sensing for directed energy deposition and powder bed fusion additive manufacturing at Penn State University". In: *Laser 3D Manufacturing III* 9738.April 2016 (2016), 97380R. ISSN: 1996756X. DOI: 10.1117/12.2217855.

[121] N. W. Klingbeil et al. "Residual stress-induced warping in direct metal solid freeform fabrication". In: *International Journal of Mechanical Sciences* 44.1 (2002), pp. 57–77. ISSN: 00207403. DOI: 10.1016/S0020-7403(01)00084-4.

[122] Andreas Lundbäck and Lars Erik Lindgren. "Modelling of metal deposition". In: *Finite Elements in Analysis and Design* 47.10 (2011), pp. 1169–1177. ISSN: 0168874X. DOI: 10.1016/j.finel.2011.05.005.

[123] J. C. Heigel, P. Michaleris, and E. W. Reutzel. "Thermo-mechanical model development and validation of directed energy deposition additive manufacturing of Ti-6Al-4V". In: *Additive Manufacturing* 5 (2015), pp. 9–19. ISSN: 22148604. DOI: 10.1016/j.addma.2014.10.003. URL: http://dx.doi.org/10.1016/j.addma.2014.10.003.

[124] Erik R. Denlinger et al. "Effect of inter-layer dwell time on distortion and residual stress in additive manufacturing of titanium and nickel alloys". In: *Journal of Materials Processing Technology* 215 (2015), pp. 123–131. ISSN: 09240136. DOI: 10.1016/j.jmatprotec.2014.07.030. URL: http://dx.doi.org/10.1016/j.jmatprotec.2014.07.030.

[125] David J. Corbin et al. "Impact of Directed Energy Deposition Parameters on Mechanical Distortion of Laser Deposited Ti-6Al-4V". In: *Solid Freeform Fabrication* (2016), pp. 670–679.

[126] Qinglin Han, Yongzhe Li, and Guangjun Zhang. "Online Control of Deposited Geometry of Multi-layer Multi-bead Structure for Wire and Arc Additive Manufacturing". In: *Transactions on Intelligent Welding Manufacturing*. Ed. by Zengxi Pan et al. Vol. I. 2. 2019, pp. 3–24. ISBN: 978-981-10-8739-4. DOI: 10.1007/978-981-10-8740-0. URL: http://link.springer.com/10.1007/978-981-10-8740-0.

[127]   M. L. Griffith et al. "Understanding thermal behavior in the LENS process". In: *Materials and Design* 20.2-3 (1999), pp. 107–113. ISSN: 02641275. DOI: 10.1016/s0261-3069(99)00016-3.

[128]   Kwak Yong-Min and C. Charalabos. "Geometry Regularion of Material Deposition in Near-Net Shape Manufacturing by Thermaly Scanned Welding". In: *Journal of Manufacturing Processes* 4.1 (2002).

[129]   Dongming Hu and Radovan Kovacevic. "Sensing, modeling and control for laser-based additive manufacturing". In: *International Journal of Machine Tools and Manufacture* 43.1 (Jan. 2003), pp. 51–60. ISSN: 08906955. DOI: 10.1016/S0890-6955(02)00163-3.

[130]   Liang Wang, Sergio D. Felicelli, and James E. Craig. "Thermal modeling and experimental validation in the LENSTM process". In: *18th Solid Freeform Fabrication Symposium, SFF 2007* (2007), pp. 100–111.

[131]   Tan Hua et al. "Research on molten pool temperature in the process of laser rapid forming". In: *Journal of Materials Processing Technology* 198.1-3 (2008), pp. 454–462. ISSN: 09240136. DOI: 10.1016/j.jmatprotec.2007.06.090.

[132]   Alexis Medrano et al. "Fibre laser metal deposition with wire: parameters study and temperature monitoring system". In: *XVII International Symposium on Gas Flow, Chemical Lasers, and High-Power Lasers* 7131.April 2009 (2008), p. 713122. ISSN: 0277786X. DOI: 10.1117/12.816831.

[133]   Almir Heralić et al. "Increased stability in laser metal wire deposition through feedback from optical measurements". In: *Optics and Lasers in Engineering* 48.4 (Apr. 2010), pp. 478–485. DOI: 10.1016/J.OPTLASENG.2009.08.012.

[134]   Lie Tang and Robert G. Landers. "Melt pool temperature control for laser metal deposition processes-part I: Online temperature control". In: *Journal of Manufacturing Science and Engineering, Transactions of the ASME* 132.1 (2010), pp. 0110111–0110119. ISSN: 10871357. DOI: 10.1115/1.4000882.

[135]   Almir Heralić. "Monitoring and Control of Robotized Laser Metal-Wire Deposition". PhD thesis. 2012, p. 181. ISBN: 9789173856553.

[136]   P.M. Sequeira Almeida. "PROCESS CONTROL AND DEVELOPMENT IN WIRE AND ARC ADDITIVE MANUFACTURING". PhD thesis. Cranfield University, 2012.

[137]   Jun Xiong and Guangjun Zhang. "Online measurement of bead geometry in GMAW-based additive manufacturing using passive vision". In: *Measurement Science and Technology* 24.11 (2013). ISSN: 13616501. DOI: 10.1088/0957-0233/24/11/115103.

[138]   Jun Xiong et al. "Vision-sensing and bead width control of a single-bead multi-layer part: Material and energy savings in GMAW-based rapid manufacturing". In: *Journal of Cleaner Production* 41 (2013), pp. 82–88. ISSN: 09596526. DOI: 10.1016/j.jclepro.2012.10.009. URL: http://dx.doi.org/10.1016/j.jclepro.2012.10.009.

[139] Jun Xiong and Guangjun Zhang. "Adaptive control of deposited height in GMAW-based layer additive manufacturing". In: *Journal of Materials Processing Technology* 214.4 (2014), pp. 962–968. ISSN: 09240136. DOI: 10.1016/j.jmatprotec.2013.11.014. URL: http://dx.doi.org/10.1016/j.jmatprotec.2013.11.014.

[140] Jun Xiong, Guangjun Zhang, and Weihua Zhang. "Forming appearance analysis in multi-layer single-pass GMAW-based additive manufacturing". In: *The International Journal of Advanced Manufacturing Technology* 80.9-12 (Oct. 2015), pp. 1767–1776. DOI: 10.1007/s00170-015-7112-4.

[141] Jun Xiong, Guangchao Liu, and Yupeng Pi. "Increasing stability in robotic GTA-based additive manufacturing through optical measurement and feedback control". In: *Robotics and Computer-Integrated Manufacturing* 59.May 2018 (2019), pp. 385–393. ISSN: 07365845. DOI: 10.1016/j.rcim.2019.05.012. URL: https://doi.org/10.1016/j.rcim.2019.05.012.

[142] Sreekar Karnati et al. "Vision-based Process Monitoring for Laser Metal Deposition Processes". In: *Proceedings Solid Freeform Fabrication symposium* (2013).

[143] Jun Xiong et al. "Modeling of bead section profile and overlapping beads with experimental validation for robotic GMAW-based rapid manufacturing". In: *Robotics and Computer-Integrated Manufacturing* 29.2 (2013), pp. 417–423. ISSN: 07365845. DOI: 10.1016/j.rcim.2012.09.011.

[144] Jun Xiong et al. "Bead geometry prediction for robotic GMAW-based rapid manufacturing through a neural network and a second-order regression analysis". In: *Journal of Intelligent Manufacturing* 25.1 (Feb. 2014), pp. 157–163. DOI: 10.1007/s10845-012-0682-1.

[145] Shyam Barua et al. "Vision-based defect detection in laser metal deposition process". In: *Rapid Prototyping Journal* 20.1 (2014), pp. 77–86. ISSN: 13552546. DOI: 10.1108/RPJ-04-2012-0036.

[146] A. R. Nassar, T. J. Spurgeon, and E. W. Reutzel. "Sensing defects during directed-energy additive manufacturing of metal parts using optical emissions spectroscopy". In: *Applied Research Laboratory at the Pennsylvania State University* (2014), pp. 278–287.

[147] Donghong Ding et al. "A multi-bead overlapping model for robotic wire and arc additive manufacturing (WAAM)". In: *Robotics and Computer-Integrated Manufacturing* 31 (2015), pp. 101–110. ISSN: 07365845. DOI: 10.1016/j.rcim.2014.08.008. URL: http://dx.doi.org/10.1016/j.rcim.2014.08.008.

[148] Abdalla R. Nassar et al. "Intra-layer closed-loop control of build plan during directed energy additive manufacturing of Ti-6Al-4V". In: *Additive Manufacturing* 6 (2015), pp. 39–52. ISSN: 22148604. DOI: 10.1016/j.addma.2015.03.005.

[149] Dennis A. Kriczky et al. "3D spatial reconstruction of thermal characteristics in directed energy deposition through optical thermal imaging". In: *Journal of Materials Processing Technology* 221 (2015), pp. 172–186. ISSN: 09240136. DOI: 10.1016/j.jmatprotec.2015.02.021.

[150] Chen Shen et al. "Fabrication of iron-rich Fe-Al intermetallics using the wire-arc additive manufacturing process". In: *Additive Manufacturing* 7 (2015), pp. 20–26. ISSN: 22148604. DOI: 10.1016/j.addma.2015.06.001. URL: http://dx.doi.org/10.1016/j.addma.2015.06.001.

[151] A. R. Nassar, Brandon Starr, and E. W. Reutzel. "Process monitoring of directed-energy deposition of Inconel-718 via plume imaging". In: *Applied Research Laboratory at the Pennsylvania State University* (2015), pp. 284–294.

[152] Christopher B. Stutzman, Abdalla R. Nassar, and Edward W. Reutzel. "Multi-sensor investigations of optical emissions and their relations to directed energy deposition processes and quality". In: *Additive Manufacturing* 21.March (2018), pp. 333–339. ISSN: 22148604. DOI: 10.1016/j.addma.2018.03.017. URL: https://doi.org/10.1016/j.addma.2018.03.017.

[153] Jarred C. Heigel, Pan Michaleris, and Todd A. Palmer. "Measurement of forced surface convection in directed energy deposition additive manufacturing". In: *Proceedings of the Institution of Mechanical Engineers, Part B: Journal of Engineering Manufacture* 230.7 (2016), pp. 1295–1308. ISSN: 20412975. DOI: 10.1177/0954405415599928.

[154] Qian Wang et al. "Physics-Based Multivariable Modeling and Feedback Linearization Control of Melt-Pool Geometry and Temperature in Directed Energy Deposition". In: *Journal of Manufacturing Science and Engineering, Transactions of the ASME* 139.2 (2017), pp. 1–12. ISSN: 15288935. DOI: 10.1115/1.4034304.

[155] Bintao Wu et al. "Effects of heat accumulation on the arc characteristics and metal transfer behavior in Wire Arc Additive Manufacturing of Ti6Al4V". In: *Journal of Materials Processing Technology* 250.December 2016 (Dec. 2017), pp. 304–312. ISSN: 09240136. DOI: 10.1016/j.jmatprotec.2017.07.037. URL: http://dx.doi.org/10.1016/j.jmatprotec.2017.07.037%20https://linkinghub.elsevier.com/retrieve/pii/S0924013617303370.

[156] A. I. Adediran. "Automatic Error Detection and Correction in Laser Metal Wire Deposition - an Additive". PhD thesis. The University of Tennessee, 2018.

[157] Justin Whiting, Adam Springer, and Federico Sciammarella. "Real-time acoustic emission monitoring of powder mass flow rate for directed energy deposition". In: *Additive Manufacturing* 23.May (2018), pp. 312–318. ISSN: 22148604. DOI: 10.1016/j.addma.2018.08.015. URL: https://doi.org/10.1016/j.addma.2018.08.015.

[158] Fangda Xu et al. "Realisation of a multi-sensor framework for process monitoring of the wire arc additive manufacturing in producing Ti-6Al-4V parts". In: *International Journal of Computer Integrated Manufacturing* 31.8 (2018), pp. 785–798. ISSN: 13623052. DOI: 10.1080/0951192X.2018.1466395.

[159] Zeqi Hu et al. "Multi-bead overlapping model with varying cross-section profile for robotic GMAW-based additive manufacturing". In: *Journal of Intelligent Manufacturing* 3.2018 (2019). ISSN: 15728145. DOI: 10.1007/s10845-019-01501-z. URL: https://doi.org/10.1007/s10845-019-01501-z.

[160] A. Chabot et al. "Towards defect monitoring for metallic additive manufacturing components using phased array ultrasonic testing". In: *Journal of Intelligent Manufacturing* (2019). ISSN: 15728145. DOI: 10.1007/s10845-019-01505-9. URL: https://doi.org/10.1007/s10845-019-01505-9.

[161] Xiaolong Wang, Aimin Wang, and Yuebo Li. "An online surface height measurement method for GTAW-based additive manufacturing". In: *Welding in the World* 64.1 (2020), pp. 11–20. ISSN: 18786669. DOI: 10.1007/s40194-019-00813-1.

[162] Tom DeMarco. *Controlling software projects: management, measurement & estimation*. Yourdon Press computing series, 1999.

[163] ASTM International. *Standard Guide for Reporting Uncertainty of Test Results and Use of the Term Measurement Uncertainty in ASTM Test Methods*. Tech. rep. E2655. West Conshohocken, PA: ASTM, 2020. DOI: 10.1520/E2655-14R20.

[164] Ohm G.S. *Understanding Additive Manufacturing*. Berlin, Germany: T.H. Riemann, 1827.

[165] Baltej Singh Rupal, Rafiq Ahmad, and Ahmed Jawad Qureshi. "Feature-Based Methodology for Design of Geometric Benchmark Test Artifacts for Additive Manufacturing Processes". In: *Procedia CIRP* 70.May (2018), pp. 84–89. ISSN: 22128271. DOI: 10.1016/j.procir.2018.02.012. URL: https://doi.org/10.1016/j.procir.2018.02.012.

[166] J.C. Metcalfe and M.B.C. Quigley. "Heat Transfer in Plasma-Arc Welding". In: *Welding Research Abroad* (1975), pp. 99–104.

[167] Friedrich B. Prinz, Joseph J. Beaman, and et al. *Rapid Prototyping in Europe and Japan Volumne I. Analytical Chapters*. Tech. rep. Japanese Technology Evaluation Center and World Technology Evaluation Center, 1997.

[168] J.E. Blather. *Manufacture of contour relief-maps*. Patent US473901A. May 1892.

[169] B.V. Perera. *Process of making relief maps*. Patent US2189592A. Feb. 1940.

[170] E.E. Zang. *Vitavue relief model technique*. Patent US3137080A. June 1964.

[171] K. Matsubara. *Molding Method of Casting using Photocurable Substance*. Japanese Kokai Patent Application, Sho 51 [1976] 10813. 1976.

[172] P.L. DiMatteo. *Method of generating and constructing three-dimensional bodies*. Patent US3932923A. 1976.

[173] T. Nakagawa. "Blanking Tool by Stacked Bainite Steel Plates". In: (1974), pp. 93–101.

[174] Masanori Kunieda and Takeo Nakagawa. "DEVELOPMENT OF LAMINATED DRAWING DIES BY LASER CUTTING." In: 18 (Dec. 1984), pp. 353–354.

[175] Masanori Nakagawa Takeo and Kunieda and Sheng-Dong Liu. "Laser Cut Sheet Laminated Forming Dies by Diffusion Bonding". In: *Proceedings of the Twenty-Fifth International Machine Tool Design and Research Conference*. Ed. by S. A. Tobias. London: Macmillan Education UK, 1985, pp. 505–510. ISBN: 978-1-349-07529-4. DOI: 10.1007/978-1-349-07529-4_60. URL: https://doi.org/10.1007/978-1-349-07529-4_60.

[176] Robert A. Sobieszek. "Sculpture as the Sum of Its Profiles: François Willème and Photosculpture in France, 1859–1868". In: *The Art Bulletin* 62.4 (1980), pp. 617–630. ISSN: 15596478. DOI: 10.1080/00043079.1980.10787818.

[177] F. Willème. *Photographing Sculpture*. Patent US43822A. 1864.

[178] C. Baese. *Photographic process for the reproduction of plastic objects*. Patent US774549A. 1904.

[179] I. Morioka. *Process for manufacturing a relief by the aid of photography*. Patent US2015457A. 1935.

[180] O.J. Munz. *Photo-glyph recording*. Patent US2775758A. 1956.

[181] M.K. Niaki and F. Nonino. *The Management of Additive Manufacturing*. Springer Series in Advanced Manufacturing. Cham, Switzerland: Springer International Publishing, 2018, pp. 1–250. ISBN: 978-3-319-56308-4. DOI: 10.1007/978-3-319-56309-1. URL: http://link.springer.com/10.1007/978-3-319-56309-1.

[182] W.K. Swainson. *Method of producing a three-dimensional figure by holography*. Patent GB1243044A. 1971.

[183] W.K. Swainson. *Method, medium and apparatus for producing three-dimensional figure product*. Patent US4041476A. 1977.

[184] Hideo Kodama. "Automatic method for fabricating a three-dimensional plastic model with photo-hardening polymer". In: *Review of Scientific Instruments* 52.11 (1981), pp. 1770–1773. ISSN: 00346748. DOI: 10.1063/1.1136492.

[185] Capucine Lonjon. "The history of 3D printer: from rapid prototyping to additive fabrication". In: *Sculpteo, Innovation and Business strategy* (Mar. 2017). URL: https://www.sculpteo.com/blog/2017/03/01/whos-behind-the-three-main-3d-printing-technologies.

[186] A.J. Herbert. "Solid Object Generation". In: *Journal of Applied Photographic Engineering* 8.4 (1982), pp. 185–188.

[187] J.C. Andre et al. *Process and device for producing a model of an industrial component*. FR2583334A1. 1985.

[188]   Charles W. Hull. *Apparatus for production of three-dimensional objects by stereolithography*. Patent US4575330A. Mar. 1986.

[189]   International Organization for Standardization. *Additive manufacturing - General principles- Part 2: Overview of process categories and feedstock*. Tech. rep. ISO17296-2. Geneva, Switzerland: ISO, 2015.

[190]   International Organization for Standardization. *Additive Manufacturing-General Principles-Part 1: Terminology*. Tech. rep. ISO17296-1. Geneva, Switzerland: ISO, 2015.

Appendix A: Prehistory of AM Appendix

Additive manufacturing was previously labelled as rapid prototyping (RP). Early roots of it can be traced to at least two areas: topology and photosculpture [167]. In 1890, Blanther suggested a mould for topographical relief maps done by layers [Fig. A.1]. Series of wax plates were stacked and smoothed based on impressing topographical contour lines to produce three-dimensional surfaces corresponding to the terrain [168].
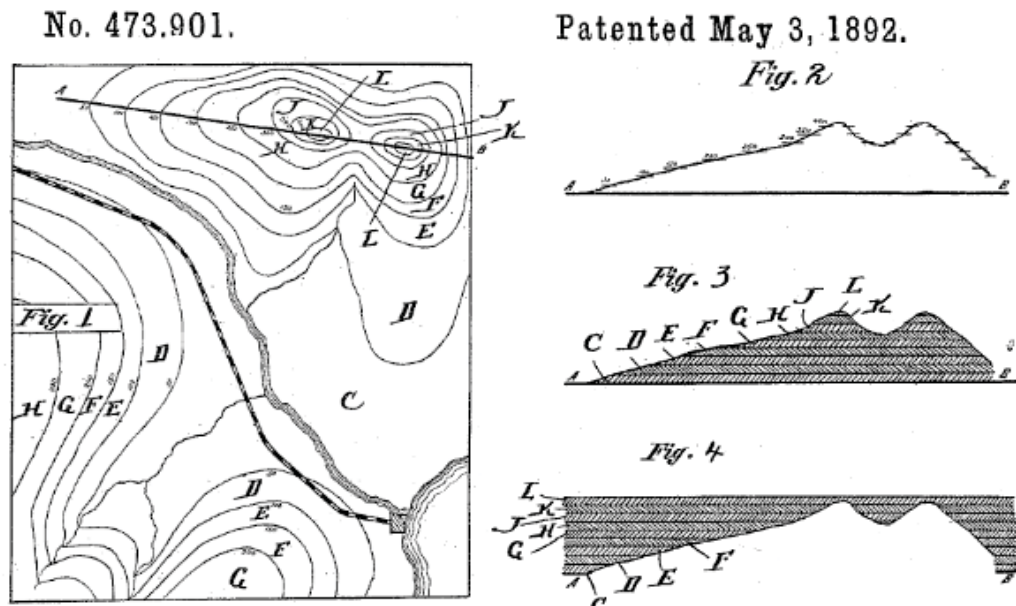
Figure A.1: Manufacture of contour relief maps patented by J.E. Blanther [168].

Different materials such as cardboard and transparent plates were used to produce similar results [169, 170] until 1972 when Matsubara of Mitsubishi Motors proposed using photo-hardening materials. The process consisted of a photopolymer resin coated onto refractory particles, which are then spread into a layer and heated to create a coherent sheet. Then a light source is selectively projected on the sheet to harden the material. Remaining unhardened material was dissolved away with a solvent. In the end, all the layers created with this process are stacked to form a casting mould [171]. The technique could be used to produce surfaces that are difficult to fabricate by standard machining operations [172]. In 1979, Professor Nakagawa of Tokyo University used the lamination technique to create blanking [173],

185

forming [174], and injection moulding tools. Nakagawa mentions the possibility of building complex cooling channels for injection moulds [175].

On the other hand, in 1859, François Willème created a method called mechanical sculpture to conceive exact three-dimensional replicas of objects and human forms. The process was simply an outgrowth of the idea that the sum of the profiles equals the whole volumetric figure. His idea developed into the first photosculpture patent in 1860 in France, and in 1864 in the United States [Fig. A.2] [176, 177].
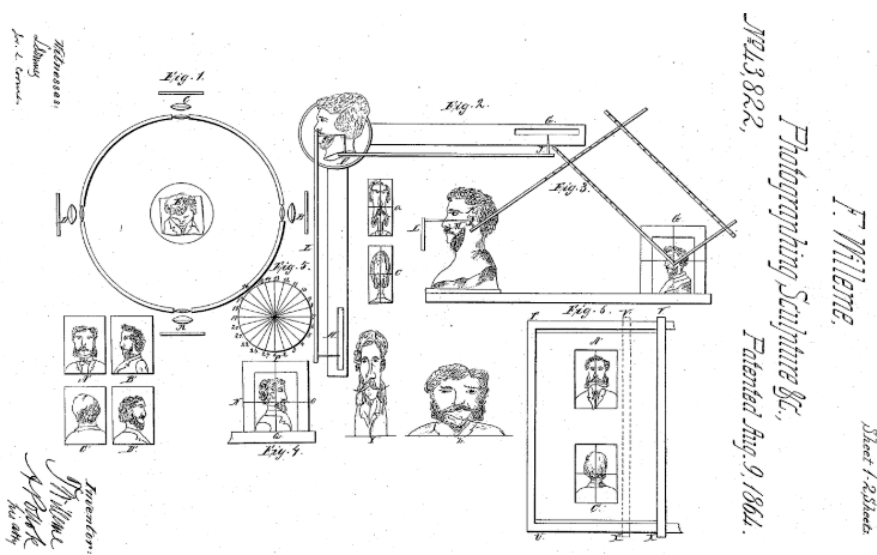
Figure A.2: Photographing Sculpture patented by F. Willème [177].

An improvement of the method developed by Willème was achieved by Carlo Baese in 1904, where a superposition of photographic plates was exposed to light and expanded to create an exact imitation in relief of the object photographed [178]. Figure A.3 shows the perspective view of the position of the illuminating lamps when shooting an object to be reproduced in profile relief.

By 1935, photosculpture and topology started to merge, as shown by the patent of Morioka. His invention describes the manufacturing process of a land relief aided by photography. Strip lines of the pictures are assembled and bound together to create a replica of the object [179]. Munz created the first photo-recorder in 1956. He disclosed an apparatus called the Photo-glyph recording in which three-dimensional objects were represented in a recording space, defined by a container and filled with a photosensitive medium. The target was photographed section by section while the photo-emulsion solidifies. The piston containing the replica is drawn away by a rack controlled with a motor [Fig. A.4]. The part is then manually carved of photochemically etched to create the final object [180].
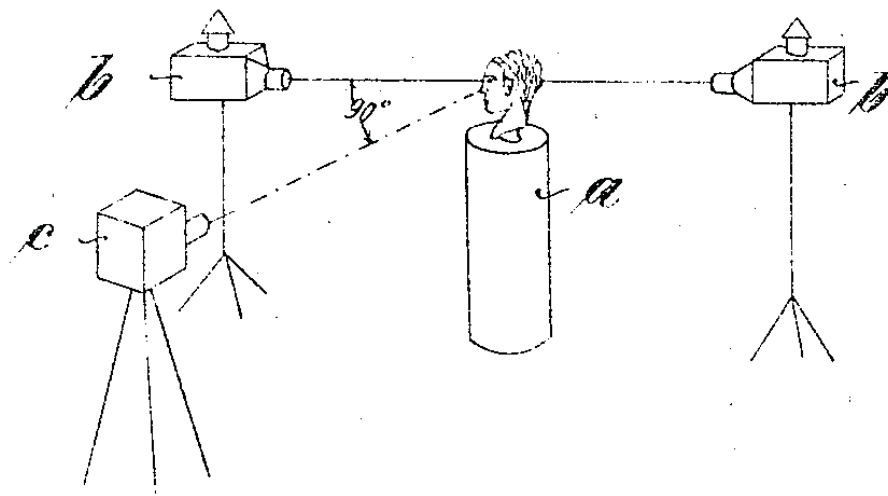
Figure A.3: Photographic process for the reproduction of plastic objects patented by C.Baese [178].
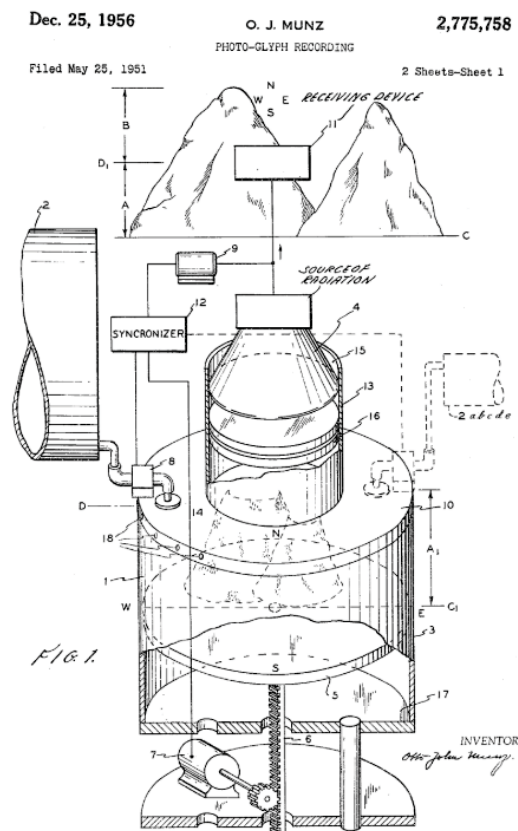
Figure A.4: Photo-Glyph Recording patented by O.J. Munz [180].

Appendix B: Stereolithography: The first AM technology Appendix

The first attempt to create a solid object with photo-polymers occurred in the 1960s at Battelle Memorial Institute. This technology used two intersecting laser beams of different wavelengths to solidify resin inside a vat. The material used in the process was a photo-polymer invented by DuPont in 1950 [181]. In 1967, Swainson applied a similar dual laser beam to produce a 3D figure by holography [182], and then launched the company Formigraphic Engine Company. In early 1970, the company commercialized its first laser-prototype project using a process called photochemical machining. By 1977, Swainson filed another patent in which the generation of a 3D object was shown [Fig. B.1]. Although this system seemed like a rudimentary process, it is the first traceable patent for a stereolithography 3D printer [183].

Swainson and the Battelle Memorial Institute employed infrared (IR) and ultraviolet (UV) laser beams intersecting to solidify polymers. Still, it was not until 1981 that H. Kodama presented an automatic method for fabricating a three-dimensional model with photo-hardening polymer using a single beam UV laser [184]. In his approach, a model is built by stacking the cross-sectional solidified layers. Three apparatus were constructed, one with UV exposure from the top, another from the bottom, and one with a scanning fibre transmitter mounted on a commercial XY plotter [Fig. B.2]. These experiments were the first evidence of working AM techniques. Unfortunately, due to funding issues, the full patent specification was not filed before the application deadline [185].

After Kodama, parallel independent efforts using photopolymers were undertaken by Alan Herbert in the U.S and Jean-Claude Andre, Michael Bouchy, Miguel Cabrera, Alain Le Mehaute and Oliver de Witte in France [186, 187]. Neither of these works could result in a patent due to a lack of interest from their respective companies. Finally, in 1986, C. Hull filed the patent for apparatus for production of three-dimensional objects by Stereolithography [188].
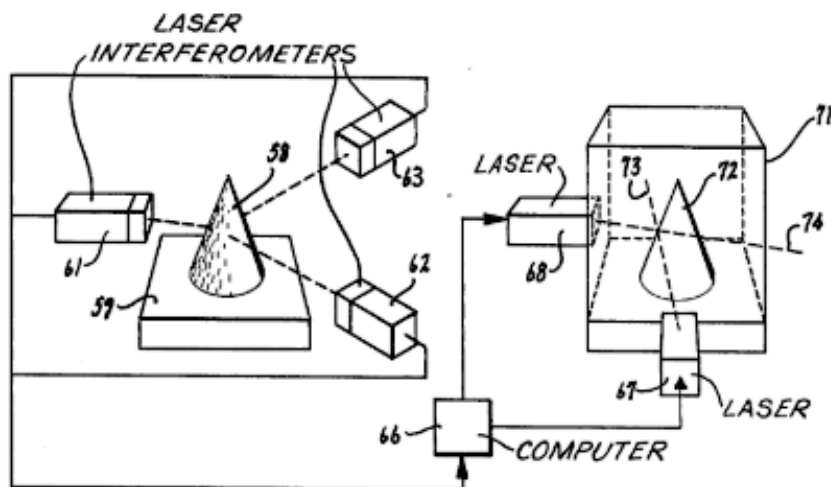
Figure B.1: Method, medium and apparatus for producing three-dimensional figure product patented by W.K. Swainson [183].
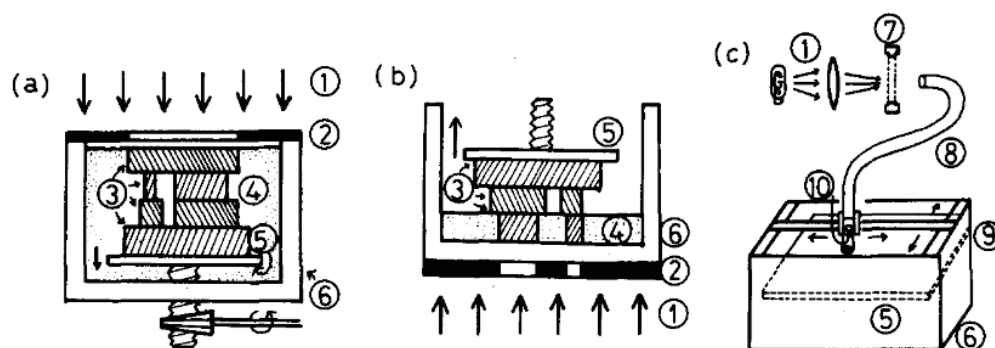
Figure B.2: Three type of systems: UV light from a)top, b)bottom, and c)fiber transmitter by H. Kodama [184].

189

Appendix C: Additive Manufacturing Technology Appendix

Figure C.1 shows the AM technology classification according to the International Standard ISO 17296: Vat photopolymerization, material extrusion, material jetting, binder jetting, direct energy deposition, powder bed fusion, and sheet lamination [189].
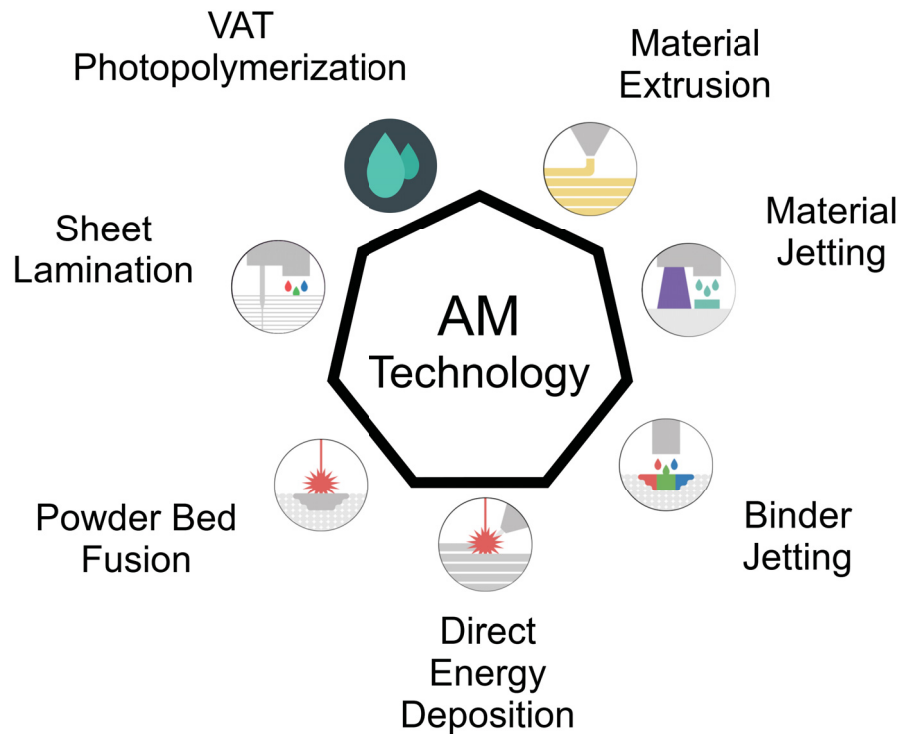
Figure C.1: Additive Manufacturing Technologies.

According to the Standard ISO17296 terminology [190], AM is defined as the process of joining materials to make parts or objects from 3D model data, usually layer upon layer, as opposed to subtractive manufacturing and formative manufacturing methodologies. Table D.1 summarized the differences between different technologies.

Vat photopolymerization: Liquid photopolymer in a vat is selectively cured by light-activated polymerization. Some examples are Stereolithography (SLA), Digital Light Processing (DLP) and Continuous Digital Light Processing (CDLP).

Material Extrusion: Process in which material is selectively dispensed through a nozzle or orifice. Composite and plastic Fused Deposition Modeling (FDM) are examples of this technology.

Material Jetting: Process in which droplets of build material are selectively deposited. For plastics, Material Jetting (MJ) term is adopted. NanoParticle Jetting (NPJ) refers to metals, and Drop on Demand (DOD) is used for wax.

Binder Jetting: Powder materials are selectively deposited using a liquid bonding agent. Binder Jetting (BJ) can be used to create gypsum, sand or metal parts.

Direct Energy Deposition: Process in which focused thermal energy is used to fuse materials while being deposited. Laser Engineering Net Shape (LENS), Electron Beam Additive Manufacturing (EBAM), and Plasma Transferred Arc Additive Manufacturing (PTA-AM) are examples of this type of technology.

Powder Bed Fusion: Thermal energy selectively fuses regions of a powder bed. For plastics, Multi Jet Fusion (MJF) and Selective Laser Sintering (SLS) are adopted terms. For metals, Direct Metal Laser Sintering (DMLS)/Selective Laser Melting (SLM) and Electron Beam Melting (EBM) are standardized terminologies.

Sheet Lamination: In this process, sheets of material are bonded to form an object. Laminated Object Manufacturing (LOM) involves building composite or paper-made parts.

Table D.1: Summary of Additive Manufacturing Technologies.

Technology	Source of activation	Binding mechanism	Feedstock
Vat Photopolymerization	UV radiation	Chemical reaction	liquid or paste photoreactive resin
Material Extrusion	Heat, ultrasound or chemical reaction	Thermal or chemical reaction	Filament or paste
Material Jetting	Radiation light	Chemical reaction or adhesion by solidification	Liquid photopolymer or melted wax
Binder Jetting	Chemical reaction	Thermal or chemical reaction	Powders and liquid adhesive/bonding agent
Direct Energy Deposition	Laser, electron beam or plasma arc	Thermal reaction	Metal powder or wire
Powder Bed Fusion	Laser, electron beam or infrared lamps	Thermal reaction	Thermoplastic, metals or ceramic powders
Sheet Lamination	Localized or large scale heating, chemical reaction and ultrasound	Thermal, chemical or ultrasonic reaction	Sheet material: paper, metal or polymers

Appendix D: Code Appendix

D.1 Linear interpolation of data

Listing D.1: Visual Basic Code for linear interpolation of data.

```
Attribute VB_Name = "Module1"
Sub Xs()
Attribute Xs.VB_ProcData.VB_Invoke_Func = "j\n14"
' Spatial transformation
'
Dim Pts As Long

Dim R1 As Range
Dim R2 As Range

Dim E_end As String
Dim F_end As String

Set R1 = Range(Range("E2"), Range("E2").End(xlDown))
Set R2 = Range(Range("F2"), Range("F2").End(xlDown))
F_end = Range("F2").End(xlDown).Address()
E_end = Range("E2").End(xlDown).Address()
Range("B3").Formula = "=ROUND(" & F_end & ",3)-ROUND($F$2,3)"
Range("B4").Formula = "=$B$3/$B$2"
Pts = Range("B4").Value
Range("B5").Formula = "=ROUND(" & E_end & ",3)-ROUND($E$2,3)"
Range("B6").Formula = "=$B$5/$B$4"
Range("H2").Formula = "=$E$2"
Range("H3").FormulaR1C1 = "=R[-1]C+R6C2"
Range("H4").FormulaR1C1 = "=R[-1]C+R6C2"
Range("H5").FormulaR1C1 = "=R[-1]C+R6C2"
Range("H3:H5").Select
Selection.AutoFill Destination:=Range("H3:H" & CStr(Pts + 2) & ""), _
Type:=xlFillDefault
Range("I2").Formula = "=ROUND($F$2,3)"
Range("I3").Formula = _
"=FORECAST.LINEAR(H3,OFFSET($F$2:" & F_end & ",MATCH(H3,$E$2:" & E_end & ",1)" & _
"-1,0,2),OFFSET($E$2:" & E_end & ",MATCH(H3,$E$2:" & E_end & ",1)-1,0,2))"
Range("I3").Select
Selection.AutoFill Destination:=Range("I3:I" & CStr(Pts + 1) & "")
Range("I" & CStr(Pts + 2) & "").Formula = "=ROUND(" & F_end & ",3)"
ActiveSheet.Shapes.AddChart2(240, xlXYScatter).Select
ActiveChart.SeriesCollection.NewSeries
ActiveChart.FullSeriesCollection(1).Name = "=""Original"""
ActiveChart.FullSeriesCollection(1).XValues = "=Scale!$E$2:" & E_end & ""
ActiveChart.FullSeriesCollection(1).Values = "=Scale!$F$2:" & F_end & ""
ActiveChart.SeriesCollection.NewSeries
ActiveChart.FullSeriesCollection(2).Name = "=""Interpolated"""
ActiveChart.FullSeriesCollection(2).XValues = "=Scale!$H$2:$H$" & CStr(Pts + 2) & ""
ActiveChart.FullSeriesCollection(2).Values = "=Scale!$I$2:$I$" & CStr(Pts + 2) & ""
ActiveChart.SetElement (msoElementPrimaryValueGridLinesNone)
ActiveChart.SetElement (msoElementPrimaryCategoryGridLinesNone)
ActiveChart.SetElement (msoElementPrimaryCategoryAxisTitleAdjacentToAxis)
```

```vba
ActiveChart.SetElement (307)
ActiveChart.Axes(xlCategory, xlPrimary).AxisTitle.Text = "Time [sec]"
ActiveChart.Axes(xlCategory).AxisTitle.Select
With Selection.Format.TextFrame2.TextRange.Font
.NameComplexScript = "Times New Roman"
.NameFarEast = "Times New Roman"
.Name = "Times New Roman"
End With
ActiveChart.Axes(xlValue, xlPrimary).AxisTitle.Text = "Axis position [mm]"
ActiveChart.Axes(xlValue).AxisTitle.Select
With Selection.Format.TextFrame2.TextRange.Font
.NameComplexScript = "Times New Roman"
.NameFarEast = "Times New Roman"
.Name = "Times New Roman"
End With
End Sub
```

Appendix E: Table Appendix

Table E.1: Single-track single-layer bead data.

	Center gas [SLPM]	Powder gas [SLPM]	Shielding gas [SLPM]	SOD [mm]	Travel speed [mm/min]	Powder flow [GPM]	Voltage			Laser				Prediction				MSE [mm^2]	RMSD [mm]
							Mean [V]	Range [V]	SD [V]	Mean [mm]	Range [mm]	SD [mm]	Uncertainty [mm]	Mean [mm]	Range [mm]	SD [mm]	Uncertainty [mm]		
V1 Aut.	1.2	1.2	11	5	500	0	24.44	4.03	0.88	4.79	0.89	0.27	34.79	4.82	0.62	0.13	17.90	0.043	206
V1 Dep.	1.2	1.2	11	5	500	20	20.63	1.88	0.30	3.45	2.37	0.63	88.20	3.45	1.57	0.25	35.09	0.327	572
V2 Aut.	2	4	15	11	500	0	36.10	2.43	0.66	11.4	3.50	0.86	113.6	11.4	0.31	0.08	11.15	0.716	846
V2 Dep.	2	4	15	11	500	70	38.21	2.18	0.62	9.35	1.39	0.22	31.22	9.35	0.33	0.09	13.39	0.040	199
V3 Aut.	1.6	3.2	13	9	500	0	27.43	1.12	0.36	8.96	0.37	0.10	12.88	8.96	0.12	0.04	5.40	0.008	87
V3 Dep.	1.6	3.2	13	9	500	27	27.25	0.34	0.09	7.63	2.06	0.48	67.62	7.63	0.09	0.02	3.60	0.228	477
V4 Aut.	1.3	1.6	12	10	500	0	29.41	3.26	1.13	9.95	0.37	0.09	12.57	9.95	0.04	0.01	1.84	0.009	93
V4 Dep.	1.3	1.6	12	10	500	49	29.77	1.02	0.29	7.59	1.00	0.18	25.13	7.59	0.41	0.12	16.27	0.018	135
V5 Aut.	1.4	2.8	14	11	500	0	28.77	0.99	0.27	11.0	0.21	0.06	8.28	11.0	0.04	0.01	1.37	0.003	61
V5 Dep.	1.4	2.8	14	11	500	63	29.14	3.16	0.86	9.97	3.41	1.04	146.2	9.97	3.29	0.89	125.1	0.285	534

Table E.2: Single-track single-layer bead data continuation.

	Center gas [SLPM]	Powder gas [SLPM]	Shielding gas [SLPM]	SOD [mm]	Travel speed [mm/min]	Powder flow [GPM]	Voltage			Laser				Prediction				MSE [mm^2]	RMSD [mm]
							Mean [V]	Range [V]	SD [V]	Mean [mm]	Range [mm]	SD [mm]	Uncertainty [mm]	Mean [mm]	Range [mm]	SD [mm]	Uncertainty [mm]		
V6 Aut.	1.8	2	13	8	500	0	29.60	0.66	0.16	8.01	1.26	0.25	33.37	8.01	0.18	0.05	6.15	0.060	245
V6 Dep.	1.8	2	13	8	500	56	30.58	1.08	0.26	5.64	0.41	0.10	14.83	5.64	0.34	0.08	11.53	0.004	66
V7 Aut.	1.8	2.4	12	7	500	0	32.43	0.68	0.16	6.99	4.75	0.79	98.31	7.01	1.10	0.26	34.24	0.603	776
V7 Dep.	1.8	2.4	12	7	500	42	33.06	0.74	0.25	5.37	0.97	0.16	22.52	5.37	0.10	0.03	4.84	0.024	155
V8 Aut.	1.5	1	15	5	600	0	23.83	0.33	0.09	4.88	1.40	0.43	56.87	4.88	1.26	0.36	48.13	0.051	226
V8 Dep.	1.5	1	15	5	600	40	20.12	0.49	0.09	4.82	0.68	0.18	21.18	4.82	0.24	0.04	5.20	0.029	170
V9 Aut.	1.5	1	15	5	600	0	23.69	0.57	0.14	5.09	1.21	0.37	49.29	5.09	1.27	0.32	42.64	0.034	185
V9 Dep.	1.5	1	15	5	600	60	20.18	0.42	0.08	4.95	0.75	0.15	18.36	4.95	0.02	0.01	0.43	0.022	150
V10 Aut.	1.5	1	15	5	600	0	24.34	0.74	0.21	5.05	1.18	0.36	47.98	5.05	1.21	0.35	46.55	0.007	87
V10 Dep.	1.5	1	15	5	600	50	20.38	0.50	0.12	4.98	0.37	0.08	9.66	4.98	0.09	0.02	2.82	0.005	77

Table E.3: Single-track single-layer bead data continuation.

| | Center gas [SLPM] | Powder gas [SLPM] | Shielding gas [SLPM] | SOD [mm] | Travel speed [mm/min] | Powder flow [GPM] | Voltage | | | Laser | | | | Prediction | | | | MSE [mm^2] | RMSD [mm] |
							Mean [V]	Range [V]	SD [V]	Mean [mm]	Range [mm]	SD [mm]	Uncertainty [mm]	Mean [mm]	Range [mm]	SD [mm]	Uncertainty [mm]		
V11 Aut.	1	1	15	5	2300	0	23.51	0.94	0.27	5.04	1.15	0.35	46.49	5.04	1.19	0.32	43.1	0.017	131
V11 Dep.	1	1	15	5	2300	30	22.70	0.57	0.12	4.93	0.58	0.10	14.48	4.93	0.21	0.05	6.96	0.007	84
V12 Aut.	1	1	15	13	1450	0	28.01	2.12	0.30	12.7	1.07	0.33	43.75	12.7	1.31	0.19	25.2	0.072	267
V12 Dep.	1	1	15	13	1450	30	29.60	0.97	0.20	11.5	2.22	0.44	65.06	11.5	0.06	0.01	1.74	0.186	431
V13 Aut.	1	1	15	10	600	0	27.58	0.72	0.21	10.1	0.96	0.30	39.64	10.1	0.94	0.28	36.6	0.013	113
V13 Dep.	1	1	15	10	600	30	28.54	1.66	0.38	8.41	1.87	0.32	47.16	8.42	0.81	0.18	27.5	0.064	254
R. Aut.	1.5	1.5	10	7	500	0	27.19	0.65	0.14	5.96	0.50	0.14	16.75	5.96	0.51	0.11	13.4	0.007	83
R. Dep.	1.5	1.5	10	7	500	40	28.40	1.40	0.35	4.19	0.72	0.16	18.96	4.19	0.30	0.07	9.12	0.018	136